Hippocampal network patterns in K_v7/M-current deficient mice (*Mus musculus, Linnaeus 1758*)

Dissertation

Zur Erlangung des akademischen Grades

des Doktors der Naturwissenschaften

des Fachbereichs Biologie,

der Fakultät für Mathematik, Informatik und Naturwissenschaften,

der Universität Hamburg

Vorgelegt von

Jasper Grendel

aus Warnsveld (Niederlande)

Hamburg, 2017

Tag der Disputation: 16.06.2017

Prüfungskommissionsvorsitzende: Prof. Esther Diekhof

Folgende Gutachter empfehlen die Annahme der Dissertation:

Erstgutachter:	Prof. Dr. Dirk Isbrandt
	Deutsches Zentrum für neurodegenerative Erkrankungen (DZNE)– Köln/Bonn
Zweitgutachter:	Prof. Dr. Christian Lohr
	Universität Hamburg

EIDESTATTLICHE VERSICHERUNG

Hiermit erkläre ich an Eides statt, dass ich die vorliegende Dissertationsschrift selbst verfasst und keine anderen als die angegebenen Quellen und Hilfsmittel benutzt habe.

Hamburg, den ……..

_____

Jasper Grendel

Acknowledgement

I would like to thank Prof. Dirk Isbrandt for reaching out to me and offering me the chance to work in his lab, despite the fact that I had limited working knowledge of neurophysiology and computer programming at the time. The highly interesting neuroscienctific project he allowed me to work in was perfectly suited for my interests. I thank him for his advice and support and for helping me to develop analytical, technical and didactical skills which will serve me well in the future.

Furthermore, I would like to thank Prof. Christian Lohr for agreeing to be one of the reviewers of this thesis.

For his expert advice I thank Dr. Fabio Morrelini, from whom I have learned a lot on statistics and mouse behavior and with whose guidance I was able to set up the behavioral tests applied during this thesis.

When it comes to programming skills, Dr. Stephan Marguet is surely my superior and I thank him for helping me solve some of the programming issues I have faced.

For his advice on my thesis I want to thank Dr. Malte Stockebrand for his valuable input.

Since I am a non-native english speaker, I want to thank Dr. Katherine Miller for spelling and grammar corrections.

I also want to thank all the (former) members from the lab of Experimental Neuropediatrics. The atmosphere in the lab was always highly positive and friendly, music was (almost) always playing, interaction was always friendly. My time in this lab could not have been as pleasant if it wasn't for these people.

Lastly, I want to thank my family: Johanne and David, for reminding me how cool it is to be a scientist who finds out new things about the world, and Anna, for keeping me grounded and making me a better person.

Abstract

ENGLISH
Mutations that lead to altered K_v7/M-currents result in an epileptic phenotype in human patients. Investigation of the effect of K_v7/M-currents on neuronal and network function in adult animals is limited to short-term pharmacological *in-vitro* or *in-vivo* manipulation and electrocorticogram (ECoG) recordings from genetic mouse models. This thesis investigates the effect of chronic M-current deficiency on intracranially recorded local field potentials (LFPs) from the hippocampus in adult mice, in the absence of confounding gross morphological abnormalities. Through the transgenic expression of a dominant-negative $K_v7.2$ subunit via a Tet-Off system, M-current-deficient mice are compared to control mice with respect to their hippocampal CA1 electrophysiological parameters during several behavioral states. Theta (4-12 Hz) and gamma (30-100 Hz) oscillations during paradoxical/rapid eye movement (REM)-like sleep and sharp wave-ripple (SW-R) complexes during slow wave sleep (SWS) were analyzed off-line from recordings made both prior to and after performing behavioral tasks. Unit spiking was analyzed from pre-task sleep. The selected behavioral paradigms included open field, spatial novelty, a single trial spatial memory (STSM) task, and Y-maze. Theta and gamma oscillations were also analyzed during running. K_v7/M-current deficient mice showed significant changes in their LFP, ranging from theta and gamma power reductions to smaller sharp waves and ripples. No change was seen in basic properties for unit spiking. Speed modulation of theta and gamma power and pre- to post-task sleep changes in LFPs were similar between controls and mutants. Behavioral testing showed reduced performance for the Y-maze, with a tendency toward reduced performance during the 24h-STSM recall. The electrophysiological changes presented here and the hyperexcitability previously shown *in-vitro* together suggest a homeostatic compensatory mechanism, which may also include changes at the synaptic level. The results reported in this thesis contribute to the overall understanding of the effect of chronic K_v7/M-current deficiency on the mammalian brain and provide suggestions for further experiments.

DEUTSCH
Mutationen in Genen, die zu veränderter K_v7/M-Kanalaktivität führen, sind mit Neugeborenenepilepsiesyndromen beim Menschen assoziiert. Untersuchungen über elektrophysiologische Effekte eines normalen oder veränderten K_v7/M-Stroms in adulten Tieren beschränken sich bisher auf akute pharmakologische Manipulationen *in-vitro* und *in-vivo*, oder Elektrokortikogrammaufnahmen (ECoG) genetischer Mausmodelle. Hier wird der Effekt einer chronischen M-Stromdefizienz auf intrakranial aufgenommene lokale Feldpotenziale (LFP) im Hippocampus adulter Mäuse, die dabei keine störenden morphologischen Abnormalitäten aufweisen, untersucht. Durch transgene Expression einer dominant-negativen $K_v7.2$ Porenmutante mit einem Tet-Off System werden hippocampale elektrophysiologische Parameter K_v7/M-Strom-defizienter Mäuse mit denen von Kontrollmäusen verglichen. Theta- (4-12 Hz) und Gammaoszillationen (30-100 Hz) während *Rapid eye movement* (REM)-Schlafs, sowie *Sharp-Wave Ripple* (SW-R)-Komplexe im Tiefschlaf (*slow wave sleep* (SWS)) werden off-line analysiert in Ableitungen von schlafenden Tieren vor und nach Verhaltenstests. Einzelzellaktivitäten wurden in Aufnahmen von Schlafphasen vor Verhaltenstests analysiert. Die Verhaltenstests umfassten sog. *spatial novelty* Tests, einen Ein-Trial-Test für räumliches Gedächtnis (*single trial spatial memory* – STSM) und das Y-Labyrinth. Theta- und Gammaoszillationen während des Laufens wurden ebenfalls analysiert. Die LFP K_v7/M-Stromdefizienter Mäuse sind signifikant verändert und zeigen verminderte Theta- und Gammaintensitäten, sowie kleinere sharp-waves und ripples. Die grundlegenden Eigenschaften der Einzelzellaktivitäten waren unverändert. Die geschwindigkeitsabhängige Theta- und Gammamodulation, sowie die Veränderungen der LFP im Schlaf vor und nach Verhaltenstests waren vergleichbar zwischen den Gruppen. In Verhaltensexperimenten zeigten K_v7/M-Stromdefiziente Tiere schwächere Leistungen im Y-Labyrinth mit einer Tendenz zu verschlechtertem Gedächtnis nach 24 Std im STSM Test. Als umfassende Erklärung sowohl für die elektrophysiologischen Befunde, als auch für die bereits beschriebene Übererregbarkeit wird ein homöostatisch kompensierender Mechanismus vorgeschlagen, der zumindest zum Teil auf synaptischer Ebene wirkt. Die Ergebnisse dieser Arbeit tragen somit zu dem generellen Verständnis der Effekte chronischer M-Stromdefizienz auf das Säugerhirn bei und bieten Anregungen für weitere Experimente.

Contents

Introduction

1.1 Origin of transmembrane ionic currents

For all cells, a membrane consisting of a hydrophobic, ion-impermeable lipid bilayer separates the intracellular and extracellular spaces of neurons (121). Ion pumps actively transport ions across this membrane and, due to selective passive permeability, create a concentration gradient-induced force towards the Donnan equilibrium (60; 87). A second force at play is that of the electric repulsion/attraction forces on the charged ions. These two forces taken together create an ion-specific electrochemical gradient, that is, an electromotive force (EMF), driving ionic fluxes across the membrane through selective ion channels (60; 87). Upon the opening of an ion channel, the EMF for any ion is determined by the difference between the instantaneous membrane potential and the ion's equilibrium potential, or $E_{m,ion}$, calculated according to the Nernst equation,

$$E_{m,ion} = \frac{RT}{zF} ln \frac{[ion]_o}{[ion]_i} \tag{1.1.1}$$

where R is the ideal gas constant, T is the temperature, z is the charge of the ion, F is the Faraday constant and $[ion]_i$ and $[ion]_o$ are the intra- and extracellular ion concentrations, respectively.

The neural equilibrium potential, or $E_{m,neuron}$, mostly depends on Na^+, K^+ and Cl^- according to the Goldman equation (64),

$$E_{m,neuron} = \frac{RT}{F} ln \frac{P_K[K^+]_o + P_{Na}[Na^+]_o + P_{Cl}[Cl^-]_i}{P_K[K^+]_i + P_{Na}[Na^+]_i + P_{Cl}[Cl^-]_o} \tag{1.1.2}$$

where P_{ion} is the respective ionic permeability, set by ion channels. In the absence of extracellular input, $E_{m,neuron}$ equals the resting membrane potential (RMP).

While equation 1.1.2 can be used to calculate the RMP, Figure 1 utilizes a model derived from electrical circuits to allow calculation of how quickly a neuron can reach the RMP, intrinsically representing ion channels with current conductance g_{ion}.The total conductance, G - a linear addition of individual components - is the inverse of the neuron's input resistance R and related to the membrane potential V_m according to Ohm's law,

$$G = \frac{I}{V}, \quad R = \frac{V}{I} \tag{1.1.3}$$

where I is the total ionic current across the neuron. Currents can be either repolarizing, hyperpolarizing or depolarizing, where $I > 0$ for inward currents.

Central nervous system (CNS) neurons are synaptically excited or inhibited. The main excitatory neurotransmitter glutamate can evoke an excitatory postsynaptic potential (EPSP) by stimulating an influx of Na^+ and/or Ca^{2+} through ionotropic receptors such as those for N-methyl-D-aspartic acid (NMDA), α-amino-3-hydroxy-5-methyl-4-isoxazolepropionic acid (AMPA) and kainate (43; 113; 130; 160). Release of γ-aminobutyric acid (GABA), the main inhibitory neurotransmitter in the adult brain, can evoke an inhibitory postsynaptic potential (IPSP) through Cl^- permeable GABA-receptors (98; 135; 163). As E_{m,Cl^-} is close to the RMP, only low Cl^- currents occur in resting neurons. However, increased chloride permeability leads to shunting, which

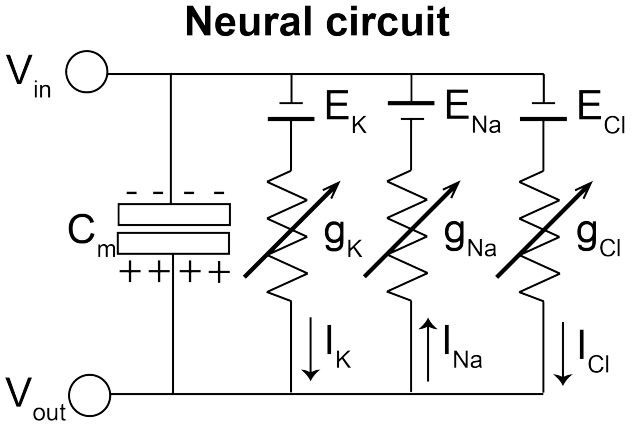

Modified from (87)

Figure 1: An equivalent electrical circuit representing the main contributors to the establishment of the membrane potential. C_m is the membrane capacitance which is proportional to the cell surface area, E_{ion} represent the equilibrium potentials for individual ions according to eq. 1.1.1 and g_{ion} are the conductances, variable by ion concentrations, ligand-binding, voltage-gating, expression patterns, second messengers, etc. Note the inverted direction for I_K and I_{Na}.

decreases EPSP amplitudes. Synaptic input is, therefore, able to induce changes in V_m through excitatory postsynaptic currents (EPSC) and inhibitory postsynaptic currents (IPSC) generated by ionotropic receptors, as well as through other ion channels opened secondarily by metabotropic receptors.

1.1.1 Voltage-gated ion channels

Transfer of received information to another neuron or muscle requires a second class of ion channels that undergo a conformational change when exposed to a change in V_m (25). Upon a ΔV_m, such as is caused by EPSPs or IPSPs, the channel's time constant τ_c determines how quickly it can adjust its open probability P (77) according to

$$P(t) = P(0) + [P(\infty) - P(0)][1 - e^{\frac{-t}{\tau_c}}] \tag{1.1.4}$$

where P_0 is the initial open probability and P_∞ is the steady state open probability for the new V_m. The kinetics of voltage-gated ion channels determine how fast the channels open or close upon a change in the membrane potential. If the membrane potential changes transiently and more quickly than the activation time constant of a particular ion channel, it will not change its open probability. For temporal EPSP summation, the timing of stimulation is similarly important because subthreshold EPSPs can sum up to cross the threshold necessary for action potential (AP) generation, i.e. they can create a superthreshold stimulation. Most voltage-gated ion channels pass Na^+, K^+, Ca^{2+} and/or Cl^- (32; 146), where a channel's ion selectivity allows permeability for one ion to be higher compared to others (76). Their overall activity and voltage dependent response can be controlled by G-protein coupled receptor mediated phosphatidylinositol-4,5-bisphosphate (PIP2) and second messengers such as cyclic adenosine monophosphate (cAMP) (62) or pH (27).

In hippocampal neurons, four major repolarizing voltage-gated K^+ currents have been described: I_{K}, I_{A}, I_{D} and I_{M} (76; 172), the last being the subject of this thesis.

1.2 The Local Field Potential

Intracranial neural oscillatory activity in rodents was first recorded in 1964 (183) by using transmembrane currents to induce a change in the extracellular potential difference V_{ex}, referred to as the local field potential (LFP), between a measuring electrode and a reference. Usually, there are three types of electrodes used to measure the LFP: glass electrodes (95), wires (single wires, stereotrodes (114) and tetrodes (66)) and silicon probes (14). Simultaneously recording from the same position with multiple, closely spaced electrodes increases the chance of recording APs from many different neurons. In addition, these recordings allow computer algorithms to cluster similar APs in order to more successfully isolate the spikes of individual neurons (70). Linear silicon probes with less densely spaced recording sites, on the other hand, allow anatomically distinct regions to be recorded.

1.2.1 Physiological contributions to the LFP

It is important to understand which transmembrane currents contribute most to the recorded LFP. Single fast events like APs show high enough currents to be measurable. However, the extracellular space serves as a low-pass filter, so that APs are only measurable close to their respective somas or dendrites (6). Individual PSCs are too small for detection but provide a broad enough time window to superimpose with co-occurring synaptic events, which increases total transmembrane current flow.

The main physiological contributor to the LFP is still debatable, with one review suggesting synaptic activity is the main contributor (21) and a more recent neocortical modeling approach suggesting that active currents dominate the generation of LFPs (143). Volume conduction, considered in more detail below, also contributes to the recorded LFP.

1.2.2 Volume conduction

As current passes into a neuron, e.g. during an EPSC, ΔV_{ex} is less than 0, which is termed a sink (Figure 2). This depolarizing current leaks out of the neuron away from the site of the sink, so here, ΔV_{ex} is positive: a passive return current - or source - can be measured (87). The presence of spatially separated sinks and sources results in a dipole or even tripole, which gives rise to an electric field passing through the brain tissue; this is referred to as volume conduction, and is depicted in Figure 2 (6; 105; 88). This effect complicates measurement of local currents, and tends to blur evoked currents and overshadow smaller neighboring events. It is, however, indispensable for recording an electroencephalogram (EEG). The sinks and sources in the signal are approximated by calculating the current source density (CSD) (57). Volume conduction does not seem to be only an epiphenomenon of synchronous activity as the endogenous volume-conducted field can affect neighboring neurons and, for example, increase their synchronous firing (83).

In summary, synaptic and intrinsic currents and the volume conduction they generate are the main components of the LFP. To measure an LFP, the total transmembrane current, I_{tot}, must be sufficiently large. Therefore, several criteria need to be met. [1] If two neighboring neurons have current flows that are similar in amplitude but are inverted in direction, then I_{tot} will equal 0. Local currents, therefore, should be unidirectional or separated in time. [2] Even if the first criterion is met, in an arbitrarily arranged neural network, sinks and sources would cancel each other out. Therefore, the existence of a layered structure is an additional requirement (47; 49; 93). Still,

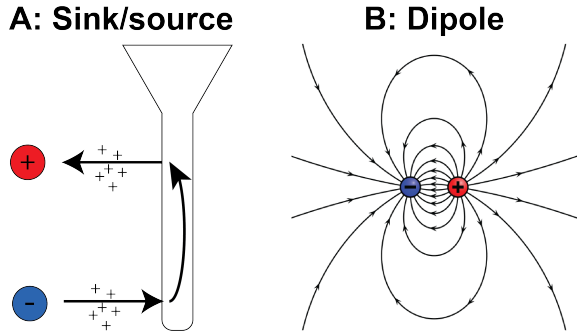

Figure 2: Volume conduction of ionic currents. **A:** Current inputs (negative sink) into the dendrite of a schematic pyramidal neuron generate an instantaneous outward current away from the injection site (positive source). **B:** Sinks and sources create a electric field that travels through the brain tissue.

caution is required if attempting to translate calculated currents into a local membrane potential change, since a source at the soma might reflect active local inhibitory synaptic conductance or passive return currents of excitatory inputs along the dendritic arbor (21).

1.3 Resonance

Oscillations of the membrane potential arise predominantly due to synchronous synaptic activity (21). Some neurons can tune their membrane response to specific stimulation frequencies when their cellular features display resonance (173). In this case, a fixed amplitude stimulation at the neuron's resonance frequency will induce the largest change in the membrane potential, i.e. the change in the neuron's membrane potential becomes a non-linear sum of individual events.

Resonance in neurons can be divided into two categories, each with their own set of properties: dendritic resonance, when synapses show a preference for a specific presynaptic firing rate; and somatic resonance, when summed transmembrane currents attuned to the neuron's resonance frequency induce a maximum change in the membrane potential. Since K_v7/M-current-generating channels localize to somas and axons, only neural resonance need be considered further as it applies to changes in the membrane conductance in an oscillatory manner. This will then result in a larger change of the membrane potential, if the input current follows the resonant frequency. A schematic depiction of a resonant electrical circuit is shown in Figure 1.3A.

In neurons, current injections are non-continuous, hence the frequency of the current f_i is larger than 0. In this case, eq. 1.1.3 becomes

$$G(f_i) = \frac{\Delta I_{tot}(f_i)}{\Delta V_m}, \quad Z(f_i) = \frac{\Delta V_m}{\Delta I_{tot}(f_i)} \tag{1.3.1}$$

where $Z(f_i)$, impedance, is the common term for frequency dependent resistance (2).

Passive membrane properties, present in all neurons, serve as the low-pass component. A passive neuron consists of a membrane and a persistent leak resistance, R_{leak}, which behaves like a capacitor and a resistor, respectively, set in parallel (Figure 1.3). When a voltage is applied to the neuron, current flows through the capacitor according to

$$I(t) = I(0)e^{-t/\tau_m} \tag{1.3.2}$$

where $I(0)$ is the initial current according to $I(0) = V/R_1$ and τ_m is the membrane time constant according to $\tau_m = C_m * R_1$. After an infinite amount of time, the current reduces to 0: current can no longer flow through the fully charged capacitor, but rather only through R_{leak}. Therefore, if

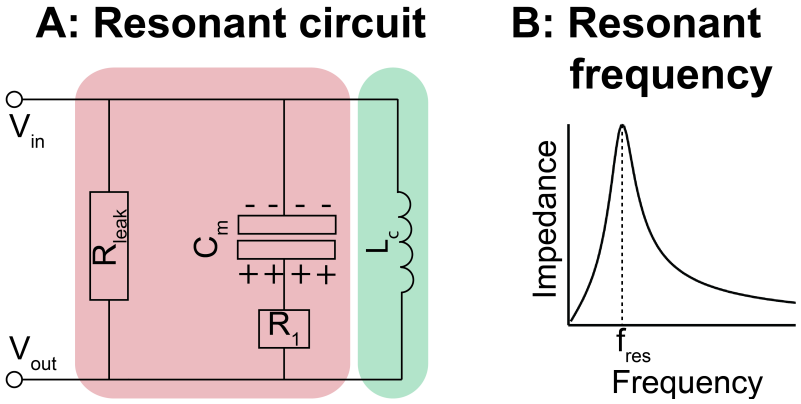

Figure 3: Inductive and conductive properties can result in a resonant circuit. **A:** An electrical circuit representation for a bandpass filter. **Red box:** Passive membrane properties. Applying a voltage across the membrane will cause a current to flow which charges the capacitor. After an infinite amount of time ($t \to \infty$) the voltage across the capacitor equals the applied voltage. Current can now only flow through the leak channels R_{leak}. Therefore, for low frequency currents ($f_i \to 0$), the membrane impedance $Z_m(f_i \to 0) = R_{leak}$. If the applied voltage's polarity switches infinitely fast back and forth, there is no time available for a current to charge the membrane, which, as a result, has a resistance of 0. Therefore, for high frequency currents ($f_i \to \infty$), $Z_m(f_i \to \infty) < R_{leak}$. **Green box:** An inductor, representative of inductor-like properties of certain voltage-gated channels, has an impedance which is positively correlated with the frequency of the current through it, so $Z_c(f_i \to 0) = 0$ and thus for $Z_c(f_i \to \infty) = \infty$. **B:** This neural circuit acts as a band-pass filter due to its inductive and capacitive properties, where impedance is highest at the resonance frequency f_{res}.

the input frequency f_i approaches 0, the impedance Z_m equals R_{leak}. For an infinitely high input frequency, the capacitor doesn't charge and so offers no resistance. Current can now flow through both R_{leak} and R_1, reducing the total resistance. Therefore,

$$Z_m(f_i \to \infty) = \frac{R_{leak} * R_1}{R_{leak} + R_1} < R_{leak} \tag{1.3.3}$$

Applying the membrane's impedance properties to eq. 1.3.1 shows that low frequency currents induce a higher ΔV_m.

Voltage-gated ion channels can give rise to a high-pass component if they conform to several principles (82). First, they must not inactivate. Second, their open probability P and ion specificity must be such that if the change of the membrane potential, V_m, is positive, then the change in the conducting current, I_c, must be negative and vice versa, i.e. they must have inductor-like properties. Suppose that at V_m = -50 mV and $t = 0$ the ion channel's resistance is $R_c(0)$. If V_m oscillates around -50 mV a lot faster than τ_c (see eq. 1.1.4), ion channels will not show any significant changes in P, which results in channel resistance remaining close to R_c. Therefore, as the input frequency approaches infinity, the impedance equals $R_c(0)$. In contrast, at slower frequencies, P does change. The membrane will now become leaky and so the resistance at lower frequencies is less than $R_c(0)$. In Figure 1.3, this is represented by an inductor L_c which has reduced resistance at lower frequencies.

A neuron's conductive property is a weighted average of both passive membrane properties and voltage-gated ion channels,

$$Z_{neuron} = \frac{Z_m * Z_c}{Z_m + Z_c} \tag{1.3.4}$$

If the third condition for voltage-gated ion channels is met, namely that $\tau_c > \tau_m$, Z_{neuron} is reduced at low and high frequencies, but peaks in-between at resonant frequency f_{res}, depicted in

B. As a result, the neurons acts as a band pass filter. K_v7/M-channels meet these three criteria (non-inactivated, inductor-like properties and $\tau_c > \tau_m$) and therefore contribute to establishing a resonance frequency (81; 80).

Output networks tune their response to the synchronous input from modeled feedforward networks (1), allowing subthreshold membrane oscillations to task-dependently gate information between neural structures by increasing their coherence (5; 8; 67; 118).

One brain region that is being intensively studied by measuring the LFP and intrinsic neural resonances is the hippocampus, due both to its layered structure and connectivity as well as its role in behaviorally relevant paradigms.

1.4 The hippocampus

Located beneath the cortical surface within the medial temporal lobe in primates, the hippocampus is part of the limbic system (3). It has been implicated in several processes including memory and spatial orientation (18; 20; 24; 84; 188), and is a well-studied structure with respect to short- and long-term synaptic plasticity – processes that are thought to be important for learning and memory (10; 109). The hippocampus forms a curved structure and an extension of the cortex. Due to its curvature and inverted position found particularly in rodents, anatomists describe more superficial layers of the hippocampus as located "further away" or "distal", while deeper layers are considered "closer" or "proximal" to the neocortical surface. In this thesis, the terms used to describe the relative position of the hippocampal layers are geometrical in nature, such that 'up' or 'above' means closer to the cortical surface.

The structure of the hippocampus resembles two half-circles enveloping each other (Figure 4). Along the neocortex-CA1-dentate gyrus (DG) axis, the order of the hippocampal layers are (from top to bottom): stratum oriens (str. Or), which contains the basal dendrites; stratum pyramidale (str. Pyr), a dense pyramidal cell body layer; stratum radiatum (str. Rad), which contains the apical proximal dendrites; and stratum lacunosum moleculare (str. LM), with the apical distal dendrites.

The main hippocampal input comes from the entorhinal cortex (EC) through the perforant path (PP), which innervates the distal dendrites of the DG, CA3, and CA1. The DG projects towards area/layer CA3 through mossy fibers to the CA3 proximal dendrites. From CA3, projections are made through the Schaffer collateral (SC) onto the proximal dendrites of CA1 in str. Rad, through the commissural fibers to the contralateral hippocampus as well as recurrent connections back to CA3. CA1 gets its input from CA3 in str. Rad and from the EC into str. LM. The main hippocampal output is guided through axons that initiate from the str. Pyr and terminate in deep EC layers. The EC-DG-CA3-CA1 path is often referred to as the trisynaptic pathway.

1.4.1 Hippocampal oscillations

Neural oscillations are classified according to their frequency bands (23). Neighboring frequency bands within the same neuronal network are typically associated with different brain states and compete with each other (36; 96). However, several rhythms can temporally coexist in the same or different structures and can interact with each other (36; 106; 176).

Several types of oscillations are observed within the hippocampus (178). This thesis is focused on two distinct oscillatory patterns of the hippocampus in CA1. The first is the co-occurrence of

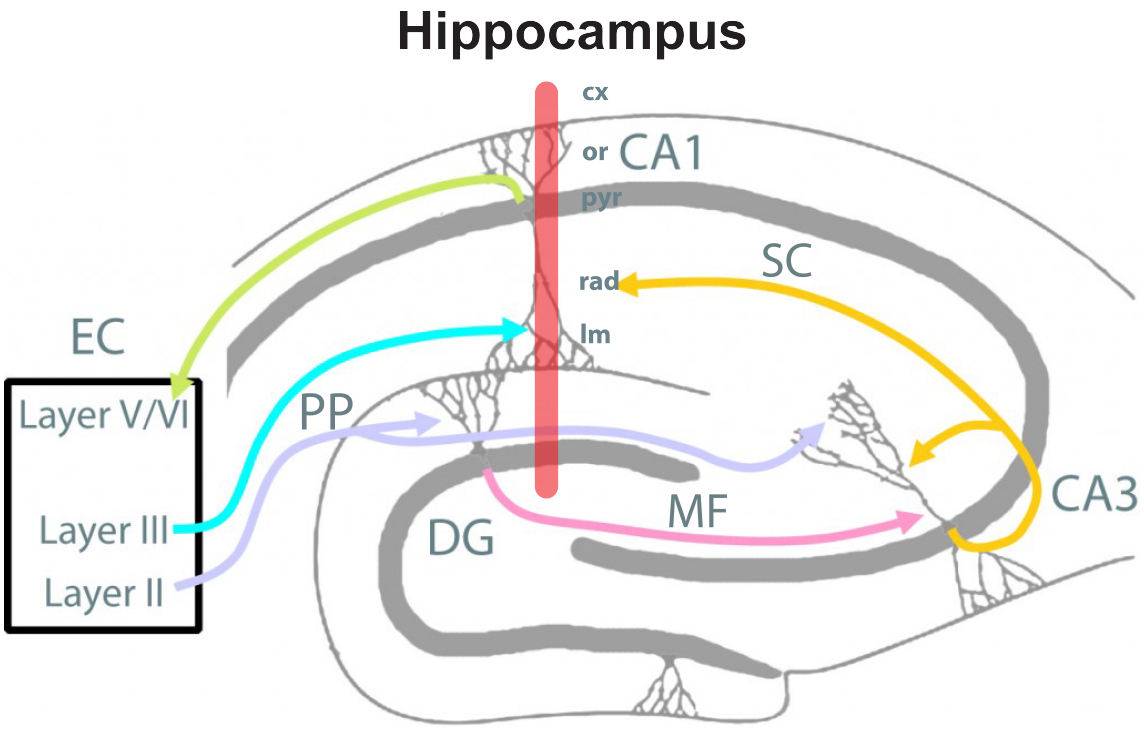

Figure 4: A representation of the subareas of the hippocampus. The entorhinal cortex (EC) is the main input into the hippocampus through the perforant path (PP). Layer II projects towards dentate gyrus (DG) and CA3. DG outputs through mossy fibers (MF) into CA3, where it is combined with the direct PP input and in its turn outputs to itself through strong recurrent loops and towards CA1 through Schaffer collaterals (SC). CA1 combines both SC and PP input and outputs back to layer V/VI of the EC. The EC-DG-CA3-CA1 is referred to as the trisynaptic pathway. The red bar indicates the position of a linear probe, inserted along the neocortical CA1-DG axis. Layers from top to bottom: cx-cortex, or-oriens, pyr-pyramidale, rad-radiatum, lm-lacunosum moleculare. Modified from (134).

theta (4-12 Hz) and gamma (30-100 Hz) oscillatory rhythms. The second is the co-occurrence of high-frequency ripples (100-250 Hz) together with a sharp wave (SW), which is referred to as a sharp wave ripple (SW-R) complex.

1.4.2 Theta and gamma oscilations

Investigation of theta oscillations in CA1 *in-vivo* and *in-vitro* has shown that two relatively independent forms of theta exist: an acetylcholine-induced atropine-sensitive theta rhythm that is thought to be intrinsically generated in CA3 that projects to CA1 in str. Rad and a non-cholinergic atropine-insensitive oscillation, generated in EC, that projects to CA1 in str. LM (19; 94; 177). The existence of the CA3-generated theta current was seen after removal of the EC, which strongly decreased but did not completely abolish theta current generation in CA1 (15; 89). When the depth profile of theta oscillations is observed along the neocortical-CA1-DG axis, a gradual 180° phase shift can be seen between str. Pyr and str. LM. The gradual shift, rather than an abrupt 180° inversion, confirms the presence of several phase-shifted dipoles (15; 22).

Intrinsic resonance in pyramidal cells allows them to follow theta-modulated synaptic input more closely (172). The medial septum is required as a theta rhythm generator, as a lesion of the medial septum activity can abolish all theta oscillations in all cortical regions (136). The

activity of CA1 neurons is rhythmically modulated by the direct afferent input from glutamatergic, cholinergic, and GABAergic neurons of the medial septal nucleus and the nucleus of diagonal band (165; 115). Medial septal neurons target hippocampal interneurons, a subgroup of which project back to the medial septum (44). Indeed, glutamatergic medial septal input corresponds to the emergence of theta band oscillations prior to and during locomotion (59). The theta susceptibility of neurons is shown by the possibility that a robust long-term potentiation (LTP) can be induced when the neuron is stimulated at theta frequencies (50).

The generation of the gamma rhythm is different (101), and strongly correlates with the actions of perisomatic inhibitory interneurons (31; 58; 167). In contrast to CA1, CA3 can internally generate a gamma frequency oscillation by a recurring pyramidal cell (PC)-interneuron circuitry (110; 187) and project this frequency to CA1 via the SC, as cholinergic stimulation in CA3-CA1 lesioned hippocampal slices results in abolished gamma oscillations in CA1 but leaves them intact in CA3 (53).

In contrast to theta oscillations, gamma oscillations are not continuous, but wax and wane with theta frequency (15; 30; 168). Gamma oscillations in the hippocampus are strongest when co-occurring with the theta rhythm (15; 102; 174), as seen by an increase in gamma power in the dentate gyrus during theta-associated tasks (36). Not all neurons fire APs phase locked to gamma oscillations, as only coherent groups of neurons are selected by gamma oscillations on each theta cycle (154).

During spatial navigation, a subpopulation of CA1 pyramidal cells act as place cells (125; 124), i.e. they specifically fire at a place within the animal's environment, phase locked to the trough of the measured theta rhythm. Place cells show phase precession (126): when the animal passes through their place fields, they fire APs on increasingly earlier theta phases; their maximum firing rate is reached at the center of the place field on the trough of the str. Pyr LFP theta cycle. During a single theta cycle, assemblies of place cells sequentially fire by the order along the animal's path (164), which can be used to predict future planning (131; 138). This, together with many later discoveries, gives rise to the hypothesis that hippocampal CA1 place cells and theta rhythm are important in spatial navigation (24; 184).

1.4.3 Sharp-wave ripples

During rest, while awake or during slow-wave sleep (SWS), CA1 shows short-lived SW-R complexes (Figure 5). Ripple generation occurs in CA2/CA3, where reciprocal connections exist between pyramidal cells (127; 189). Here pyramidal cells initially fire non-synchronously, but when a critical firing rate is reached a local circuitry involving both pyramidal cells and PV-positive interneurons generates the typical high–frequency pattern seen in the CA3 pyramidal layer (148). Additionally, an increase in neural excitability in an *in-vitro* setup is positively related to ripple occurrence (148). The output from CA3 travels to CA1 through the Schaffer collaterals and generates a large sink in CA1 str. Rad (28; 193) where the local interplay between pyramidal cells and various types of interneurons (92; 145) contribute to the generation of the typical 100-250 Hz ripples in CA1 str. Pyr. Only pyramidal neurons that are sufficiently depolarized to overcome the simultaneous inhibition will fire on the troughs of str. Pyr ripples (37).

1.4.4 Memory and oscillatory patterns

Both ripples and theta/gamma oscillations are involved in proper memory formation. Rapid eye movement (REM) sleep deprivation has been shown to negatively affect memory-based tasks in rodents (55; 141). A modeling approach to REM sleep suggests neuronal reactivation (72), but empirical evidence during REM sleep is ambigious - while a few studies favor neuronal reactivation (74; 107; 132; 140), others do not (16; 99), and many studies do not include analysis of REM sleep. Several studies found that impairment of memory correlated with a decrease in theta and/or gamma oscillations (4; 58; 97; 123; 142; 184). A recent study designed to suppress theta oscillations

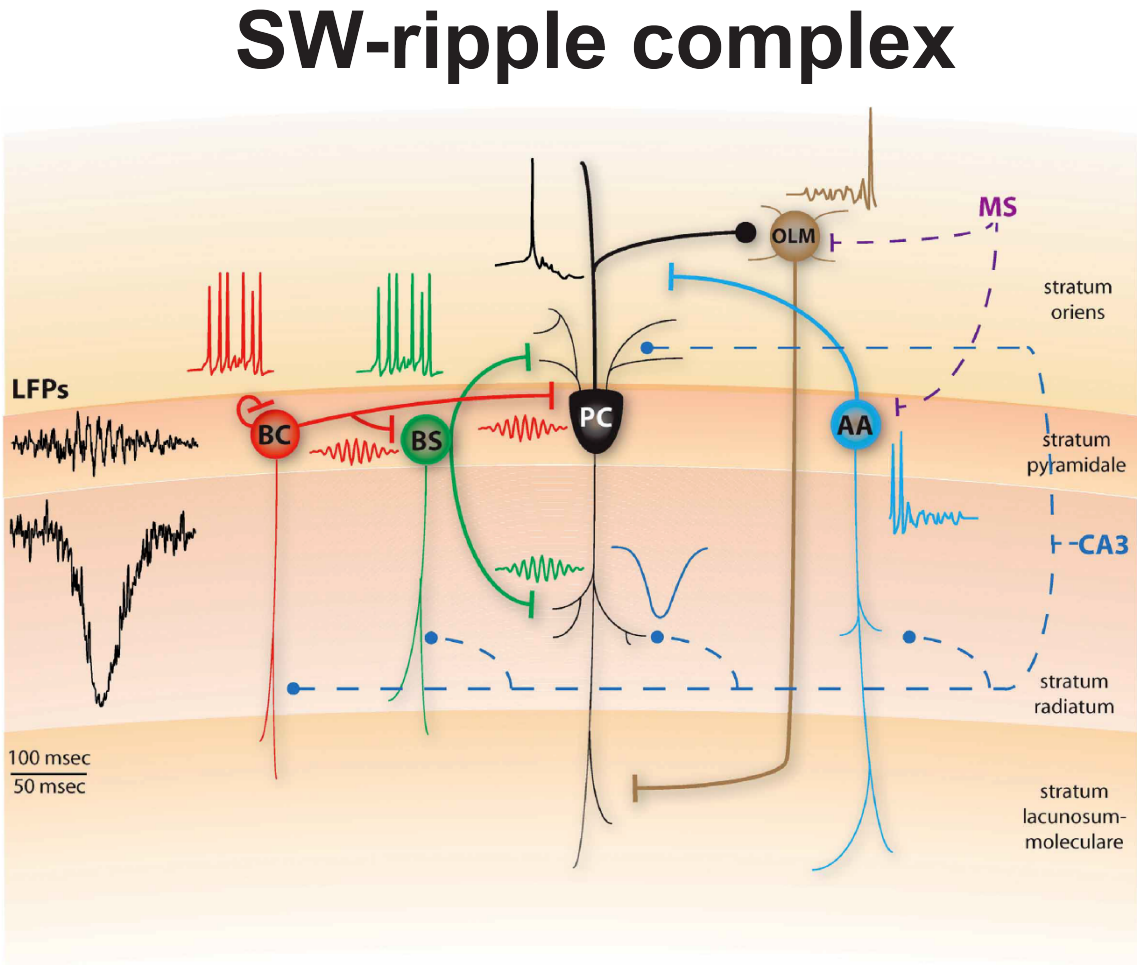

Figure 5: Schematic diagram of a conceptual SW-R model, including pyramidal cells (PC), basket cells (BC), bistratified cells (BS), axo-axonic cells (AAC) and oriens-lacunosum moleculare cells (OLM). Thin lines represent dendritic arborizations, and thick lines arerepresent the axonal ones. Dashed lines represent inputs coming from CA3 through the Schaffer collaterals (blue) or the medial septum (MS, purple). The representative spiking activity of BS, BC and PC cells during SW-Rs is shown above the corresponding cells. In the model, the BS cells will respond to the CA3 input by fast-spiking, which abolishes dendritic electrogenesis and somatic bursting in the PCs. BC cells also spike fast, and due to their recurrent inhibition, synchronize their firing in ripple frequencies, imposing this rhythm on the BS population as well (red and green ripple-frequency spikes). Hence, PCs receive synchronous ripple-frequency inhibitory inputs in their dendritic and perisomatic areas (green and red ripples), along with excitatory input in their apical dendrites (blue, sharp-wave), yielding ripple-frequency intracellular oscillations and ripple phase-locked sparse firing (black trace). A schematic SW-R LFP that would result from this activity is shown on the left. Top timescale corresponds to LFPs; bottom one to all spiking and synaptic traces. All traces are conceptual and start at the same time point. Reprinted from (37).

specifically during REM sleep showed impaired contextual memory in mice (13).

During SW-Rs, ensembles of place cells acquired during exploration replay their sequential activity at a faster timescale (42; 45; 164). A large number of simultaneously recruited PCs render the SW-R suitable for inducing LTP in their downstream targets (7; 46). Electrical disturbance of the neural network for inhibition of ripple formation during post-task sleep results in a decreased performance in subsequently performed memory-dependent tasks (63; 48), lending credibility to the claim that SW-Rs are necessary to transfer short-term memories to into long-term cortical memories (112; 170).

1.5 K_v7/M-channels

In humans and in mice, the five distinct subunits used for the constructions of tetrameric K_v7/M-channels, encoded by five genes (*KCNQ1-5*), are part of the K_v7 family. Each subunit has six transmembrane domains, a voltage sensor and pore loop/selectivity filter (Figure 6). $K_v7.1$ is highly expressed in cardiac tissue, where it plays a crucial role in shaping the action potential (86). Neural $K_v7.2$-5 subunits form either homomeric or heteromeric K_v7/M-channels. These are pharmacologically modulated to varying extents according to their subtype composition (75; 104; 191), but not all combinations are capable of interacting with each other in vitro. $K_v7.2$ and 7.3 are most abundantly expressed across the brain and form heteromeric channels, whereas $K_v7.3$ additionally forms heteromeric channels with the lesser-expressed $K_v7.5$ (150; 157). This results in stoichiometrically heterogenic K_v7/M-currents (100; 85). Exclusive expression of either $K_v7.2$ or 7.3 shows reduced currents when compared to co-expression of both (158). The higher amplitudes of $K_v7.2/7.3$ heteromeric channels is mediated by increased transport to the plasma membrane (152) together with a higher single channel conductance (153).

K_v7/M-channels are localized to the axon initial segment (AIS) and to nodes of Ranvier of

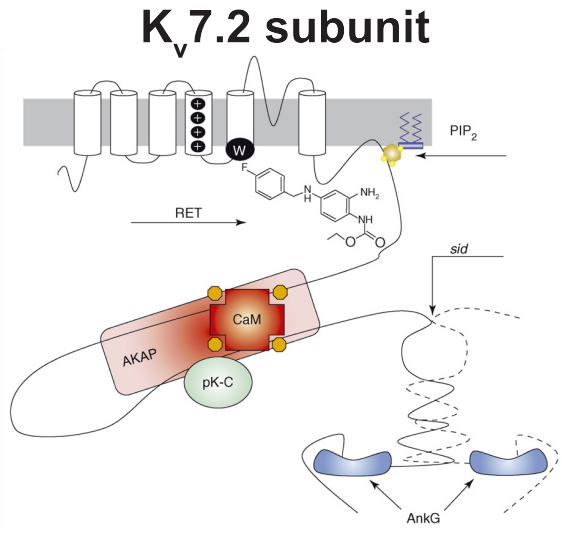

Figure 6: Schematic representation of a single $K_v7.2$ subunit. The W at position 236 in the S5 domain is the main binding site for retigabine (whose chemical structure is shown next to the binding site). sid: subunit interaction domain; CaM: calmodulin; AKAP: A-kinase-anchoring protein; pK-C: protein kinase C; Ank-G: ankyrin-G. The approximate position of the binding domain for PIP2 in the C-terminus is also indicated. The C-terminal end of a second subunit, including the sid, is shown by a dotted line. Reprinted from (116).

principal neurons and parvalbumin (PV)-positive interneurons (29; 34; 41), where they pass a non-inactivating re- or hyperpolarizing K^+ current. K_v7/M-channels activate slowly (100ms< τ_M <200ms) at depolarized potentials from about -60 mV. These channels are therefore capable of suppressing continuous AP generation in a process called spike frequency adaption (171; 108). They also close slowly, thereby contributing to the medium/slow afterhyperpolarization (AHP) (182; 68). Additionally, because the open probability of K_v7/M-channels does not equal 0 around -60 mV, they likely contribute to setting the RMP and resting conductance. The K_v7/M-channel activity is regulated by the concentration of membrane-bound PIP2, which is hydrolyzed by phospholipase C upon muscarinic acetylcholine (ACh) G_q-coupled receptor stimulation (hence the name M-current) (17; 103). They can be pharmacologically blocked by XE991 or linopirdine and activated by retigabine or flupirtine (116). Intracellular Ca^{2+} inhibits K_v7/M-channel activity through Calmodulin binding in the C-terminus (61).

1.5.1 K_v7/M-channels in epilepsy

An epileptic seizure is defined as a transient occurrence of signs and/or symptoms due to abnormal excessive or synchronous neuronal activity in the brain (54). Epilepsy is defined as a disorder of the brain characterized by an enduring predisposition to generate epileptic seizures, and by the neurobiological, cognitive, psychological, and social consequences of this condition. The definition of epilepsy requires the occurrence of at least one epileptic seizure (54). Approximately 60% of epilepsies are idiopathic, i.e. they can likely be attributed to a genetic disposition (90), whereas acquired epilepsies can be caused by tumors, cerebral hypoxia, trauma, infections, or neurological diseases (190).

Proper K_v/M-channel function is shown to be highly relevant for neural circuit excitability, due to its relation to epilepsy. K_v7/M-channels are the target of the new anticonvulsant retigabine, which increases their activity (38). Decreased K_v7/M-currents in patients with mutations in either $K_v7.2$ or $K_v7.3$ subunits can lead to benign familial neonatal convulsions (BFNC) (186), which is inherited in an autosomal dominant pattern (85). Mutations in *KCNQ2* can also cause $K_v7.2$ epileptic encephalopathy (186), also in the case of a gain-of-function mutation (40).

Case studies suggest most BFNC mutations are not dominant-negative, but rather dosage dependent (9; 162). Full-term infants with BFNC experience seizures during the first postnatal weeks after which they remit. Although there is an increased risk of epileptic seizures during adulthood, BFNC is considered to be a self-limiting condition. Some patients, however, show a more severe form of epileptic encephalopathy and mutations may exhibit a dominant-negative effect, indicating that the exact position of the mutation strongly affects a patient's prognosis (128). Pre-term infants show a delayed onset and remission, suggesting a development-dependent epileptogenic effect of K_v7/M-current deficiencies (144). Seizures that are not primarily caused by K_v7/M-channel mutations do not cause a change in K_v7/M-current due to seizure activity (35; 155), although K_v7 expression can be regulated by neuronal activity (194).

1.5.2 Mouse models for K_v7/M-current deficiencies

To generate a rodent model for K_v7/M-current deficiencies, several approaches are available. Genetic deletion of K_v 7.2 in mice is lethal (185). Heterozygous $K_v7.2$ animals do not show an epileptic phenotype, despite expressing only half of the $K_v7.2$ protein, although a decreased seizure threshold was observed (185). A mouse model of a temporally controlled neuron-specific expression

of a dominant-negative $K_v7.2$ pore mutant (133), developed in our lab, showed that suppression of K_v7/M-currents solely during the first two postnatal weeks was sufficient to induce epileptic seizures and cerebral morphological abnormalities. This developmental implication of K_v7/M-currents was discovered upon expressing the pore mutant from conception throughout adulthood except for the critical period of two weeks postnatal, which resulted in morphologically similar hippocampi (133). Mice with a V182M mutation in the S3-helix of $K_v7.2$ died during the first postnatal weeks, which could be partially rescued by application of retigabine (117). Other genetic missense mutations linked to human BFNC showed reduced seizure thresholds and spontaneous generalized tonic-clonic seizures (161).

1.5.3 K_v7/M-currents and neural resonance

Neural resonance requires that voltage-gated ion channels meet three criteria: (a) they must not inactivate, (b) their open probabilities and passed current should be such that they oppose a change of the membrane potential, and (c) their activation constant τ_c has to be longer than the membrane constant τ_m (See Chapter 1.3).

K_v7/M-channels meet all three criteria, or rather, neurons expressing functional K_v7/M-channels show somatic subthreshold resonance (81). It is, therefore, understandable that blocking K_v7/M-channels by application of XE991 abolishes the resonance peak seen at subthreshold depolarized potentials (80). XE991 application suggests a decrease in hippocampal theta oscillations in live mice (56), and leads to a decrease in both theta and gamma oscillations in slices (11; 139).

1.6 The project

Patients carrying *KCNQ2* mutations may show cognitive problems and mental retardation (12; 186). However, it is unclear whether retardation is a side effect of the seizures to which these individuals were exposed, a reduction in K_v7/M-currents during development, a reduction in K_v7/M-currents in adulthood, or any of these factors combined. In contrast, acetylcholine release-increasing, K_v7/M-channel-suppressing linopirdine has been considered a cognition enhancer (33) and attenuation of K_v7/M-channel activity by application of XE991 shows cognitive improvement in a novel object recognition task. Additionally, application of XE991 in urethane-anesthetized rats makes CA1 not only more susceptible to LTP induction, but the degree of LTP induction increases as well (169). The opposing effects of an acute attenuation of K_v7/M-currents, that is, the improvement of cognition vs. clinical observation of reduced cognitive function in *KNCQ2*-mutated patients (12; 186) might be related to a prolonged reduction in K_v7/M-current activity, which may induce a compensatory mechanism. Furthermore, acutely abolishing K_v7/M-currents through application of XE991 (56) neither mimics K_v7/M-current deficiencies during learning nor during post-task sleep as one would expect in chronic K_v7/M-current patients.

Non-epileptic, morphologically similar mice chronically deficient in K_v7/M-currents can be generated using the temporally controlled $K_v7.2$ dominant-negative approach (133). Single-cell recordings in these mice have shown that pyramidal cells in CA1 are hyperexcitable due to a loss of K_v7/M-current, because XE991 application cannot increase firing rates in mutants any further when a depolarizing current is applied, in contrast to controls (133). Admittedly, this genetic approach does not accurately reflect the situation in human patients affected by BFNC: a temporally controlled dominant-negative subunit expressed in addition to endogenously ecxpressed

subunits (mouse model) vs. a permanently present dosage-dependent mutation (patients) (9; 162). However, it is not the goal of this thesis to mimic a *KCNQ2*-mutation related encephalopathic phenotype. Rather, the purpose is to try to further understand the function of K_v7/M-currents during adulthood, their contribution to recorded LFPs, and their effect on behavior. To this end, the use of this mouse model is ideal because suppression of the expression of the dominant-negative subunit solely during the first two weeks of life shows no evidence of developmental constraints on the maturation of the brain and abolishes epileptic seizures (which can both have a secondary effect on neural function and obscure the readout of behavioral tests), while K_v7/M-currents are strongly impaired in adults (133).

1.6.1 Hypotheses

These previously generated mice (133) revealed a cognitive deficit in a hippocampus-dependent water maze test (119). The reason for the observed cognitive deficiencies are unclear. Several possibilities are listed below: (a) Due to an increased excitability, ripple occurence may increase. This however would suggest an increased memory consolidation, inconsistent with the poorer performance in the Morris Water Maze; (b) K_v7/M-currents contribute to theta range resonance. Blocking of these channels leads to decreases of theta and gamma oscillatory amplitudes in slices. As these are a prominent LFP feature during spatial navigation, it might be that spatial navigation itself is impaired. (c) In the hippocampus, REM sleep also shows similar theta and gamma oscillatory patterns. As REM sleep has a role for proper memory function, disruption of the network might be involved in an impaired consolidation of novel experiences into long-term memory. (d) During SW-R, pyramidal cells are strongly excited which may be dampened by the K_v7/M-current due to its role in spike frequency adaptation. By removing this dampening, SW-Rs may be disturbed and consolidation of experiences into memory may be further impaired. (e) Retrieval of memory during recall trials may be impaired, due to similar deficiencies as expected during spatial navigation. Of course, the actual answer may be any combination of these. It is therefore highly interesting to correlate hippocampal network patterns to behavioral paradigms in these K_v7/M-current-deficient mice.

These deliberations lead to the following hypotheses: [1] K_v7/M-current-deficient mice used for this study survived and did not show evidence of marked behavioral changes in their home cage. It is, therefore, hypothesized that typical patterns of hippocampal oscillations seen in controls are also seen in mutants. [2] K_v7/M-current deficiency throughout adulthood should result in reduced theta and gamma power during theta-associated behaviors such as running and REM sleep. [3] No literature was found on the contribution of K_v7/M-currents on either sharp waves or ripples, but due to the expected hyperexcitability, the occurrence of ripples might increase and [4] ripple shape may be altered. It is therefore unclear how K_v7/M-currents deficiency affects ripples. [5] Unit firing rates are expected to be increased due to the higher excitability and [6] their phase locking to the theta rhythm is expected to be decreased, due to the abolished K_v7/M-current resonance.

Methods

2.1 Animal model

Mice, used for this thesis, were generated previously (133). Under the control of the prion protein promoter (179), a tetracycline sensitive transactivator (tTA; Tet-off system, (65)) drives the expression of a *hKCNQ2* pore mutant construct with known dominant-negative properties (hQ2-G279S) (151), fused to a tetracycline-responsive element (TRE) (65). All C57BL/6 mice used were positive for tTa. Mice carrying the dominant-negative transgene are labeled mutants. Mice not carrying the dominant-negative transgene are labeled as controls.

All mice were bred and housed under a reversed day-night cycle at 23° C and 50% relative humidity. Food (ssniff Spezialdiäten GmbH) and water was given ad libitum. To prevent transgene expression during the initial neonatal period, doxycycline was mixed into the food pellets at 200mg/kg for weaning dams until pup-parent separation around P21.

2.2 Electrode implantation

Male mice (>5 weeks old) were anesthetized by 4% isoflurane in humidified 100% oxygen and kept at 1-2 % isoflurane throughout the operation. Mice were injected with 0.05 mg/kg buprenorphine (Temgesic), 7.5 mg/kg Enrofloxacin (Baytril) and 5 mg/kg Carprofen (Rimadyl), and placed in a stereotaxic apparatus (Stoelting). Body temperature was maintained at 36.5°C using a homeothermic heating pad and rectal thermometer (WPI). A midline skin incision was made on the top of the skull. 10% H_2O_2 was applied to the skull to remove residual tissue. A single-component self-etching dental adhesive (OptiBond) was applied to the skull surface and allowed to harden for 20 sec by UV-illumination (Woodpecker). Two stainless steel screws (SmallParts) - implanted at 1.0 mm anterior to bregma/1.0 mm lateral to the midline and 1.5mm posterior to lambda/1.0 mm lateral to the midline - were used for ground and reference electrodes, respectively. A single hippocampal silicon probe was implanted at 2.0 mm posterior to bregma/1.5 mm right to the midline, in a 0.8 mm wide burr hole. The probes used include a linear 16-site silicon probe with an interelectrode distance of 100 μm, and a 12-site 3-shank silicon probe with an interelectrode distance of 25 μm. All electrode surfaces were 177 μm^2 (NeuroNexus Technologies). The 3-shank probes were mounted on a custom-built drive prior to implantation. The 16-site linear probes were inserted vertically into the dorsal hippocampus (2.2 mm deep) along the CA1–dentate gyrus axis. The 3-shank probes were initially implanted 1.2 mm deep and slowly lowered post-op. Probes and drives were attached to the skull by a wooden framework and dental cement (Caulk Dentsply). The probe's reference wire was soldered to the wire pre-attached to the respective screw. Paraffin (Merck) was mixed with mineral oil (Sigma) and used to seal the hippocampal burr hole. A thin copper mesh was wrapped around the implant, to which both the ground wire from the probe as well as the respective screw were soldered. Skin was sutured together (Ethicon) and attached to the copper mesh with a tissue adhesive (3M VetBond). Mice were allowed to recover for at least three days, and were monitored closely during this time.

2.3 Data acquisition

2x or 20x amplifying headstages (Plexon) were attached to the probe and connected by a home-made cable to the recording setup (Neuralynx). Data were digitally filtered (0.5–9000 Hz band-pass) and digitized as 16-bit integers with a sampling rate of 32552 Hz using a Digital Lynx 4SX data acquisition system (Neuralynx). A 25 Hz color camera simultaneously recorded positional data from a red and a green LED that were attached to the headstage. Video threshold detection was performed online and saved to disk. LFPs were downsampled to 1252 Hz from raw traces. All *in-vivo* data were analyzed and visualized in MATLAB (MathWorks) or NeuroScope (73). Using a Minirator MR1 (NTI) to apply a 20 Hz 0.5mV root-mean-squared sinusodal test signal to the headstage, the signal was calibrated. Amplifications were set such that the measured signal in Neuroscope had the same peak-to-peak amplitudes as when the Minirator signal was used as an input on an oscillator (TDS2014, Tektronics).

2.4 Behavioral paradigms

On each day where mice were exposed to behavioral paradigms, home cage rest was recorded for at least 1.5 hrs both before and afterwards. Each individual open field, new objects, moved object, and single trial spatial memory (STSM) session lasted 30 minutes. Breaks in between sessions lasted 10 minutes, with mice in their home cage, unless otherwise mentioned. In between each session, mazes were cleaned with 70% ethanol. The mice were exposed to these behavioral paradigms in the order listed below. Mice were given 1-2 days between behavioral paradigms to recover.

2.4.1 Open Field and spatial novelty

On day 1, mice were allowed to explore an asymmetric circular open field (Figure 7, left) twice. On day 2, mice were re-exposed to the open field once. Afterwards, two different objects X and Y were placed inside the open field (Figure 7, middle). Mice were now allowed to explore this open field twice. On day 3, they were re-exposed to the open field once with the same object configuration as on day 2. Then, they were allowed to explore the open field twice after object X was moved to the contralateral side (Figure 7, right). Interest in an object was defined as the time spent within 5 cm distance of that object. The relative interest for object X is defined as the interest ratio X/Y. Spatial memory was assessed by the change of the relative interest for object X between the first and second sessions on day 3.

On day 1, mice were allowed to explore an assymetric circular open field (Figure 7, left) twice. On day 2, mice were reexposed to the open field once. Then, they were allowed to explore the open field twice in which two different objects X and Y were placed (Figure 7, middle). On day 3, they were reexposed to the open field once with the same object configuration as on day 2. Then, they were allowed to explore the open field twice, where object X was moved to the controlateral side (Figure 7, right). Interest in an object was defined as the time spent within 5 cm distance of that object. The relative interest for object X is defined as the interest ratio X/Y. Spatial memory was assessed by the change of the relative interest for object X between the first and second session on day 3.

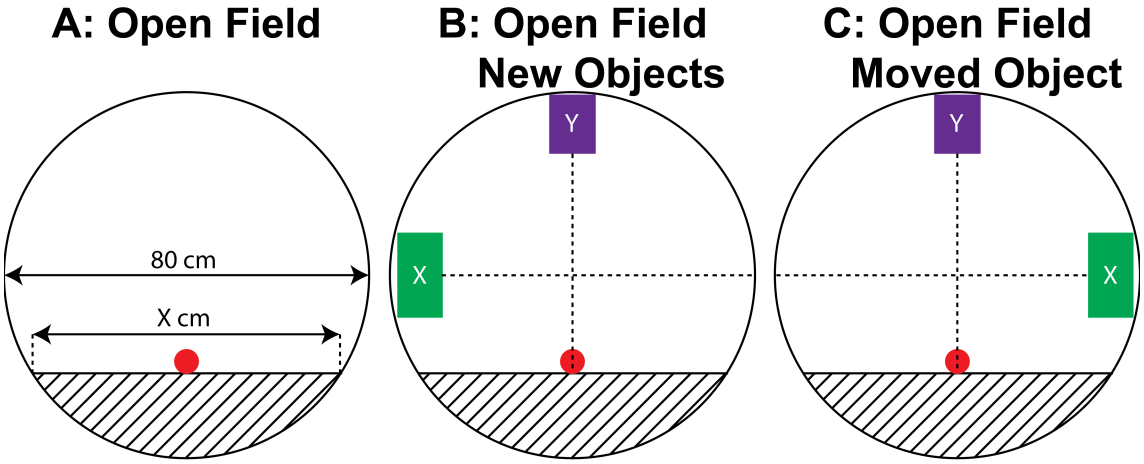

Figure 7: Open fields and spatial novelty mazes. **A:** A semi-circular open field, where a wall was added to create asymmetry. The red dot indicates the mouse's entry point. **B:** Mice were subsequently exposed to two different objects, placed against the wall of the open field opposing and to the left of the asymmetric side, respectively. **C:** Eventually, object X was moved to the contralateral side. The change in relative interest for object X was used as a measure for spatial memory.

2.4.2 Single trial spatial memory (STSM)

The STSM (51) consisted of a 80cm x 80cm square open field with three corners made inaccessible by 10 x 10 cm walls (Figure 8A). On day 1, male mice were exposed once to the field, while one of the three inaccessible corners contained 4-5 females. Holes near the bottom of each walled-off corner allowed the male mouse to smell, but not touch, the female mice. Afterwards, the male mouse was left to rest for 75 minutes in its home cage, during which the STSM maze was replaced with an identical "clean" version to completely prevent any residual scents from interfering with a purely spatial paradigm.

Mice were then tested for their spatial memory while they re-explored this female-free STSM open field. Interest in a corner was defined as the time spent within a 5 cm distance of that corner. Spatial memory is assessed by the relative interest the male mouse has in the female corner. After this short-term recall, mice are re-exposed to females in the "dirty" maze twice to further consolidate the female's position and to oppose possible memory extinction due to short-term recall. On day 2, mice were allowed to explore the female-free "clean" STSM maze twice for long-term recall.

2.4.3 Y-maze

On a single day, mice were tested twice in a Y-maze (Figure 8B) until within a single session they either made 46 transitions - exiting one arm and entering another- or spent 20 minutes in the maze. As mice tend to be exploratory creatures, they slightly prefer to visit the arm that had not recently visited. A correct transition occurs when the mouse visits an arm it had not been in prior to the previous transition. For each mouse, the performance from two Y-maze sessions were averaged. The number of correct transitions to total number of transitions (50% being chance level) was used as a measure to asses the working memory.

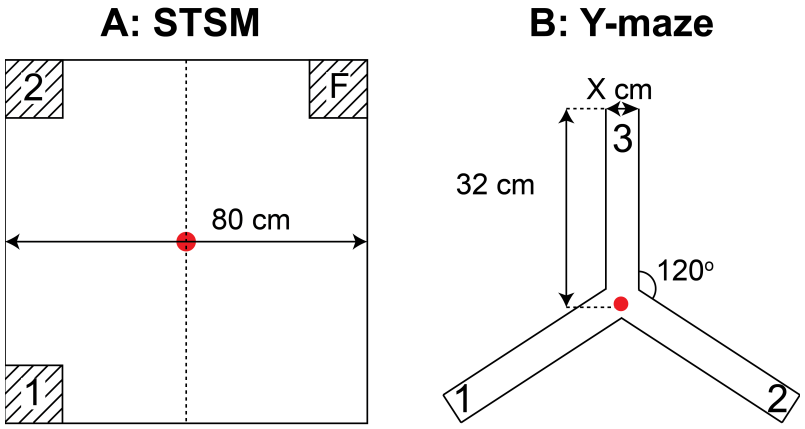

Figure 8: The STSM open field and Y-maze investigate spatial navigation and memory. **A:** In a STSM open field, three corners are barred by plastic walls with holes at the bottom. One of three corners, marked "F", contains 4-5 females. After exposure to females, male mice are retested in the STSM open field without females to observe their preferences for either corner. The red dot indicates the mouse's entry point. **B:** In a Y-maze, three equally spaced arms are used to assess the mouse's working memory. A correct transition was defined when the mouse visited an arm it had not been in prior to the previous transition. The red dot indicates the mouse's entry point.

2.5 Data analysis

The 32552 Hz broadband raw signal was downsampled to 1252 Hz to speed up analysis. CSDs were calculated by applying the inverse of the electrostatic forward solution (137). This procedure calculates how currents would be volume conducted through the brain, assuming an extracellular conductivity of 0.3 S/m (69) and a source diameter of 0.5 mm. This is then applied to the measured LFP to estimate local currents, basically by calculating the answer to the question "What currents would have been necessary to create the recorded LFP, based on the volume conduction of the surrounding tissue?" These estimated currents are expressed in A/m^3. Multitaper spectrograms, power spectra and coherences were computed using Chronux (www.chronux.org; nFFT 4096 points, sliding window 2048 points).

2.5.1 Ripples

During home cage sleep sessions, ripples were semi-automatically detected. From the spectrogram, a period (>100 sec) characterized by both immobility and increased occurrences of ripples representing power spikes within 100-250 Hz was selected as a representative SWS-epoch. First, the instantaneous ripple amplitude from this epoch was calculated by the absolute of the Hilbert transform on a ripple band filtered signal (Butterworth; 14th order, 100–250 Hz) from which the mean and standard deviations (SD) were extracted. Second, throughout the entire recording, ripples were defined as periods during which the peak instantaneous amplitude exceeded four times the SD above the mean. The borders on the left and right side of this peak were defined as the time points where the instantaneous power dropped below 1.75 SD above the mean. Events shorter than 25 ms and those during non-SWS periods were excluded. These non-SWS periods included epochs [1] of continued 4-12 and 30-100 Hz oscillations without movement (paradoxical/REM sleep); [2] where low occurrence of ripples was quickly alternated with movement and 4-12 and 30-100 Hz bouts (awake behavior); and, [3] periods of high frequency non-oscillatory noise on all channels simultaneously (EMG-noise). Events whose borders were separated by 8 ms or less were combined

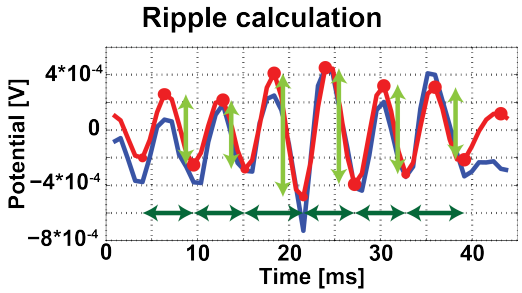

Figure 9: Calculation of ripple properties. The raw trace from str. Pyr (blue) is filtered in ripple range (red). The minima and maxima are then detected (red dots). The average time between subsequent troughs (dark green arrows) is used to estimate its frequency. The average of the peak-to-peak potential differences (light green arrows) is used to calculated its amplitude.

as one event.

For detected ripples, several parameters were calculated (Figure 9). For each individual ripple, the average peak-to-peak amplitude on the bandpass-filtered signal was calculated. Ripple frequency was estimated by calculating the mean inverse distance between subsequent troughs. To obtain the ripple amplitude and frequency per session, a mean was calculated for all detected ripples throughout a recording. Ripple occurrence was defined as the number of ripples per second of SWS brain state.

Retrograde inspection was used to verify that the channel with the largest ripple amplitude was used for ripple detection. This channel was then defined as str. Pyr. From the CSD-profile for linear probes, the minimum and maximum during each ripple was detected on the wide-band signal. The median of these minima and maxima was calculated for all channels. The most negative minimum during ripples 100-300 μm below str. Pyr was defined as the sharp wave amplitude and the channel on which this occurred was defined as str. Rad. During ripples, the sharp wave creates a return current in both str. Pyr and str. LM. The channel that showed the largest return current 100-300 μm below str. Rad was defined as str. LM. Layer identification during behavioral trials were based on each individual pre-task sleep session, adjusting for possible probe shifts.

Ripple detection performance was estimated by identifying ripples from the CSD by eye on a 5 min period of SWS and counting the correct, false positive and false negative detected events.

2.5.2 Theta/gamma epochs

Paradoxical/REM-like epochs during sleep were manually selected from the LFP and characterized by the presence of theta (4–12 Hz) and gamma (30–100 Hz) oscillations during immobility. Epoch selection occurred mostly on spectrograms from the putative str. Pyr. During open field/spatial novelty and STSM, running epochs were automatically detected by extracting those where the mouse continuously ran at least 10 cm/s for at least 1 sec long. Detected running epochs were manually corrected for recording artifacts. Phase and instantaneous amplitude of the signal were calculated by the angle and the absolute value, respectively, of the Hilbert transform on a band filtered signal (Butterworth; 3rd order for 4–12 Hz, 6th order for 30-100 Hz).

All theta and gamma properties mentioned below were calculated for both the LFP and CSD. For each session, average theta and gamma powers were calculated for all epochs by integrating the area below the theta and gamma ranges in the power spectra. Any possible power cycle peaks were removed from the power spectrum by linearly interpolating between 48.5 - 51.5 Hz. Theta and gamma peak frequency was achieved by finding the maximum power peak with the respective frequency ranges after whitening the spectrum in order to get rid of the $1/f^n$ power law.

Modulation of gamma power by theta phase was calculated by first binning theta phase in 18 blocks of 20 degrees each. The mean instantaneous gamma amplitude within each theta phase

block was calculated and normalized according to

$$\gamma_{amp,\ norm}(i) = \frac{\gamma_{amp}(i)}{\sum_{i=1}^{N} \gamma_{amp}(i)} \tag{2.5.1}$$

where N denotes the number of bins and i denotes the i-th bin. The modulation index (MI) for the modulation of gamma amplitude by theta phase was then calculated by comparing $\gamma_{amp,\ norm}(i)$ to a uniform distribution, using an adaptation of the Kullback–Leibler divergence (175), according to

$$MI = \frac{1}{N} \sum_{i=1}^{N} \gamma_{amp,norm}(i) \log \frac{\gamma_{amp,norm}(i)}{1/N} \tag{2.5.2}$$

Dividing the sum by the number of bins scales the MI between 0 (no modulation) and 1 (perfect modulation).

Theta wave asymmetry was determined as follows. First, minima and maxima were detected on the 4-12 Hz filtered signal. Between two subsequent maxima from the 4-12 Hz signal, a minimum was detected for a 1-50 Hz signal (Butterworth; third order). Concordantly, between two subsequent minima from the 4-12 Hz signal, a maximum was detected for a 1-50 Hz signal. The median distance (in seconds) between a detected 1-50 Hz minimum and the following 1-50 Hz maximum was divided by the median distance between a detected 1-50 Hz maximum and the following 1-50 Hz minimum. If this ratio is > 1, then the descending phase is longer than the ascending phase, and vice versa.

For running epochs, speed modulation of theta and gamma amplitude was calculated by applying a linear fit to a matrix where theta or gamma amplitude (the absolute value of Hilbert transform, as mentioned before) at each time point was paired with the corresponding speed. A value of 5% means that the amplitude of the linear fit at 30 cm/s changed with a factor of 1.05 compared to the amplitude at 10 cm/s.

For theta/gamma epochs depth profiles, recordings were aligned such so that every recording had exactly one channel between str. Pyr and str. Rad and between str. Rad and str. LM. Exceptions to this were aligned according to Figure 10. Please note that averaging channels during alignment is not the same as the calculation of an average CSD-trace from which the relevant parameters were extracted. Instead, all parameters were extracted from the original CSD-traces and, if realignment required it, subsequently averaged.

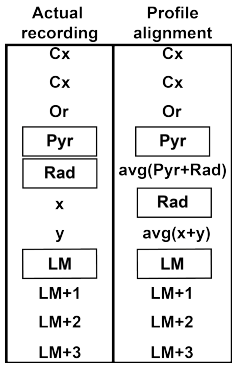

Figure 10: Alignment of depth profiles. Most recordings have one channel both in between str. Pyr and str. Rad and between str. Rad and str. LM. If a recording does not show a channel in between these regions – like for example if str. Pyr and str. Rad's were anatomically adjacent – the intermittent channel was averaged between the two. If two channels were recorded in between either aformentioned pair (for the example between str. Rad and str. LM), the intermittent channel was averaged from both two channels.

2.5.3 Neural firing

Since the waveform of the spike is dependent on the position and orientation of the neuron relative to the electrode and is similar to other spikes coming from the same neuron, it can be used to identify single units from spiking data. In order to do this, the broadband signal was high-pass filtered (Butterworth; 11^{th} order, 800 Hz cutoff). Any spikes that exceeded the mean by 4 standard deviations were recorded. Three principal components were calculated from the spike waveform for each of the channels of the shank on which the spike occurred. Clustering was then performed with KlustaKwik software (71), using the principal components for each detected spike to determine whether they are likely to belong to the same neuron. Clean units were defined as those where the number of spikes within 2ms (the refractory period) was lower than 1% and the height of the center autocorrelation bars were lower than the average firing rate, depicted by the calculated assymptote for $\delta \to \infty$. This clustering procedure overclustered, so manual correction using Klusters was necessary (73). Clean clusters were merged if waveshapes were similar and if the firing cross-correlation between them showed a clear refractory period.

Neural phase locking to either theta oscillations during REM sleep or to ripples during SWS was determined by calculating the oscillatory phase (angle of Hilbert transform) for each spike and subsequently calculating the circular concentration coefficient (ccc) in a Rayleigh test for the appropriate epoch. Units with less than 150 spikes during REM and ripples were excluded. Since the calculation of the ccc is biased by the number of spikes that are used, 150 spikes were randomly selected from the ones available and calculated for their ccc. The random selection and subsequent calculation of the ccc was repeated 1000 times ('bootstrapping'), after which the mean was taken as the representative ccc for the analyzed unit.

2.6 Further Y-maze analysis

Running in the Y-maze, in contrast to in open fields or STSM, is highly similar throughout the paradigm. Mice do not have the opportunity to use external landmarks to identify which of the three arms they are currently visiting, and freedom of movement is restricted due to narrow Y-maze arms. Each run towards the center may therefore be seen as similar.

Electrophysiological data from Y-maze runs was collected as follows (Figure 11): each run toward the center that started at least 50% of an arm distance away from the center and resulted in a clear and direct decision for a new arm was marked. In MATLAB, the center and each arm of the Y-maze was identified from the running path throughout the entire recording. The x- and y-coordinates were then rotated such that each new x-axis was parallel to an arm. All distances to the center were then normalized to the longest detected run of the respective session and binned into 6 equidistant bins. A linear fit was applied to the mean gamma amplitude for each bin, the resulting slope normalized by the offset, and this was repeated for each layer. Coherences between str. Pyr and str. Rad as well as between str. Pyr and str. LM were calculated for the starting, middle, and final third of each run.

2.7 Statistics

The following statistics were performed using Prism5 and Statistica: [1] the 2-tailed Mann-Whitney test for the differences of one variable, which does not presuppose a normal distribution of the data;

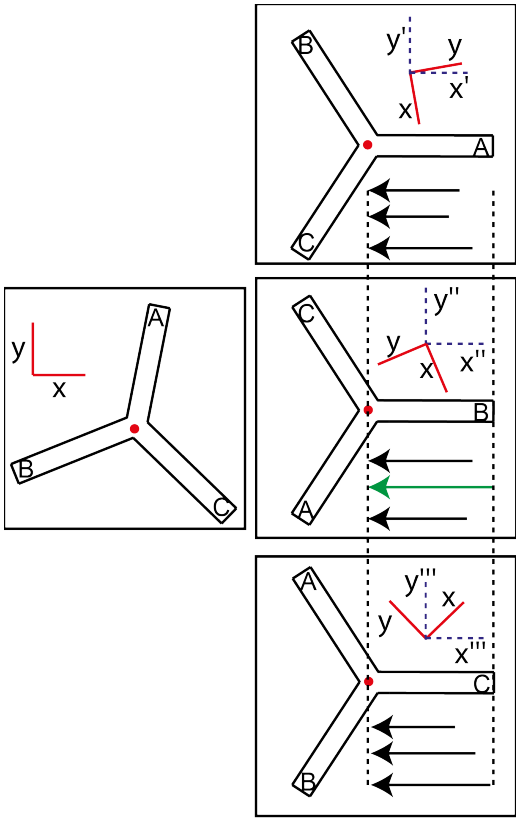

Figure 11: X- and y-coordinates from the original recording (red lines) were rotated into [x' , y'], [x" , y"] and [x"' , y"']] (dashed blue lines), such that each recalculated x-axis was parallel to arm A, B, and C, respectively. Distance to the center was then normalized to the start of the run that started from the point located furthest away (green arrow).

[2] the Wilcoxon signed rank test to determine whether a groups median is significantly different from a hypothetical value; [3] a repeated measures ANOVA with a post-hoc Newman-Keuls (when interaction between two variables was significant). Each data point is shown as the mean, and error bars represent the standard error of the mean. Significant difference is denoted by *: $p<0.05$ (significant), **: $p<0.01$ (very significant), or ***: $p<0.001$ (highly significant).

The repeated measures ANOVA test with a post-hoc Newman-Keuls is only applied to depth profiles where a parameter, e.g. theta power, is calculated along all anatomical layers for both wild type and M-current deficient mice. However, this test is not perfectly applicable, since each parameter measurement is done in a different layer, and so, theoretically, is not repeated. Nevertheless, layers are anatomically connected and influence each other, and, therefore, the measurements are not completely independent from each other either. An additional problem with the post-hoc test for repeated measures is that it assumes a similar variance between comparisons, and since it has already been shown that theta oscillations in str. LM are the higher than in other layers, the variance in str. LM will also be higher, and as such, dominate any post-hoc test. These results are therefore shown where applicable, but their outcome may not be a representative result of the dataset.

Results

In this thesis, the effect of a reduction in K_v7/M-currents in adult mice was investigated. The mutant mouse model expressed, via a Tet-off system, a dominant-negative $K_v7.2$ subunit under the prion protein promoter. Incorporation of this subunit into a tetrameric K_v7/M-channel renders this channel non-functional. Prevention of expression during the first weeks of life by addition of doxycycline to the animals' chow previously showed prevention of morphological abnormalities, epileptic seizures, and behavioral hyperactivity (133). These mice, hereafter referred to as mutants, were tested against a littermate control group: mice that only expressed the tTa-element under the prion protein promoter and received doxycycline during the same period, but did not express the dominant-negative $K_v7.2$ subunit. Differences between controls and mutants in hippocampal CA1 LFP recordings were obtained during basic sleep (see Chapter 3.1), spatial navigation in an STSM test (see Chapter 3.2), Y-Maze (see Chapter 3.4), and a spatial novelty task (see Chapter 3.5).

3.1 Basic sleep

During handling, mutant and control mice showed no apparent behavioral phenotype, nor did they exhibit differences in their response to isoflurane anesthesia or their recovery after surgery. The implantation sites were histologically verified post mortem (Figure 12). After five to seven days of recovery, the home cage recordings allowed mice to get used to the implanted silicon probe being connected by a cable. Qualitatively, home cage recordings looked similar between controls and mutants (see Chapter 3.1.1), but showed quantitative differences.

3.1.1 Sleep from home cage recordings progresses similarly between controls and mutants

As a result of analyzing electrophysiological recordings during home cage sessions prior to any behavioral activity, this chapter demonstrates that basic neural networks that are active during paradoxical and SWS are present in K_v7/M-current-deficient mice.

After recording a home cage session, depth profiles of the LFPs were investigated in order to see whether typical oscillatory patterns seen in WT mice with basic network activity were present in K_v7/M-current-deficient mice. In general, control and mutant mice showed qualitatively similar network activity. From the channel located closest to str. Pyr, as determined by the

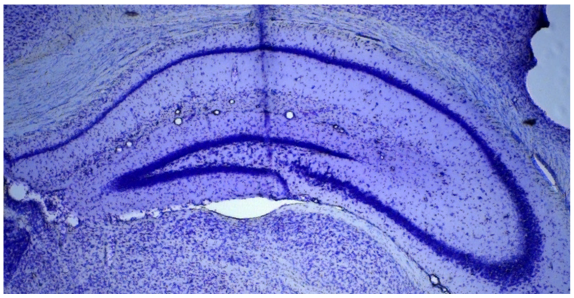

Figure 12: Histological verification of probe insertion coordinates. A Nissl stain of the dorsal hippocampus, showing a trace of the insertion path of an implanted probe.

occurrence of short (± 50 ms) high-frequency (±150 Hz) ripples, spectrograms were calculated from the downsampled LFP signals. In Figure 13A, several electrophysiologically different epochs can be observed: SWS is characterized by immobility and the occurrence of high-frequency ripples; paradoxical sleep is characterized by immobility and continuous theta and waxing and waning gamma oscillations; awake behavior is characterized by intermittent bursts of theta and gamma oscillations during movement, sparse ripples during immobility, and high-frequency EMG noise, the latter appearing simultaneously on all channels.

The duration of sleep spent in a SWS state was longer than that spent in paradoxical sleep, both in mutants and controls. As the duration ratio of paradoxical sleep/SWS varied strongly, even within multiple recordings of individual mice, no differences could be identified. Ripples also occurred during awake behavior, but their occurrence was far lower than during SWS.

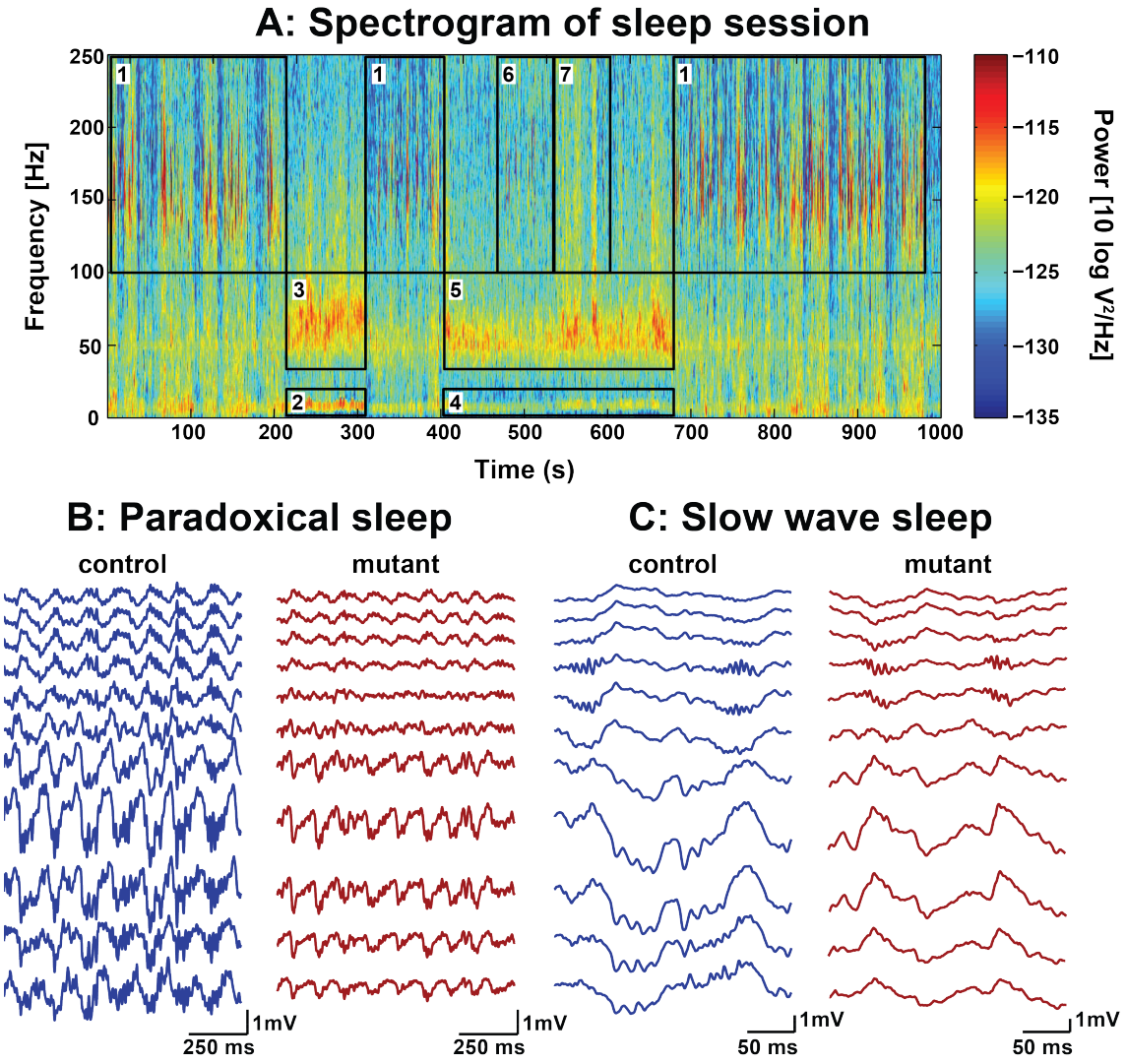

Figure 13: Data obtained from exemplary home cage sessions. **A:** Whitened time-frequency spectrogram of color-coded LFP power during a home cage epoch. Several SWS epochs with a high incidence of high-frequency ripples are visible (Boxes labeled 1), paradoxical sleep with increased theta (Box 2), and gamma (Box 3) frequencies, awake activity with sporadic bursts in theta (Box 4), gamma (Box 5), and ripple frequency ranges (Box 6), and occasional EMG noise (Box 7). Paradoxical sleep states are discerned from awake behavior by verifying the absence of movement. **B:** Exemplary raw data traces showing paradoxical sleep states. **C:** Exemplary raw data traces showing SWS sleep with ripples in str. Pyr.

With all home-cage recordings, sleep after a period of awake behavior is characterized by the occurrence of SWS. Furthermore, as can be seen from Figure 13A, there were short intermittent periods during which no 150-Hz oscillations occurred, e.g. at around 180 s of the excerpt/epoch shown. These periods did not conform to any of the three non-SWS epochs mentioned in Chapter 2.5.1. As they were still regarded as periods during which ripples could have occurred, their occurrence was calculated for the entire duration of the boxes labeled 1 in Figure 13.

Ripple detection performance in a control mouse showed that about 3.4% of the ripples detected were false negatives, indicating that practically all detected events can be classified as SW-ripple complexes. Visually, ripples were more easily identified from the CSD by the high frequency ripple oscillation in str. Pyr together with the occurrence of sharp waves in str. Rad, whereas the algorithm used was based solely on ripple amplitudes in the LFP. Smaller amplitude ripples were therefore not considered by the algorithm, which resulted in a false-negative detection of 23.8%. Of note, the relatively long time spent in SWS epochs and the regular occurrence of SW ripples throughout the epochs made the collection of a large number of events (100-3000) possible, despite the definition used (see Chapter 2.5.1)

Paradoxical sleep starts off slowly from SWS and takes a few seconds to form clear continuous theta oscillations. Throughout a paradoxical sleep phase, amplitude and frequency of both the theta and gamma bands fluctuate, but a temporal trend was not observed. The end of such a phase is a rather clear-cut ablation of oscillatory activity within 100 ms. Within a few seconds after the abrupt end of paradoxical sleep, EMG noise can often be observed, and is accompanied by either complete awakening of the mouse or a return to SWS. In cases in which paradoxical sleep epochs were difficult to determine due to small LFP amplitudes, the putative layer for str. LM, where theta oscillation amplitudes are higher, was additionally used to visualize the emergent theta and gamma bands.

Not every home cage session contained a paradoxical sleep epoch. First, this is a matter of chance because the duration of sleep during a home cage session varied strongly from one recording to the next. Second, not every period of sleep contained a paradoxical sleep epoch because these phases tend to occur irregularly. Third, after a behavioral task, paradoxical sleep occurred more towards the end of the recording, favoring SWS epochs at the beginning, which further reduced the chance of recording paradoxical sleep during post-task sleep.

3.1.2 Slow wave sleep epochs reveal altered ripple and sharp wave amplitudes

SW-R complexes are important for a proper consolidation of memory (see Chapter 1.4.4), and any alteration in them may contribute to memory deficits, which has already been shown in water maze experiments (133). From raw traces (Figure 13C), it was observed that ripples did occur in the mutant. However, the analysis presented in this chapter revealed quantitative differences between controls and K_v7/M-current-deficient mutants.

The parameters of ripples that were investigated were their amplitude, as calculated by the peak-to-peak voltage, their frequency, as calculated from the time between subsequent ripple troughs, and their occurrence, by dividing the total number of detected ripples by the total time determined to be SWS (see Chapter 2.5.1). Peak-to-peak voltages for ripples were used to confirm post-hoc that the selected channel for ripple detection, and hence the channel defined as being closest to str. Pyr, indeed had the highest amplitudes compared to anatomically adjacent chan-

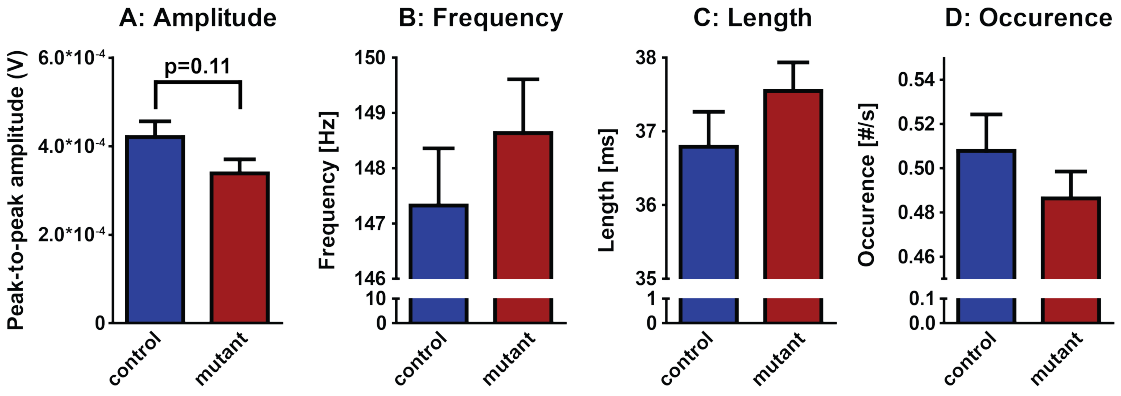

Figure 14: Ripples that occur during SWS in controls differ from those detected in mutants. **A:** Peak-to- peak amplitude calculation of detected ripples reveal that K_v7/M-current-deficient mice tend to have reduced amplitude when compared to control littermates. **B-D:** Frequency, length, and occurrence of ripples are similar between controls and mutants (p=0.32, p=0.15, p=0.30, respectively).

nels. A comparison of parameters between control and mutant mice (Figure 14) showed similar frequencies, lengths, and occurrences, but mutants tended to have smaller ripples: peak-to-peak voltages for controls show an average of 4.2 * 10^{-4} V, compared to 3.4 * 10^{-4} V for mutants, p=0.11.

The tendency for reduced ripple amplitudes can be due to a decreased excitatory input from CA3 into CA1. This can be further investigated by calculating the CSD. A CSD is used to assess the currents that are passing into and out of a separate layer along the vertically inserted electrode's axis, here calculated by using the inversion of the electrostatic forward solution (see Chapter 2.5), and to improve identification of the anatomically distinct layers (see Figure 15). The current sink in str. Rad from excitatory CA3 activity, the driving force behind the emergence of a high frequency ripples in CA1 str. Pyr, is clearly visible two channels below str. Pyr. This channel indicates the recording of the largest cumulative EPSCs during a ripple. Therefore, it is assumed to be located closest to the dendritic section, where Schaffer collaterals terminate onto CA1, and hence represents str. Rad. The return current can also be seen as sources in str. Pyr and two channels below str. Rad. The channel with the largest source below str. Rad is defined as str. LM. In agreement with the tendency towards smaller amplitude ripples in mutants (Figure 14), sharp-wave amplitudes were significantly reduced from 4.4 *10^4 to 3.0*10^4 A/m^3, p<0.05.

Together, K_v7/M-current-deficient mice showed reduced ripple amplitudes, possibly due to a reduced excitatory drive from CA3. This may contribute to a reduced memory performance.

3.1.3 Paradoxical sleep in mutants show decreased theta and gamma power and modulation index

As proper paradoxical sleep influences memory performance (see Chapter 1.4.4), the electrophysiological properties were investigated.

Fourier analysis of two exemplary paradoxical sleep traces showed the typical $1/f^n$ power law, where amplitude generally decreases with increasing frequency. Paradoxical sleep epochs showed distinct activity within the theta and gamma frequency bands (Figure 16A). For some recordings, an additional peak occurred at a frequency two times the frequency of the theta peak. Fourier analysis sometimes generated second harmonics, but the specific properties of this second harmonic were not investigated. Since the $1/f^n$ power law caused the gamma band activity to show a change in slope, rather than a peak, it could not be used to estimate the peak frequency of the gamma

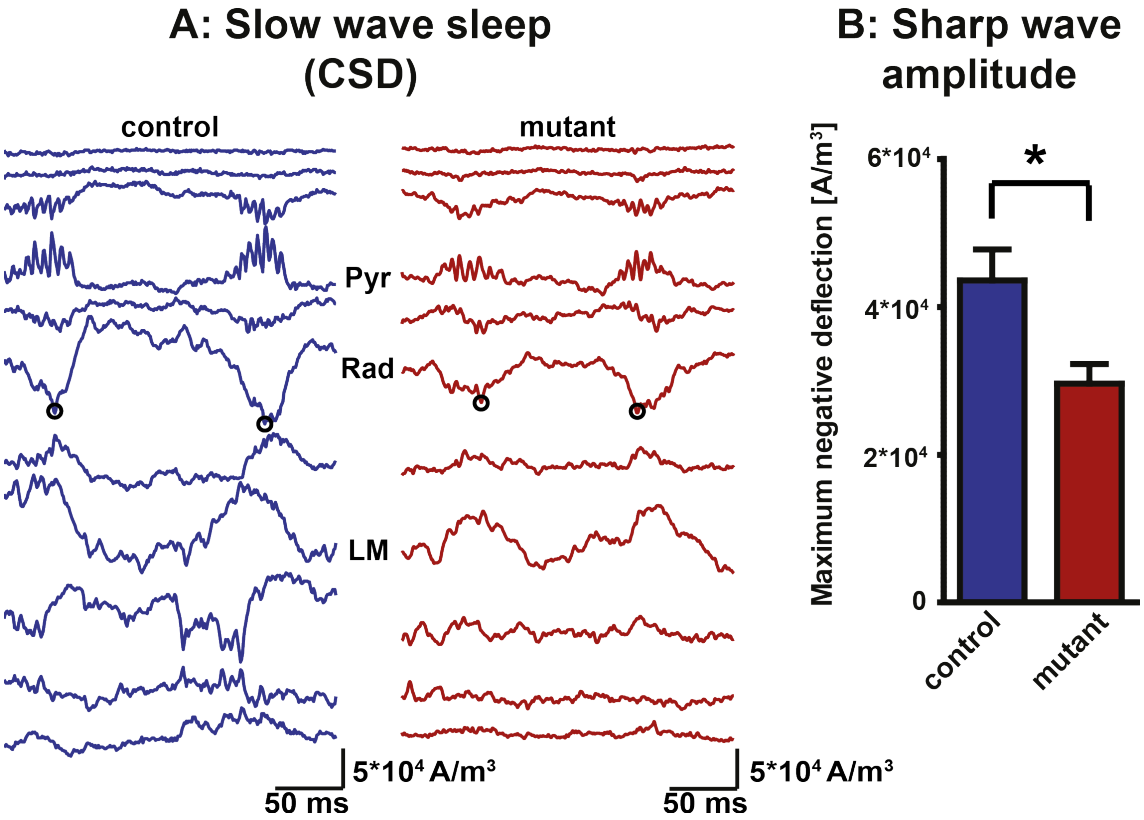

Figure 15: Examplary CSDs during SWS. **A:** The same examples as shown in Figure 13 are shown here after calculating their CSDs. Both CSD profiles show high frequency ripples in str. Pyr. The channel with the largest co-ocuring sink, depicted by the black circles, is defined as str. Rad, while the channel with the largest source below str. Rad was labelled str. LM. **B:** The maximum negative deflection during the detected ripples in str. Rad, i.e. sharp waves, are significantly smaller for mutants, compared to controls.

band. Whitening the signal (Figure 16B) resulted in a clear peak for the gamma band. However, the whitening procedure was based on a fit that was dependent on the signal's content, i.e. changes in one frequency band can affect the shape of other bands after whitening. Therefore, whitening was only used for peak detection, whereas integrated powers were calculated from the unwhitened spectra. In both Figure 16A and B, the linear interpolation between 49 and 51 Hz, which was performed to remove 50 Hz power cycle noise when present, can be seen in the power spectra by the short straight line. The gamma amplitude as a function of theta phase (Figure 16C) shows a flatter distribution for a mutant mouse compared to a control mouse.

Mutants showed a reduction in both theta power (Figure 17A, control: $1.0*10^{-8}$ V^2, mutant: $6.7*10^{-9}$ V^2 , $p<0.05$) and gamma power (Figure 17C, control: $2.2*10^{-9}$, mutant: $1.0*10^{-9}$, $p<0.01$), whereas the peak position in both bands (Figure 17B, D, respectively) remained the same. When the modulation indices are calculated for all animals (Figure 17E), a highly significant reduction of gamma modulation is seen in mutants (control: $1.4*10^{-2}$ mutants $7.8*10^{-3}$, $p<0.001$).

Theta wave asymmetry, which is caused by the dynamics of local synaptic currents (Figure 17F), provides a measure for the shape of the theta wave by the calculation of a ratio between the lengths of its ascending and descending portions. A comparison of theta wave asymmetry between both groups of mice did not reveal differences. As this ratio is less than one, it indicates that the ascending phase in str. Pyr was shorter than the descending phase.

In summary, K_v7/M-current deficiency leads to reduced LFP theta and gamma power in str.

Pyr. Additionally, a lower modulation index indicates that the coordination of the gamma rhythm with the theta rhythm is weaker. However, it remains unclear whether the reduced power values and the reduced modulation index are causally related. From a mathematical point of view, the modulation index is not dependent on the absolute power of either the theta or gamma band, but physiologically there may be a connection. Additionally, based solely on LFP recordings performed for this thesis, it is not possible to determine whether the power loss is due to a general reduction in activity or whether there is a reduced EPSC synchrony.

3.1.4 Depth profiles show layer-specific differences of hippocampal LFP properties during paradoxical sleep

In Figure 17, paradoxical sleep analysis shows the parameters only for the LFP and only for str. Pyr. Since the linear probe allows us to record across multiple lamina (22), it is important to investigate whether the transmembrane currents at the dendrites are disturbed, as was done for determining the sharp wave size for SW-R complexes in Figure 15.

The CSD depth profiles for theta and gamma powers, modulation index, and theta wave asymmetry during paradoxical sleep are shown in Figure 18. These profiles show that the reduction of theta and gamma powers (Figure 18A, B) are not limited to str. Pyr, but span the entire CA1 axis. The modulation index is also reduced in many layers. However, there does not seem to be a direct link between theta/gamma power loss and a reduction of the modulation index for individual layers, since in str. Pyr and between str. Pyr and str. Rad, where theta and gamma powers are clearly reduced, there is no change in the modulation index.

For theta power, a repeated mesures ANOVA reveals highly significant influence of interaction and layer ($p<0.001$) and significant influence of genotype ($p<0.05$). The post-hoc Newman-Keuls test, reveals highly significant differences for str. LM ($p<0.001$). Similarly, a repeated measures ANOVA analysis for gamma power reveals a very significant influence of genotype ($p<0.01$) and a highly significant influence of layer and interaction ($p<0.001$). A post-hoc Newman Keuls test however reveals no single layer to be significantly different.

A repeated measures ANOVA on the theta wave asymmetry depth profile (Figure 18C) reveals a highly significant influence of layer ($p<0.001$). This was to be expected due to the phase reversal, visible between the upper and lower CA1 layers (Figure 13B). Indeed, above the phase reversal, the

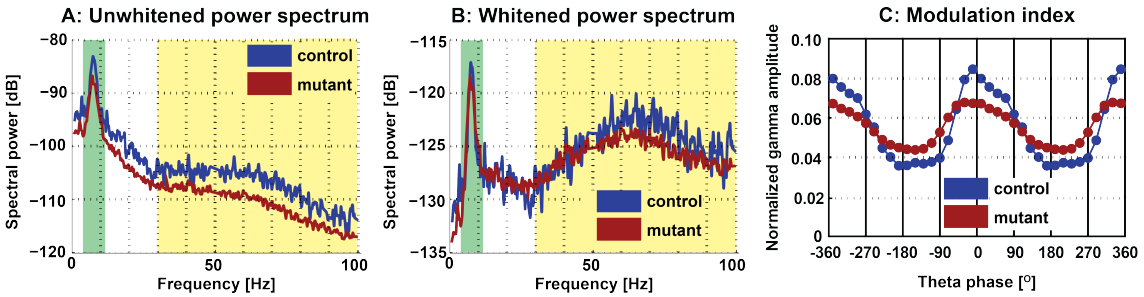

Figure 16: An exemplary power spectrum from paradoxical sleep showing two individual recordings from a control (blue) and mutant mouse (red). **A:** An unwhitened power spectrum shows activity in both the theta (4-12 Hz, green shading) and gamma frequency ranges (30-100 Hz, yellow shading). Due to the $1/f^n$ power law, the activity in the gamma band did not show a peak. **B:** After whitening the signal, the activity in the gamma band clearly showed a peak. **C:** The modulation of gamma amplitude by theta phase showed similar profiles in both mutant and controls, but modulation was weaker in mutants. The modulation index for the control example is $1.69*10^{-2}$, and $4.52*10^{-3}$ for the mutant example.

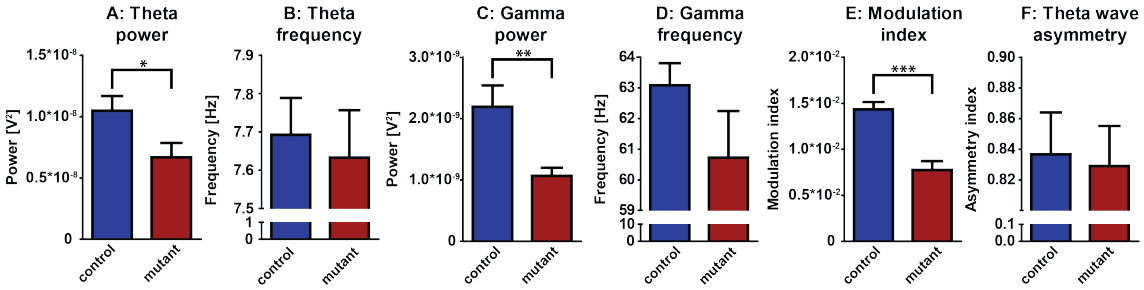

Figure 17: Paradoxical epoch LFP results from str. Pyr showing reduced theta (**A**) and gamma power (**C**) and modulation indices (**E**), whereas theta and gamma peak frequencies (**B**, **D**, respectively), as well as theta wave asymmetry (**F**), were similar in controls and mutants.

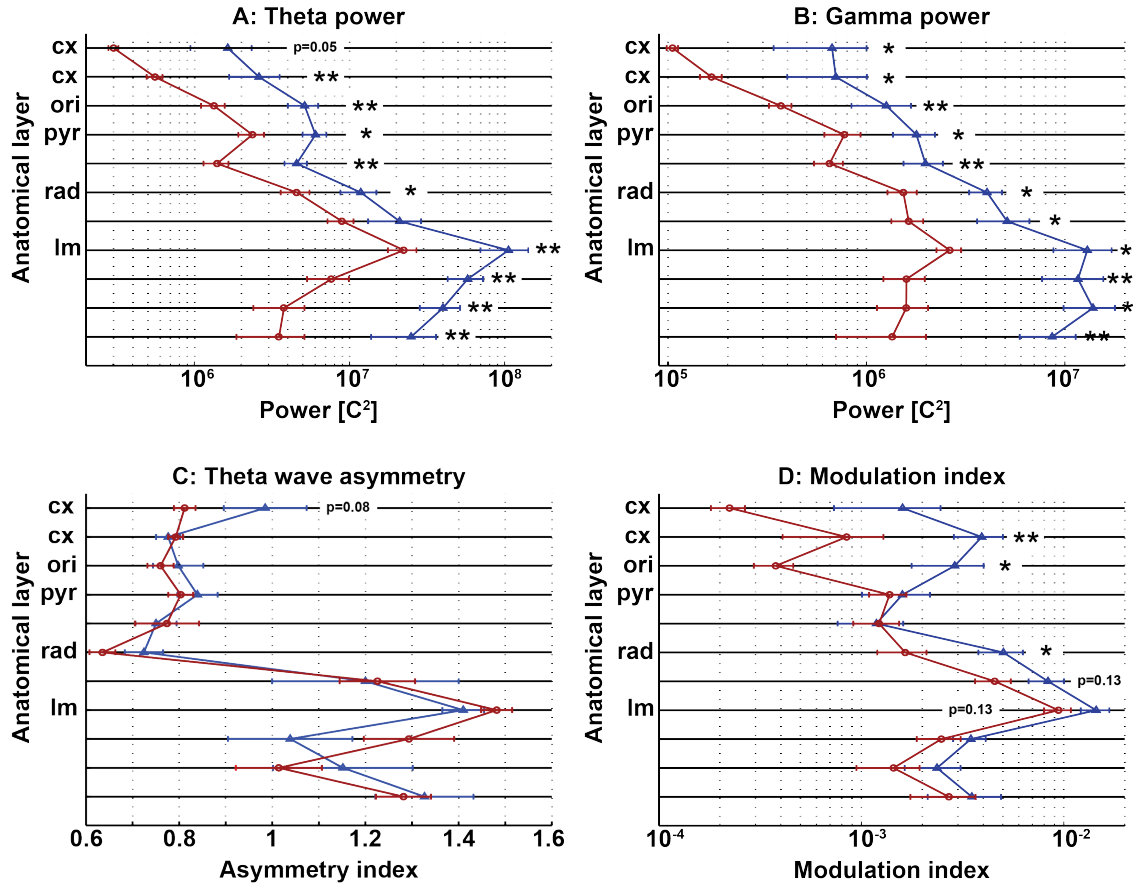

Figure 18: Depth profiles for paradoxical sleep CSD results. These depth profiles indicate a decrease of theta (**A**) and gamma powers (**B**) across almost all layers, according to Mann-Whitney tests. The symmetry of the theta wave (**C**) is similar for both groups and clearly shows the abrupt phase reversal between str. Rad and str LM. The modulation index (**D**) seems reduced for str. Ori, the deepest cortical layer, str. Rad and str. LM. Significance levels as analyzed using Mann-Whitney tests.

asymmetry index lies around 0.8 – below the phase reversal around 1.25. These values perfectly show a complete phase reversal as they are each other's inverse. No differences between mutants and controls were found, neither with the repeated measures ANOVA nor separate Mann-Whitney tests for each comparison.

Modulation indices (Figure 18D), analyzed with a repeated measures ANOVA shows a significant interaction ($p<0.05$), a highly significant difference for layer ($p<0.001$), and a trend towards

a difference for genotype (p=0.05). A post-hoc Newman-Keuls test does not identify any layer as being significantly different, though a trend exists for str. Rad (p=0.06).

3.1.5 Coherence depth profiles for paradoxical sleep reveal layer specificity, sparse changes for theta coherence and decreased gamma coherences

Coherence is a measure that indicates how transmembrane currents recorded in one layer relate to those recorded in another layer. When measuring multiple positions along the same neural structure, as is done here, one can calculate the coherence between transmembrane currents measured at for instance str. Rad (where CA3 inputs into CA1) to any other layer.

In Figure 19, the theta and gamma coherence is calculated for each channel towards str. Pyr (Figure 19A, B, respectively), str. Rad (Figure 19C, D, respectively), and str. LM. (Figure 19E, F, respectively). For all shown graphs, a repeated measures ANOVA reveals, unsurprisingly, a highly significant influence of the layer measured ($p<0.001$). Theta coherence (Figure 19A, C, E) statistical analyses reveal no significant changes for any measured coherence, whether when tested with a repeated measures ANOVA followed by a post-hoc Newman-Keuls test, or when tested with individual Mann-Whitney tests. When each channel's gamma coherence with str. Rad was calculated (Figure 19D), a repeated measures ANOVA revealed a very significant interaction ($p<0.01$), but a post-hoc Newman-Keuls did not indicate any specific layer.

The above analyses were performed on the LFP and CSD, which mainly reflect synaptic inputs. The output of the hippocampus is determined by the firing of hippocampal CA1 pyramidal cells. Therefore, spiking data was extracted from the recordings to see whether hippocampal pyramidal cells fire differently in K_v7/M-current-deficient mice compared to controls.

3.1.6 Neural spiking data show very similar spiking for mutant and control neurons

Neural spiking (unit activity) of hippocampal CA1 pyramidal cells allows the processed input from EPSCs to transfer back to cortical regions. Some of the earlier recordings were obtained from implantations of a 12-site silicon probe with three shanks and four electrodes per shank, with a 25 μm spacing between electrodes. However, these recordings were from a separate set of mice who did not go through the behavioral battery of STSM, open field, spatial novelty and Y-maze: behavioral recordings were exclusively performed with linear 16-site silicon probes. These recordings have poor unit separation as explained earlier (see Chapter 1.2). Therefore, only units from basic sleep recordings from 3-shank probe implanted mice were analyzed. To identify a potential change in the firing pattern of CA1 pyramidal cells, individual unit activity was obtained by high-pass filtering the recorded data and clustering the data points according to their wave shapes (see Chapter 2.5). These results reveal that neurons from mutant mice have very similar firing rates and phase locking characteristics to controls, shown in Figure 20.

Summarizing, K_v7/M-current-deficient mutants show several differences in LFP properties during sleep, both for SWS and paradoxical sleep when compared to controls. Though low in animal numbers, unit spiking data does not suggest a change in unit activity, neither in their firing rates nor in their phase locking.

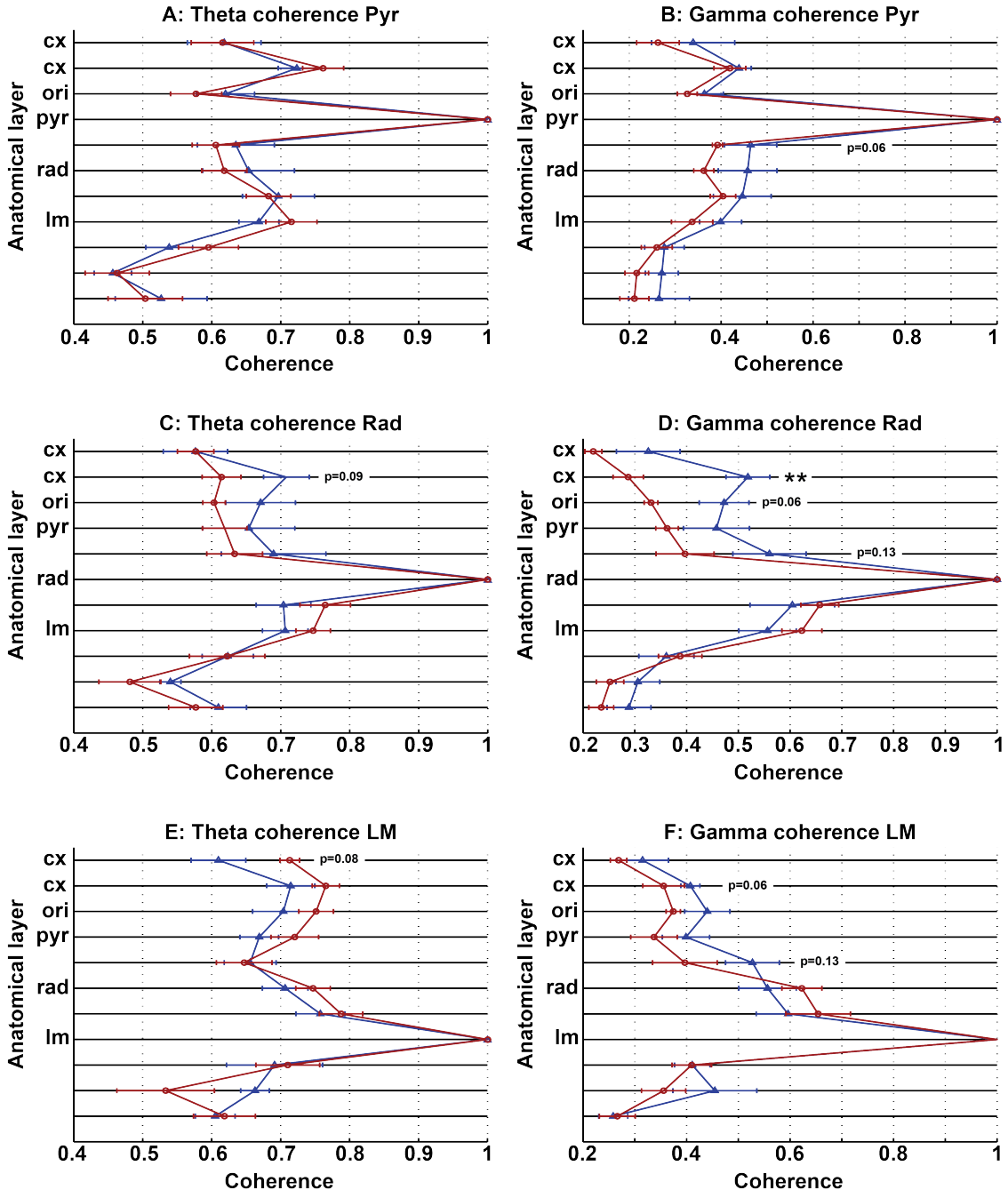

Figure 19: Depth profiles for coherences during paradoxical sleep. **A, B:** Coherences between each channel and str. Pyr suggest similar theta coherence for all layers, whereas gamma coherences suggest a trend at str. Rad. **C, D:** Coherences between all channels and str. Rad. suggest decreased theta coherence for the deepest cortical layer. Str. Ori and the deepest cortical layer are suggested to have decreased gamma coherence. **E, F:** Coherences with str. LM. show no significance, though the trending increases in theta coherence for the upper layers, whereas gamma coherence suggests a decrease.

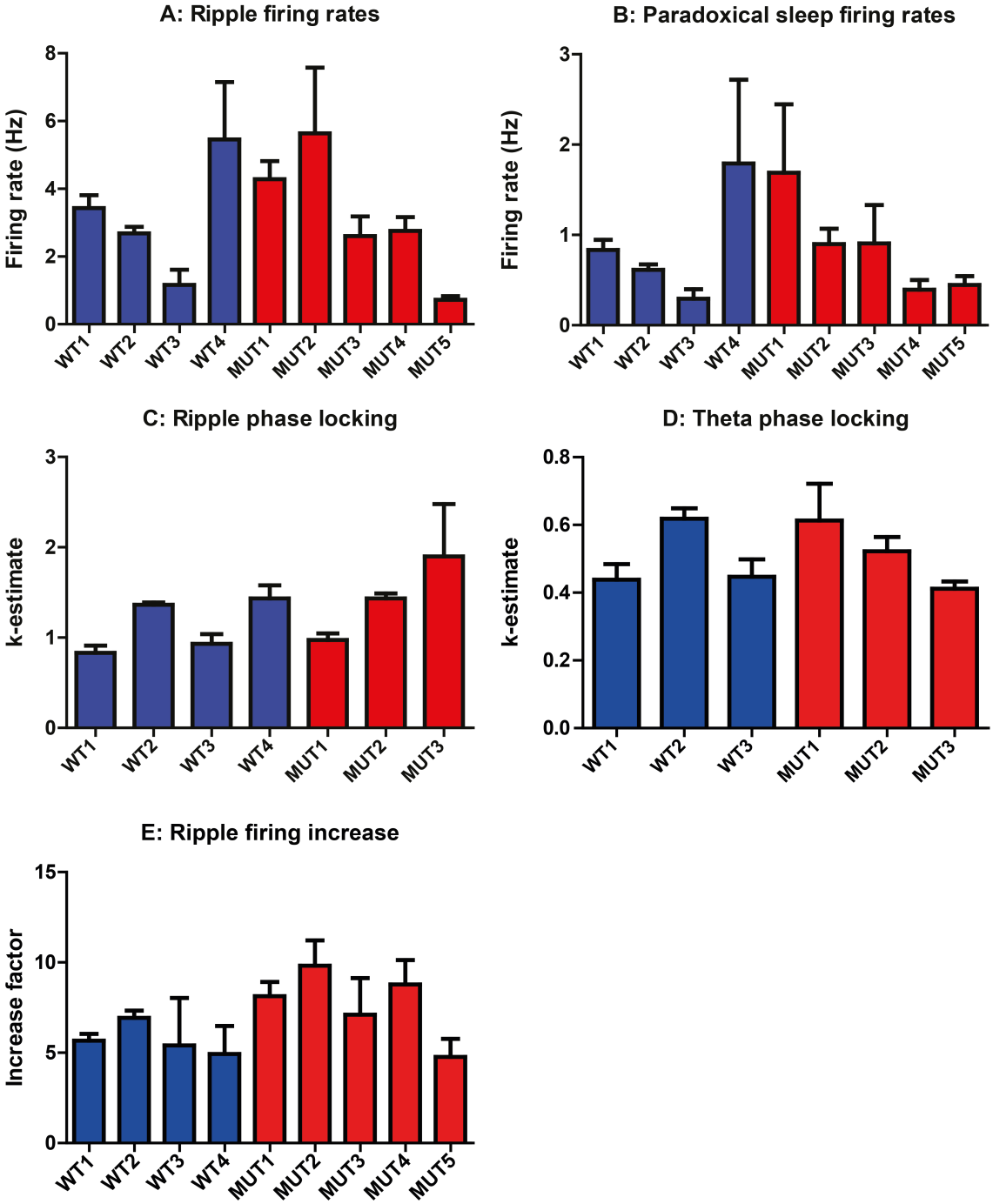

Figure 20: Neural unit spiking results for individual animals. **A,B:** Firing rates during ripples and paradoxical sleep show high variability between units and mice. No trend towards a change in firing rates was observed. **C, D:** Despite a trend for smaller ripples and a reduction in theta power, no trend was seen for phase locking either during ripples or theta oscillations in paradoxical sleep. **E:** Firing rates during ripples generally is higher than before or after ripples. The increase in firing rates between controls and mutants did not show a trend in any direction.

3.2 Single trial spatial memory (STSM) test

The STSM maze is a square maze with 80 cm sides (see Figure 8). In one of three blocked corners, females are present. During the first exposure, the male mouse is supposed to explore the maze and remember the location of the females. During a recall session, spatial memory is tested by observing their preference for the now empty female corner. Preference is calculated by their occupancy of an area 5 cm around the edges of the blocked corners. Electrophysiological recordings were made in their home cage before the exposure (i.e. basic sleep (see Chapter 3.1), during the exposure, and in their home cage afterwards. The following sections show the behavior and network patterns during the initial exposure trial.

3.2.1 STSM exposure induces similar behavior for both controls and mutants, but reveals theta frequency decrease in running mutants

For the STSM behavioral test, each animal is identified by a combination of a color (which signifies either a control or mutant animal) and a symbol. This allows each animal to be tracked for behavior during exposure, certain electrophysiological parameters and recall performance. In Figure 21, all animals, except for one mutant, preferred to spend their time at the female corner, separated as the total time spent at the corners as a percentage of the entire 30min recording (Figure 21A). If their total presence near any of the three corners would be set to 100%, animals would on average spend 33% of their time at each corner if they didn't have any preference. As expected, their preference for the female corner was above chance level for all mice (Figure 21B).

The total distance ran during a certain period can answer the question of hyperactivity, as was seen in the open field test for mutant mice with permanent $K_v7.2$ dominant-negative expression (129). In contrast to the hyperactive epileptic mice, there might be even a slight tendency for these K_v7/M-current-deficient mice to run less (Figure 21C). However, running states are defined as epochs where the mouse's speed is at least 10 cm/s for a duration of at least 1s long (manually corrected for recording artifacts). During these states, the mutants' speed is similar to controls (Figure 21D) and therefore running states can be compared. Interestingly, theta frequency during these running states (Figure 21E) shows a significant reduction in mutants, something that was not observed during paradoxical sleep (Figure 17). Gamma frequency (Figure 21F) on the other hand is unchanged.

3.2.2 Depth profiles show layer specific deficits during running

Running epochs from the STSM exposure session were pooled per mouse and analyzed for the same parameters as those from paradoxical sleep. The results are shown in Figure 22, where theta and gamma powers and modulation index deficits are seen (Figure 22A, B, D). A repeated measures ANOVA again reveals a highly significant influence of layer ($p<0.001$) for all graphs. For theta power, genotype only has the tendency for a significant influence ($p=0.09$), but does show an actual significant interaction ($p<0.05$). A Newman-Keuls post test only reveals a tendency for a reduction for str. LM ($p=0.05$). Gamma power also shows a tendency to be influenced by genotype ($p=0.06$), but no significant interaction.

In the recordings made during paradoxical sleep, genotype showed no effect on theta asymmetry (Figure 18C). Though no significant difference for genotype was found during running (Figure 22C,

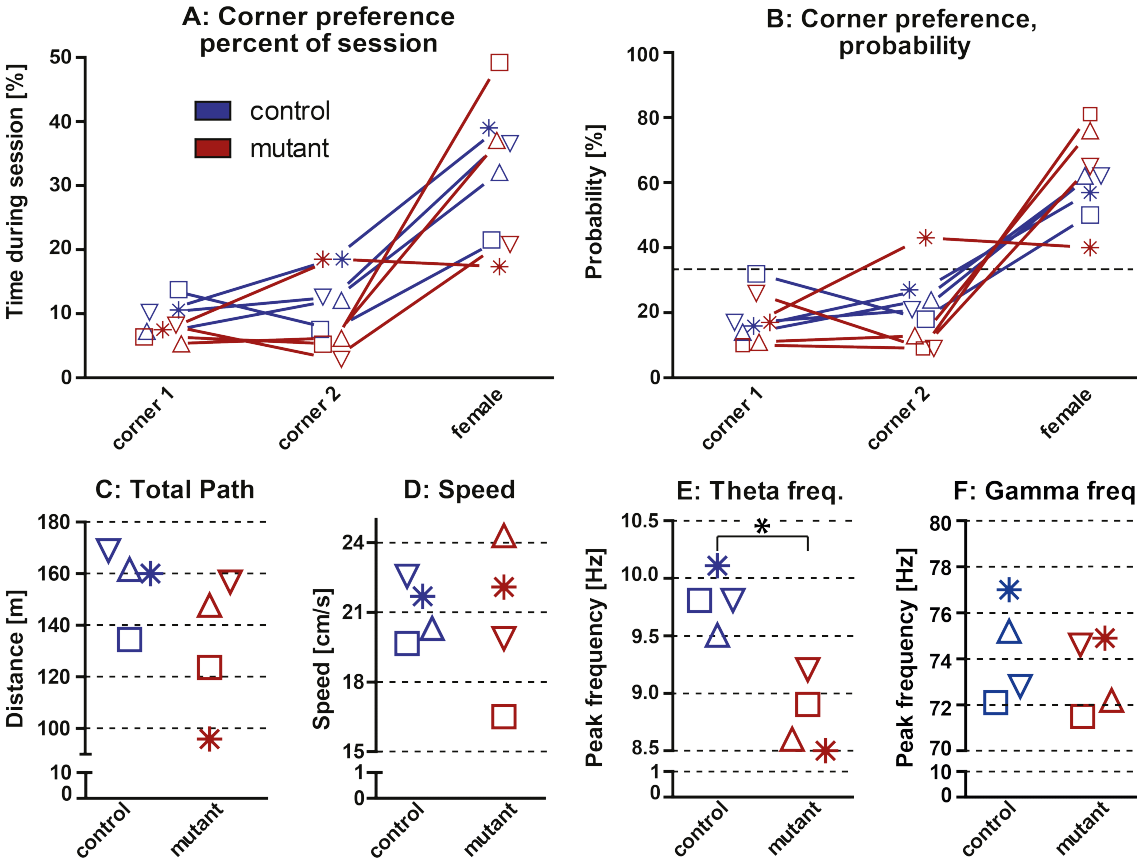

Figure 21: Behavior and electrophysiological parameters during STSM exposure. Each mouse is identified by a color (blue for control, red for mutant) and a symbol. **A:** Except for one mutant mouse, the total time spent at the female corner was similar between mutants and controls. **B:** The probability of choice for either corner was again similar, where all preferences for the female corner were above chance level (dashed line). **C:** There might be a trend towards a reduced path length. **D:** The mice's speed during the detected running epochs is similar between both groups. **E:** Theta frequency is significantly reduced for mutants throughout these running epochs. **F:** Gamma frequency remains unaltered.

$p<0.05$) in a repeated measures ANOVA, Mann-Whitney tests do suggest an alteration between str. Pyr and str. Rad and for str. LM.

The increased theta symmetry for both significantly different layers (Figure 22C) is investigated more closely in Figure 23. Here, it is clearly shown that the reason for the increased symmetry is due to a lengthening of the ascending phase in the layer between str. Pyr and str. Rad and of the descending phase in str. LM. The other phases are similar between mutants and controls. This lengthening of one phase, and hence the lengthening of a single theta cycle, correlates to the decreased theta frequency during running, as shown in Figure 21.

Theta coherences during running (Figure 24A, C, E) show similarities with those during paradoxical sleep (Figure 19A, C, E) to the extent that they show only minor changes between mutants and controls. Unsurprisingly, a repeated measures ANOVA revealed all theta coherence graphs to be significantly influenced by layer ($p<0.001$). No difference was found was found for genotype, though an interaction was identified for when all coherences were compared to str. Rad ($p<0.05$) and the post-hoc analysis identified the lowest layer as being different ($p<0.05$).

For gamma coherences, a repeated measures ANOVA didn't reveal a significant influence of genotype for the coherences to either str. Pyr or str. Rad (Figure 24B, D, respectively), but did

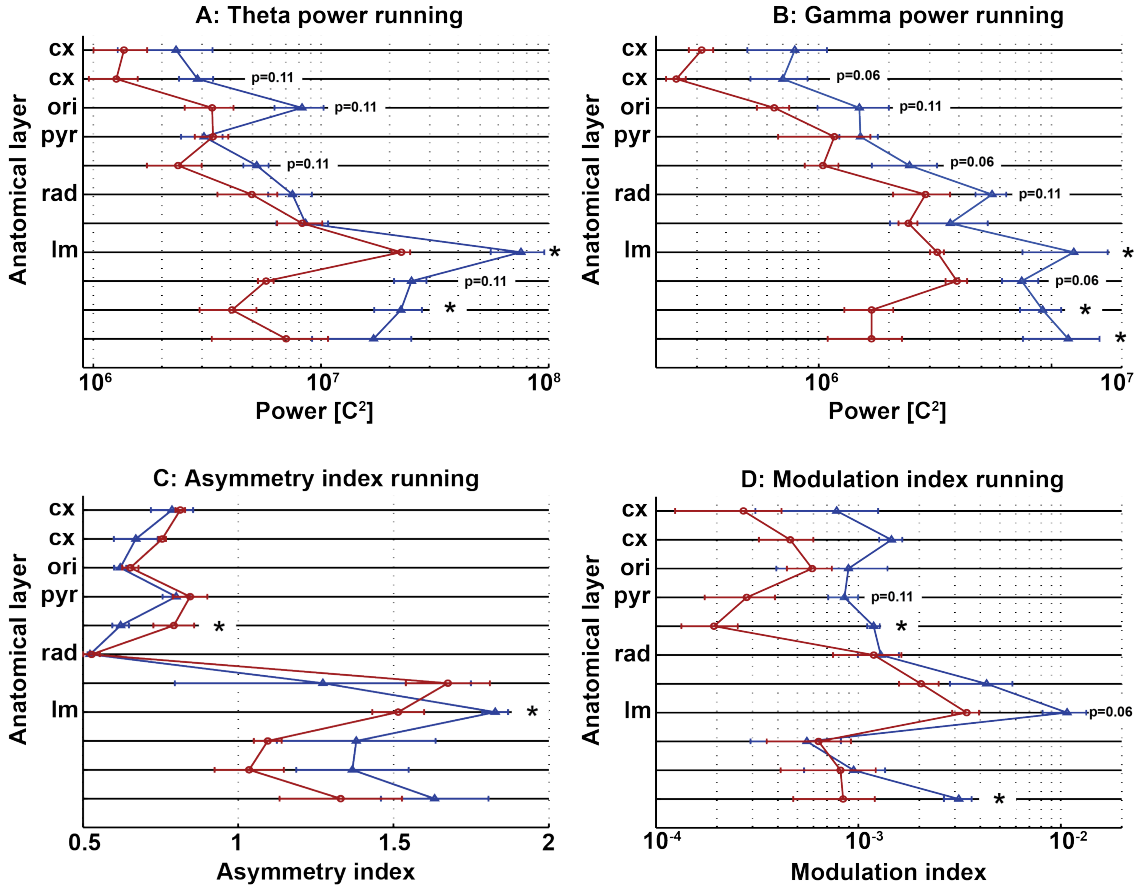

Figure 22: Depth profiles for running CSD results. These depth profiles for running epochs indicate a decrease for theta and gamma power (**A**,**B**) across most layers, though they are similar in str. Pyr. The assymetry index (**C**) shows significant increased symmetry (values closer to 1) between str. Pyr and str. Rad and at str. LM. The modulation index (**D**) seems reduced around str. Pyr, str. LM and the deepest recorded layer. Significant differences for individual layers were detected with Mann-Whitney test, *: $p<0.05$, **: $p<0.01$, additional p-values shown for $p<0.15$.

when coherences of all channels with str. LM were calculated (Figure 24F, $p<0.05$).

Summarizing, these results indicate that what K_v7/M-current-deficient mice may show in altered network patterns during paradoxical sleep does not necessarily predict similar alterations during another theta/gamma-characterized behavioral state like running: some parameters, like theta and gamma powers and modulation index, were reduced for both theta/gamma behavioral states, whereas theta frequency and theta wave asymmetry was only altered during running.

3.2.3 Speed modulates theta and gamma amplitudes, but varies per session

As mentioned before, control and K_v7/M-current-deficient mice have similar speeds during running sessions. This similarity in speed is important as speed can influence the amplitude of theta and gamma oscillations (Figure 25). Since theta and gamma amplitudes during running are suggested to be reduced in mutants for several layers (Figure 22A, B), speed modulation of these amplitudes is expressed as the percentage of change of instantaneous amplitude from a speed of 10 cm/s to a speed of 30 cm/s for any of the shown parameters, to remove this bias. This analysis shows that speed dependency of theta and gamma amplitudes is not straightforward. There are positive

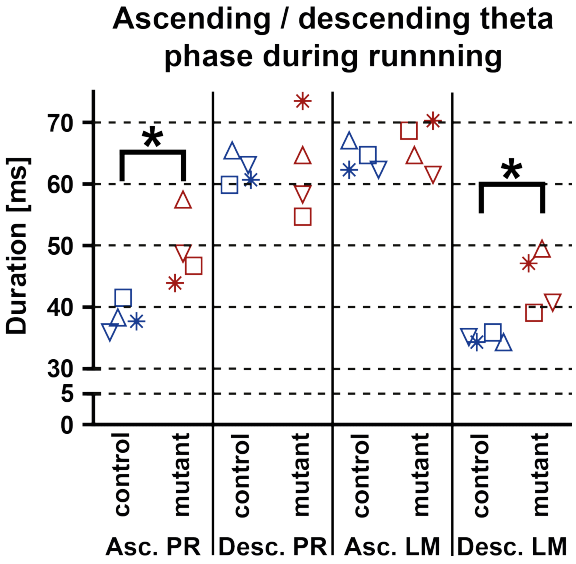

Figure 23: Theta asymmetry changes in str. Pyr-Rad and str. LM. As seen from Figure 22C, the layer between str. Pyr and str. Rad and str. LM. reveal a more symmetric theta wave. Here it can be seen that the reason for the mutants' increased symmetry is due to the lengthening of the ascending phase in str. Pyr-Rad (Asc. PR) and the descending phase in str. LM (Desc. LM). The descending phase in Str. Pyr-Rad (Desc. PR) and ascending phase in str. LM are similar between mutants and controls.

and negative amplitude changes for theta amplitudes with increased speed across str. Pyr, str. Rad, and str. LM (Figure 25A-C). Gamma amplitudes for str. Pyr and str. Rad (Figure 25D, E, respectively) consistently increase with speed, with a possibly minor increase in str. Rad for mutants.

It was noticed, however, that the values obtained from this speed modulation varied strongly per session. Whereas Figure 25 only shows the results for the first exposure session, Figure 26 shows the averaged speed modulation for each animal throughout all six STSM sessions, i.e. exposure, short-term recall, 2x consolidation, and 2x long-term recall. Please note the different y-axis ranges between Figures 25 and 26.

Here, theta amplitude is positively correlated with speed in str. LM (Figure C). This correlation seems to be absent in str. Pyr and str. Rad (Figure A, B, respectively). Gamma amplitude is positively correlated with speed in str. Pyr and str. Rad (Figure D, E, respectively), whereas no clear speed correlation is seen in str. LM (Figure F). Comparing these speed-amplitude correlations between mutants and controls, we see no apparent phenotype for K_v7/M-current-deficient mice, indicating that modulation by speed of theta and gamma amplitudes is not affected in K_v7/M-current-deficient mice.

3.3 Pre- versus post-task sleep

As sleep has been shown to be important for memory consolidation, the electrophysiological parameters during post task sleep were investigated. As before, both theta and gamma oscillations during paradoxical sleep and SW-R complexes during SWS were investigated.

3.3.1 Pre-post sleep does not show changes for paradoxical sleep in control mice

To understand how experience changes paradoxical sleep, many parameters were checked for control mice between pre- and post-task sleep. However, not each sleep session contains a paradoxical sleep phase, especially during post-task home cage sessions when paradoxical sleep occurs later. Therefore, Figure 27 shows all recordings, both for STSM and Open field sessions, where control

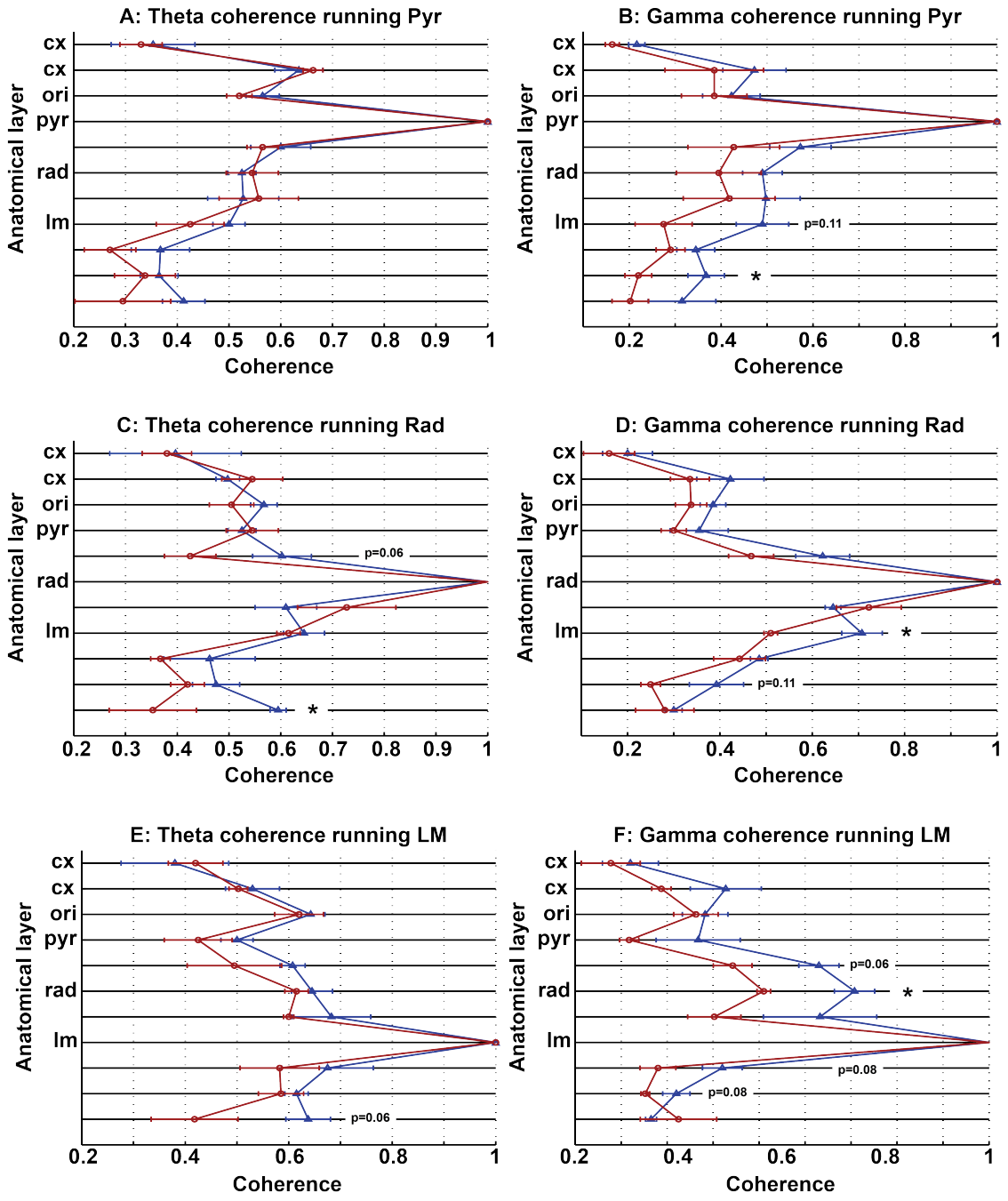

Figure 24: Depth profiles for coherences during running. **A, B:** Coherences for all channels compared with str. Pyr show no changes for mutants, whereas gamma coherence suggests a decrease around str. LM and deeper. **C, D:** Theta coherence to str. Rad trends towards a decrease between str. Pyr and str Rad, together with a significant decrease approximately 300 μm below str. LM. Gamma coherence seems to be reduced for str. LM. **E, F:** Theta coherences with str. LM shows a trend for a decreases coherence approximately 300 μm below str. LM. Gamma coherence seems reduced for a number of layers. Significant differences for individual layers were detected with Mann-Whitney test, *: $p<0.05$, **: $p<0.01$, additional p-values shown for $p<0.15$.

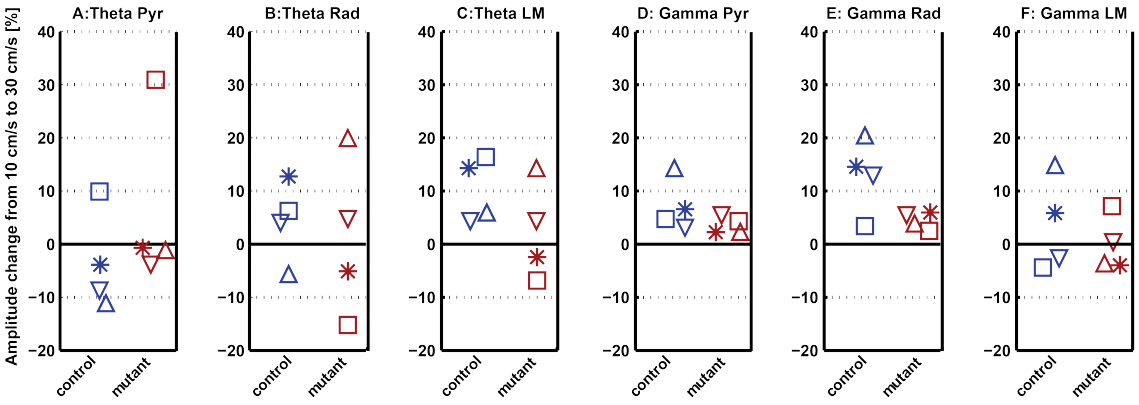

Figure 25: Speed modulation of theta and gamma amplitudes during the first exposure in the STSM maze. Using the same symbols as in Figure 21, the theta and gamma amplitudes at 30 cm/s are normalized to the mouse's theta and gamma amplitudes at 10 cm/s, respectively, and depicted for the three identified CA1 layers.

mice had a paradoxical sleep phase both before and after the behavioral paradigm. Not each mouse had the same number of pre-post comparisons, e.g. the mouse symbolized by the triangle pointing down had four comparisons, while the mouse symbolized by the star had only two. No single mouse had a clear increase or decrease of any parameter that could not be attributed to chance. Since changes in paradoxical sleep parameters for controls did not show a result in any direction, this level of analysis was not repeated on mutant mice.

3.3.2 Pre-post sleep reveals similar changes for ripple parameters in control and mutant mice

Open Field behavior tests consisted of three adjacent days of exploration. For a description of behavioral paradigms for each day, see Chapter 2.4.1. In Figure 28, all four depicted SWS parameters were normalized to the first day pre-sleep and show a clear influence of experience. With few exceptions, ripple occurrence, amplitude, frequency and sharp wave amplitude increased during post-task sleep and clearly dropped before pre-task sleep on the following day, indicating that the initial increase in any of the aforementioned ripple parameters decays back to baseline during

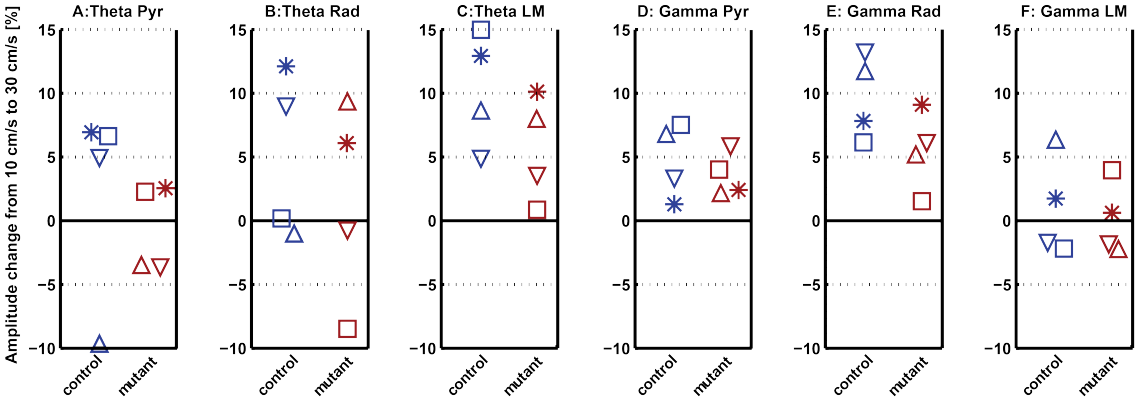

Figure 26: Speed modulation of theta and gamma amplitudes averaged from all exposures to the STSM maze. Using the same symbols as Figure 21, the theta and gamma amplitude at 30 cm/s was normalized to the mouse's theta and gamma amplitude at 10 cm/s and depicted for the three identified CA1 layers.

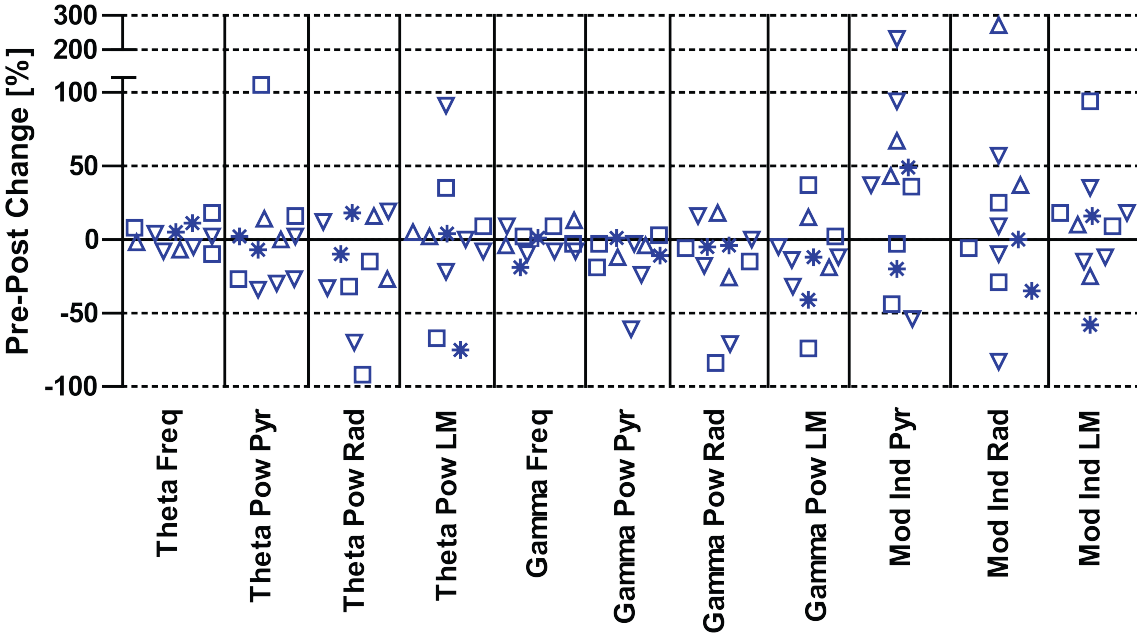

Figure 27: Changes between pre- and post-task paradoxical sleep. Since not every sleep session contains a paradoxical sleep phase, all open field and STSM related sleep recordings from control mice that contain both a pre- and post-task paradoxical sleep phase are compared for several parameters. None of these show a clear tendency for increase or decrease between pre- and post task. Symbols are the same as Figure 21.

post-task sleep. Unsurprisingly, 2-way ANOVA confirmed that the session had a highly significant influence on all four parameters ($p<0.001$). For both ripple and SW amplitude, a significant interaction was calculated ($p<0.05$). It is important to note though, that any possible difference might be due to temporal trends throughout the three days of open field trials. This is likely the case for ripple amplitude: the values of the peak-to-peak voltages show a trending increase for each of the three pre-task sleep sessions – a phenomenon less clear for sharp-wave amplitude. To remove any temporal trend, the pre-post ripple parameters were reviewed after each post-task sleep parameter was normalized to its respective pre-task sleep directly (Figure 29), which is in contrast to Figure 28 where all parameters were normalized to the first pre-task sleep session. In the new analysis, no difference can be seen between mutants and controls, indicating that the interaction seen for ripple and sharp wave amplitude may indeed have been due to temporal trends.

Importantly, though baseline ripple and sharp wave amplitudes are reduced in K_v7/M-current-deficient mice, they are similarly increased during post-task sleep and show similar trends throughout the three-day open field task. Frequency and occurrence also increase similarly during post-task sleep and return before pre-task sleep on the following day. This leads to the conclusion that experience induced network activity changes seem to be unaffected in K_v7/M-current-deficient mice.

3.3.3 STSM recall trials suggest a long-term memory deficiency

It is important to verify whether the changes in network parameters can be directly linked to behavior. As memory fades over time, we checked two separate time points for whether mice remembered in which corner the female mice were located during the exposure trial. During short-term recall trials, performed after being put into the home cage for 75 min, mutant mice did not show a clear deficit (Figure 30A). As preferences for the female corner can be interpreted

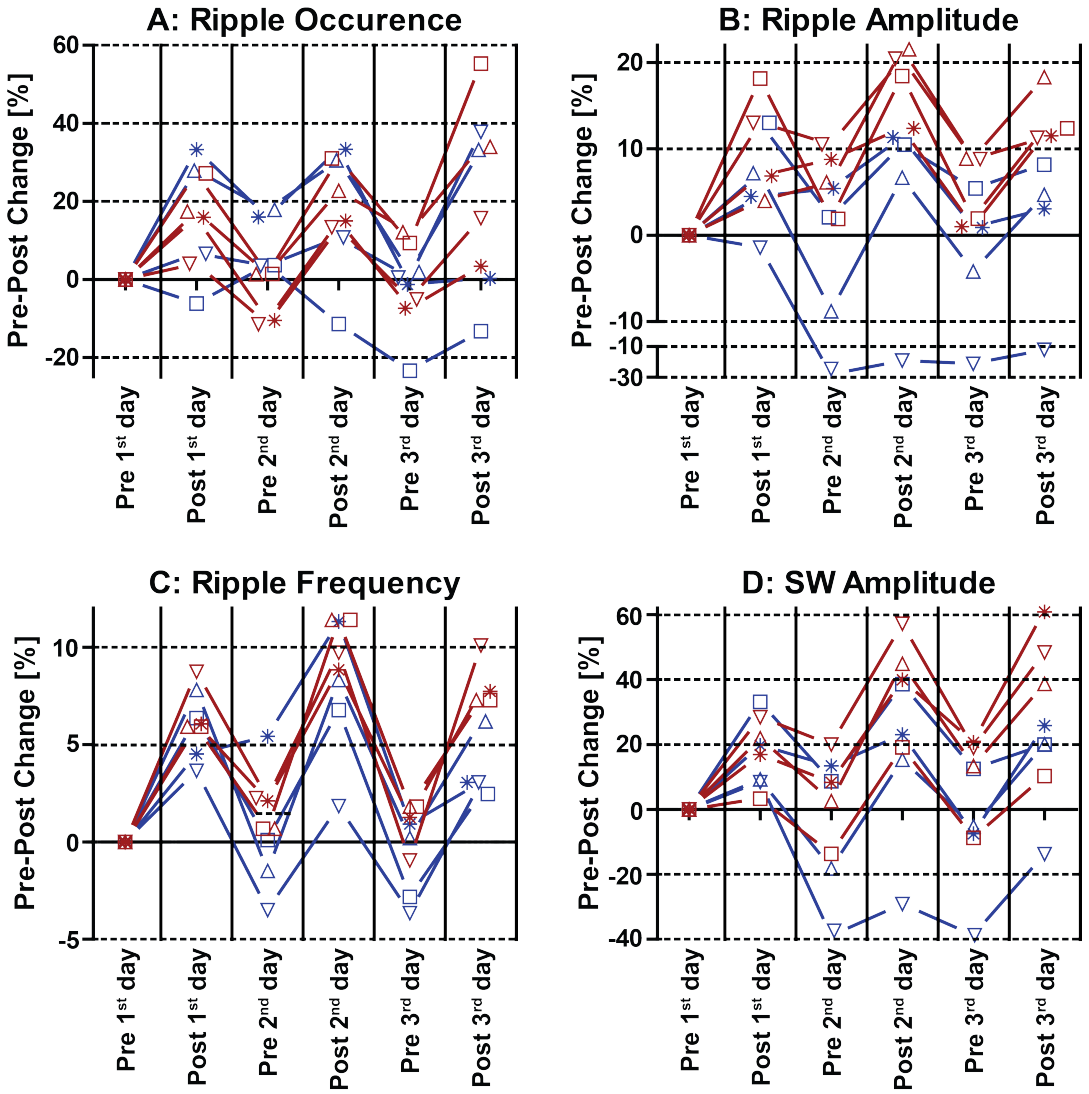

Figure 28: Ripple properties during pre- and post-task sleep in the Open Field maze, normalized to the 1st day pre-task sleep (see Methods 2.4.1 for behavioral paradigms for each day). Differences between mutants and controls may be observed for ripple amplitude post task-sleep on the 2nd and 3rd day and ripple frequency for post task sleep on the 3rd day.

as a measure for memory performance, one mutant performed surprisingly good and one control performed surprisingly bad. It is important to note that performance in a memory task may not solely be due to a fading memory, but also memory extinction (120), where a conditioned response gradually diminishes over time as an animal learns to uncouple a response from a stimulus. As the same group of mice is to be tested for both short-term (75 min) and long-term (24 h) recall, mice were re-exposed to the females in two 30 min sessions after the short-term recall. Then, 24 hours later, these mice were tested for long-term recall. For this test, results were slightly more pronounced, but due to one poorly performing control mouse and the low number of mice overall, no significant difference could be detected (Figure 30B).

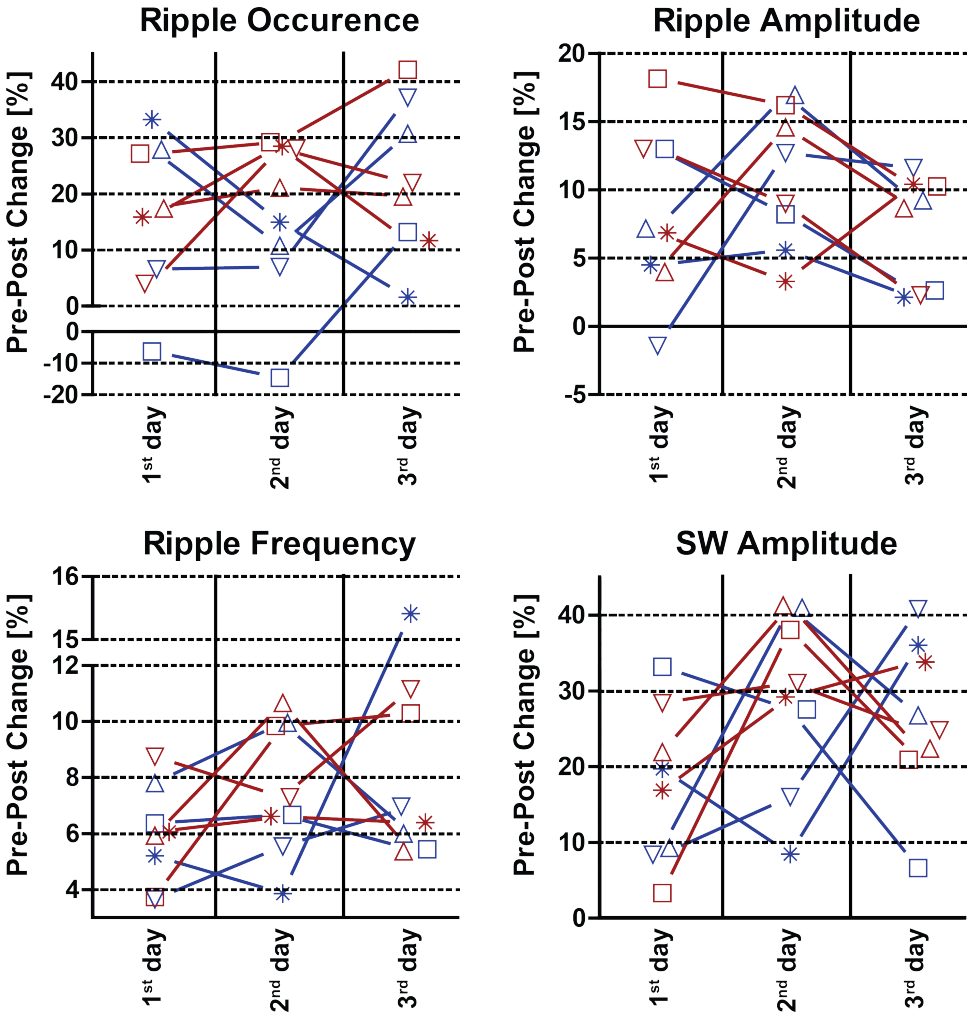

Figure 29: Ripple properties during post-Open Field sleep, normalized to the pre-task sleep of that same day (see Methods 2.4.1for behavioral paradigms for each day). Whereas possible trends were visible throughout the 3-day open field paradigm in Figure 28, no (significant) trends are visible between mutants and controls when one compares individual pre-post task sleep sessions.

3.4 Y-maze

Mice naturally explore their surroundings. In order to explore new environments, they need to remember where they already have been. In the Y-maze (see Figure 8B), mice alternate between three arms. If they remember from which arm they came, they are more likely to choose the other arm when making the next alternation. A decrease in the percentage of choosing the novel arm may indicate a deficit in the working memory.

After being exposed to the Y-maze twice, performing transitions up to a maximum of either 46 transitions or 20 min of exposure, whichever was achieved first, both groups retained a certain degree of working memory, since performances were significantly above chance level (Wilcoxon signed rank test for control and mutant, p=0.06). However, despite the fact that mutant mice took similar times to reach 46 transitions, they were shown to perform significantly worse, choosing a novel arm less often than the control mice (Figure 31A).

Additional investigation into gamma amplitude during a run towards the center of the Y-maze (Figure 31B) does not reveal differences between mutants and controls in any of the three defined

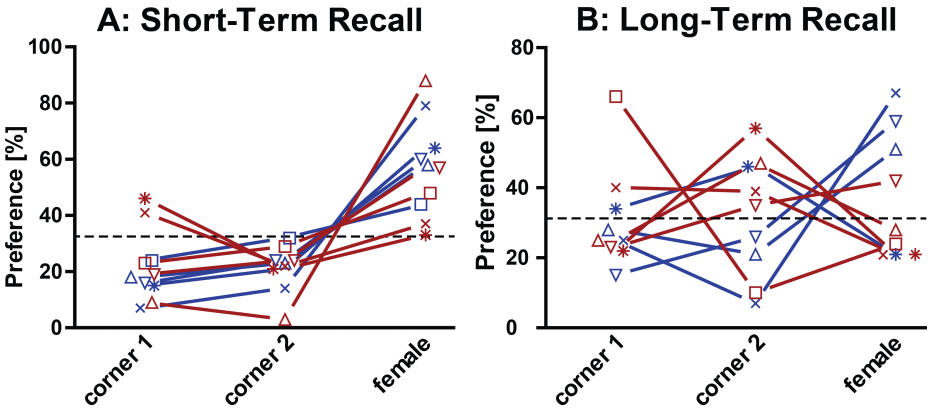

Figure 30: STSM trials. **A:** After exposure to females for 30 min and a subsequent 75 min home cage rest, mutant mice do not reveal a clear deficit in selecting the female corner. One mutant mouse performed better than all other mice, and one control mouse performed poorer than three mutant mice. Even though median performance is better for controls than for mutants, the variance is too large for any statistical difference to be detected. The additional X's represent mice that did perform the STSM paradigm, but did not have usable electrophysiological data. **B:** Long-term recall is slightly clearer in its results, but one poorly performing control mouse prevented the achievement of significance.

layers. Coherence measurements between str. Pyr and str. Rad. and between str. Pyr and str. LM for the starting, middle, and final third of the runs (Figure 31C) also did not reveal a difference between mutants and controls. However, the ratios of those coherences (Figure 31D) do show that during the ending third of the run, all control mice have a higher Pyr-Rad / Pyr-LM coherence ratio than all mutants. This may indicate that control mice hippocampal CA1 neurons 'listen' better to CA3-related inputs compared to K_v7/M-current-deficient mice upon approaching the choice point.

3.5 Spatial Novelty

Moving an object within a previously familiarized maze should increase the mouse's interest in it, as it is a form of novelty. Recognizing that an object has been moved requires the mouse to contrast the map it has in its memory with the changed layout. A relatively reduced interest in a moved object compared to controls, therefore, may reflect an inherent problem with either creating or recalling spatial maps.

The spatial novelty paradigm result is shown in Figure 32, in which an interest shift of 1 means that the relative interest of object X over object Y did not change after object X was moved to the contralateral side (see Chapter 2.4.1). Despite having been exposed to objects X and Y three times prior to moving object X, the interest in the moved object did not increase in all control mice afterwards (interest shift <1). All mutant mice, however, did seem to notice that the object was moved (interest shift >1), indicating that they retained spatial memory (Wilcoxon signed rank test, $p=0.06$).

3.6 Summary of results

K_v7/M-current-deficient mice show changes in several electrophysiological parameters of the hippocampal LFP, which could contribute to the poorer performance in the Morris Water Maze,

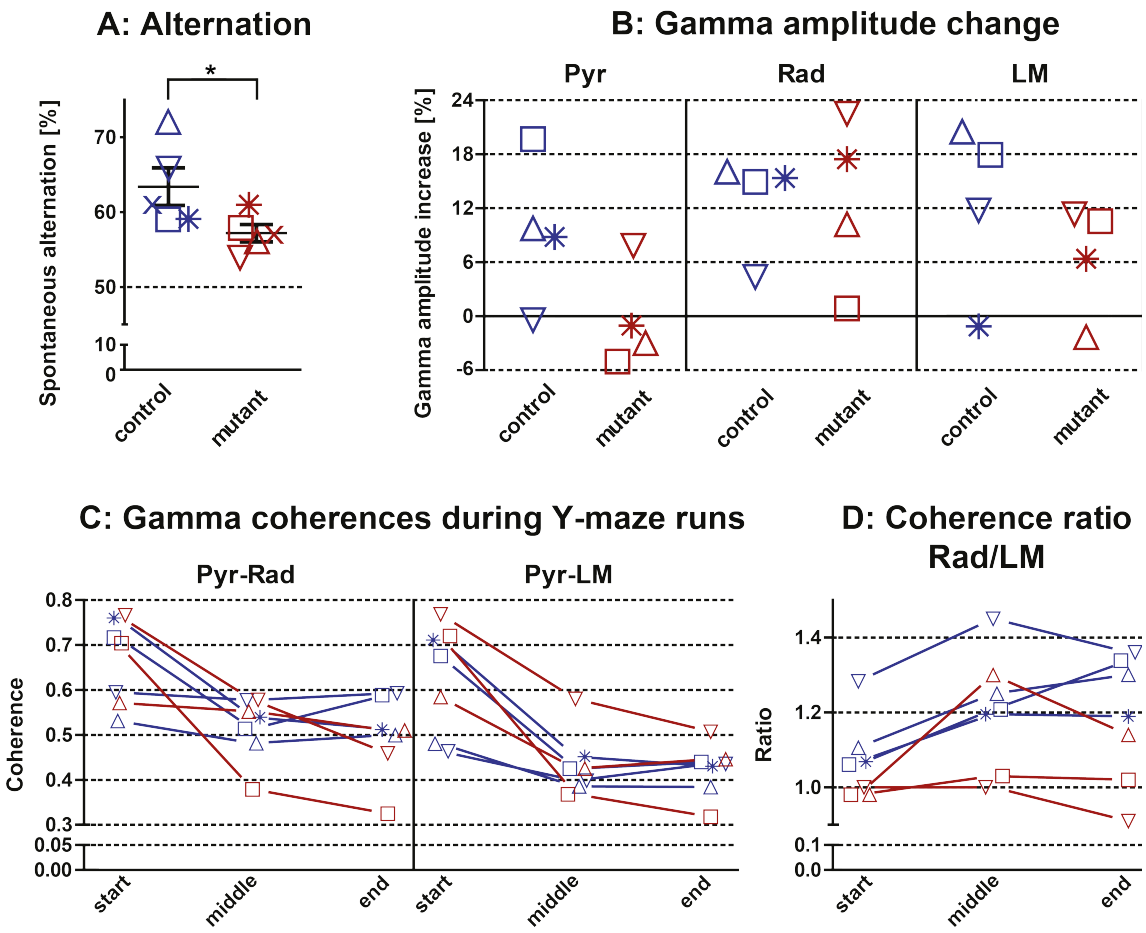

Figure 31: Gamma properties during Y-maze. **A:** Control mice entered an arm not visited prior to the previous transition significantly more often than mutant mice did (dashed line indicates chance level). Symbols are identical to those in Figure 21. The additional X's represent mice that performed the Y-maze paradigm, but did not have usable electrophysiological data. **B:** There was no difference in the change of gamma amplitudes during Y-maze runs in str. Pyr, Rad, and LM when comparing mutants and controls. **C:** Coherences between str. Rad and str. LM during the initial, middle, and final thirds of their Y-maze runs showed no clear distinction between mutants and controls. **D:** Coherence ratios might suggest a difference between the two groups.

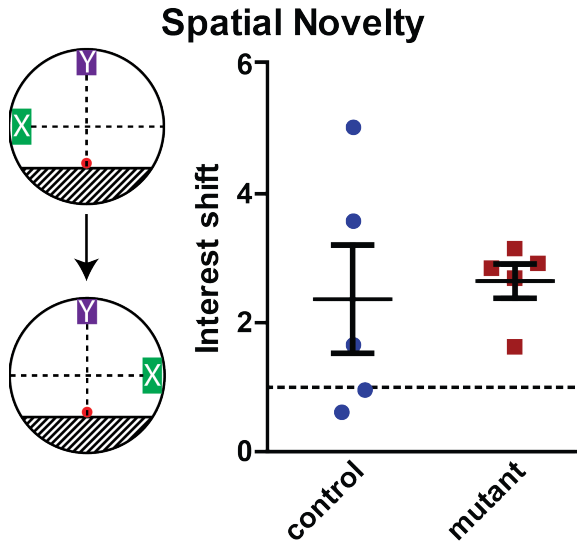

Figure 32: Exposure to a moved object did not increase the interest for the control mice overall, and the interest shift for two control mice dropped below 1 (dashed line). The interest level for all of the mutant mice increased regarding the moved object, suggesting that they noticed a change in the spatial layout of the maze.

observed before (133), the poorer performance in the Y-maze shown in this thesis, and a tendency toward a poorer performance in the STSM task as shown in this thesis. Surprisingly, however, no indication of changes in basic firing properties of CA1 neurons was seen to correlate with these putative cognitive deficits. Interestingly, running epochs revealed a theta frequency reduction and theta wave asymmetry not previously observed during paradoxical sleep. The influence of experience on electrophysiological parameters during SWS for SW-R complexes is very similar to controls. An additional Y-maze analysis suggests that CA3-CA1 communication is impaired in K_v7/M-current-deficient mice when a spatial choice must be made, as can be seen from a reduced Rad-to-Pyr / LM-to-Pyr coherence ratio upon approaching the choice point.

Discussion of methods

Several methods applied in this thesis are relatively new. A large part of the MATLAB scripts used were self-written, including [1] the analysis of behavioral parameters during open field, spatial novelty, STSM, and Y-maze tasks from positional data extracted from the Neuralynx system, [2] detection of running states, [3] speed versus theta/gamma amplitude correlations, [4] ripple detection and analysis, [5] sharp-wave analysis, [6] theta wave asymmetry, [7] implementation of the Kullback-Leibler divergence, [8] implementation of the Rayleigh test for analysis of phase locking, [9] implementation of the electrostatic forward solution for CSD calculation, [10] additional Y-maze analysis, and [11] plotting tools. These scripts are now available for application to other similarly recorded datasets for quick processing.

Although there is no doubt about the accuracy of these scripts and their output, the conclusions drawn from them are subject to interpretation. Below, several points of discussion about the methods applied are listed.

4.1 Genetic mouse model

The expression of a dominant-negative $K_v7.2$ subunit allows for non-functional K_v7/M-channels. This approach is better than a $K_v7.2$ KO model, because then the absence of $K_v7.2$ subunits would not prevent $K_v7.3$ and $K_v7.5$ to form functional channels at the AIS. In the model used in this thesis, there is still an expression of endogenous $K_v7.2$ subunits, but from the reduction of K_v7/M-currents seen in vitro (133), this does not seem to be a hindrance to K_v7/M-current suppression.

$K_v7.2$ is expressed both in pyramidal cells and interneurons (29; 34; 41). The change in excitability due to the expression of the dominant-negative transgene (133), together with histology confirming the transgene's expression (unpublished results), was verified only in pyramidal cells. However, from the genetic model, i.e. expression under the prion protein promoter, it is assumed that this transgene may similarly affect interneurons. Importantly though, heteromeric $K_v7.3/7.5$ channels are not affected and so care should be taken on whether there is a functional significance between them. Since $K_v7.5$ expression is more abundant in CA3 of the hippocampus, our approach might have created an imbalance between CA1 and CA3 excitability, with a more significant reduction of K_v7/M-currents in CA1. However, $K_v7.5$ subunits are found both at the AIS and, uniquely, at the postsynapse (52). The lack of colocalizing $K_v7.3$ subunits at the postsynapse suggests that these $K_v7.5$ channels are homomeric. This might be related to the fact that $K_v7.5$ subunits do not have an ankyrin-G binding motif (129), which guids K_v7 channels to the AIS (156). First, this suggests that pairing a $K_v7.5$ with a 7.3 subunit overwrites the localization from the postsynapse to the AIS. Second, it also suggests that $K_v7.5$ might have a postsynaptic targeting motif, since disruption of ankyrin-G binding does not result in postsynaptic relocalization of $K_v7.3$ to the postsynapse, but rather a lack of specific targeting (156). Furthermore, it might be that the increased expression of $K_v7.5$ in CA3 will increase the likeliness of forming $K_v7.5$ homomeric channels specifically and so the observed unique role of $K_v7.5$ homomeric channels might be more significant in CA3, compared to CA1.

Expression of a dominant-negative $K_v7.5$ subunit has been shown to create an imbalance in

excitation/inhibition (52), where spontaneous IPSCs on pyramidal cells were increased both in amplitude and occurence due to increased interneuron firing. $K_v7.5$ colocalization with gephyrin suggests that $K_v7.5$ homomeric channels are located at inhibitory synapses (52). Importantly, the electrophysiological results that were found in this approach included decreased ripple occurence and a lack of theta power loss. These results are very interesting, underlying the importance of distinguishing invidual subunits and affecting the conclusions to be drawn from the results after genetic interference.

In our approach we are expressing an additional subunit on top of the endogenously present channels. Because $K_v7.2$ only binds to $K_v7.3$, the now more abundant (endogenous plus transgene) $K_v7.2$ expression increases binding to the endogenous $K_v7.3$. This reduces the likeliness of a $K_v7.3$ binding with a $K_v7.5$, which in turn makes homomeric $K_v7.5$ channels more likely. Similarly, the expression of the dominant-negative $K_v7.5$ approach (52) could shift the balance in the opposite direction, where $K_v7.3$ now binds more to the abundantly present $K_v7.5$, reducing the number of functional channels at the AIS. To what extent this happens is unclear as stochiometric information on endogenous and trangene expression levels is not available. However, if such a shift would be significant in the case of the dominant-negative $K_v7.5$ - significantly fewer functional K_v7 channels present at the AIS - then it would be expected to see some similarities between those results (52) and the results presented in this thesis, like loss of theta power. This was however not reported in the dominant-negative $K_v7.5$ approach (52). Similarly, if the dominant-negative $K_v7.2$ approach in this thesis would cause a significant shift towards more functional $K_v7.5$ channels, our results should possibly contrast those obtained from a lack of functional $K_v7.5$ channels (52): we should have seen an increased ripple occurence, yet we don't. Therefore, it is assumed that the conclusions drawn on this data cannot be attributed to interference with specific $K_v7.5$ function. The last point is that the genetic approach in this thesis clearly reveals a critical developmental period (133), something not taken into account in the dominant-negative $K_v7.5$ approach. This makes it even more difficult to compare results and should be kept in mind when conclusions are drawn from the results presented here.

4.2 CSD calculation

The CSD calculation presupposes the insertion of a recording probe perpendicular to a parallel set of spatial planes. However, the dorsal hippocampal CA1 str. Pyr has a curved structure, like an inverted U, along the mediolateral axis. Therefore the exact insertion site may have varied from animal to animal, resulting in increased CSD variability between mice. This variability appears to not have been, in fact, very strong because in several layers mutants showed significant power reductions. Likewise, it is not assumed that differences in CSD-calculated currents between controls and mutants occurred as a result of anatomical distinctions because none were previously found, nor were obvious differences seen in brain sections analyzed in this study.

For CSD calculation, conductivity is assumed to be homogeneous along the CA1 axis, although some inhomogeneity is likely to exist (79). These conductivity differences across the hippocampal layers may confound results from CSD analyses when comparing control and mutant mice. However, as the genotype-specific theta and gamma power changes, shown in Figure 18A and B, are significantly altered in several anatomically adjacent layers, local conductivity inhomogeneities are unlikely to systematically contribute to the effects observed.

4.3 Ripple detection

The method for setting detection and border thresholds (deviations from the mean by a certain number of SDs) should be carefully applied since most ripple parameters are interconnected. For example, if ripple length was significantly increased in mutant mice, the SD of the signal could potentially also increase. As a consequence, higher SDs could shift the detection limit towards higher-amplitude ripples. Another possibility is that a significantly reduced occurrence of ripples in mutant mice would reduce the SD of the signal and shift the detection limit down to include lower-amplitude ripples. The advantage of this SD-based detection method, however, is that the varying amplitudes, based on non-physiological parameters such as exact probe position or electrode impedance, for both individual recordings and specific mice are taken into account. This results in a less variable occurrence. Conversely, using a fixed detection threshold – measured in Volts rather than in multiples of SD – would ensure the detection of ripples within a certain amplitude range. However, if that amplitude were decreased in mutants (as was the case in this study), this method would detect fewer ripples.

Since the tendency toward reduced ripple amplitude is in agreement with a significant decrease in sharp-wave amplitude and no other ripple parameters were significantly different between the genotype groups, the interdependency of the parameters tested is not likely to cause a detection bias with respect to the method applied.

Detection of SWS periods in this study may be limited because, due to depth-profile recording across hippocampal layers, no cortical LFPs were available that could have provided direct information about the occurrence of spindles or low-frequency delta waves. The short ripple-free periods, mentioned in Chapter 3.1, could be a different sleep state. If these ripple-free periods do not reflect SWS, the total duration of 'real' SWS will be strongly reduced compared to what was used in this thesis. Therefore, it may be possible that ripple occurrence continued to be underestimated in addition to the estimated 23.8% false-negative detection. However, since sleep progression was unrelated to genotype, the bias that may have been inherent to the method used is assumed to have equally affected both groups.

4.4 Modulation index

The present adaptation of the Kullback-Leibler divergence is used to measure the flatness of the distribution of gamma amplitudes during the theta cycle, where 0 is a completely flat distribution and 1 means that gamma amplitude is 0 in all except one bin. The MI is based on theta phase, but not on theta amplitude. It is furthermore based on gamma amplitude, which, for the purpose of this calculation, was normalized to 1 for a 360-degree cycle. Therefore, from a purely analytical point of view, neither theta nor gamma amplitude influences the MI. It is unlikely that the detection of theta phase at lower amplitudes was distorted, because theta oscillations were clearly visible in the raw LFP traces and theta wave asymmetry was similar in both groups. Therefore, the reduced MI is assumed to be a physiological phenomenon. One point of interest in this context is that the reduced theta power input will result in a less phasic excitation of interneurons due to the loss of functional K_v7/M-current and, in a less synchronized gamma rhythm, lead to both a reduced theta phase relationship and an overall reduced gamma power. At first glance, it might appear that the data obtained contradict this oversimplified view: Figure 18 clearly reveals that despite significant theta and gamma power decreases in almost all layers, modulation indices were reduced

in only one subset. However, interneurons in CA1 are diverse and include populations whose dendrites, soma, and axon terminals span from str. Or to str. LM. (92). Therefore, the theta band currents recorded in a single layer do not necessarily reflect the input into the interneurons that give rise to the gamma band currents in that same layer. Furthermore, each recorded potential is a superimposition of local synaptic input, return currents from synaptic input elsewhere, intrinsic currents, etc. Interference between them could therefore counteract a loss of modulation.

4.5 Speed modulation of theta and gamma amplitude

The method to analyze the changes in theta and gamma amplitudes during different running speeds (Figure 25 and 26) showed strong variability between sessions, but it is unclear whether this is due to analytical or physiological reasons. It is possible that if a mouse runs at a reduced speed, the linear fit on a scatter plot with amplitude vs. speed would bias itself, because the fit might actually not be linear: speeds between 10 and 20 cm/s might not increase in amplitude as much as speeds above 30 cm/s. However, no correlation or trend was seen when comparing individual speeds (Figure 21C) with their amplitude changes.

4.6 Statistics

Statistical differences between groups in a single parameter were calculated with Mann-Whitney tests. For the analysis of depth profiles, one can argue that a 2-way ANOVA would be the appropriate test because there are two variables, genotype and layer, that could influence a third variable, e.g. theta power. Furthermore, there is a degree of matching: the paradoxical sleep theta power of one mouse in str. LM may be predictive of its theta power in str. Pyr due to propagation of electrical signals through the neurons. Therefore, a repeated measure 2-way ANOVA, rather than a regular 2-way ANOVA without matching, would be more appropriate.

In contrast, layers are anatomically distinct from each other, receiving different synaptic inputs, i.e. CA3 input through the Schaffer collaterals into str. Rad and entorhinal cortical input into str. LM, not to mention the different classes of interneurons that terminate along the entire CA1 axis. Therefore, layers may be regarded as separate. Indeed, from literature it is evident that the measure of theta power in str. LM, though predictive, is not similar to that in str. Pyr: power in str. LM is far higher than in str. Pyr. Therefore, the absolute variability of the data is also highest in LM and any post-hoc test will therefore be influenced by the results from str. LM. Though it is generally agreed that 0.05 is the threshold for significance in post-hoc tests, individual Mann-Whitney tests might suggest a change between controls and mutants. Therefore, non-significant post-hoc results may therefore still be physiologically relevant, especially if there are several, anatomically adjacent layers with similar trends.

4.7 Theta wave asymmetry

LFPs measured in one layer represent an integrated signal that includes local synaptic input, return currents from synaptic currents in other layers, intrinsic currents, and volume-conducted fields. The gradual phase shift between str. Pyr and str. LM reveals the existence of multiple theta dipoles. In general, asymmetry can be established by a single dipole if the depolarization

resulting from synaptic input takes a shorter amount of time than the repolarization back to the RMP. Indeed, EPSPs are generally not symmetrical.

For the running session during STSM exposure (Figure 22), Mann-Whitney tests revealed a significant difference in theta wave asymmetry for the layer spanning str. Pyr and str. Rad, and for str. LM. One might argue that a significant difference detected with a Mann-Whitney test on a depth profile is too weak, but other tests that take into account the variance from all layers and simply do not detect this difference. Furthermore, the reduced asymmetry in mutants, both above and below the phase reversal, indicates that this is not just a matter of chance or analytical bias, but spans anatomical layers. Of note, theta wave asymmetry per mouse was calculated from the average asymmetry of all theta cycles within its running states, which reduced the variability within a single recording.

In addition, dissection of the asymmetry ratios in the ascending and descending parts of the waves (Figure 23) clearly shows that only one phase of the theta wave is significantly affected between mutants and controls. Furthermore, the lengthening of one of the phases for mutants corresponds to the decreased theta frequency (Figure 21). Therefore, the reduced asymmetry detected in mutants is deemed to be physiological.

4.8 Behavioral paradigms

For open field sessions, initial trials were performed differently. Several days before any behavioral test was conducted, a small enclosure (20 cm x 10 cm) was filled with bedding and nesting material and placed inside the home cage in order for the mice to become acclimatized to it. This small enclosure was then placed within the same circular open field as in Figure 7A, across from where object Y would be placed, but without a wall added.[i] The mouse was allowed to exit the enclosure and to explore the open field. The inclusion of the small enclosure was to help relate the likelihood of the mouse exploring the environment with its level of fear of a novel environment. Furthermore, if a mouse decided to explore the environment, the decision to do so would be spontaneous rather than forced, as it would be when placing a mouse inside a maze without the familiar enclosure, e.g. during an STSM session. With this familiar enclosure, mice were allowed to overcome their fear of a novel environment so that their motivation for exploration was similar across trials, thereby possibly reducing the variability in recorded brain activity. Additionally, if the mouse wanted to explore, then the interest it showed in an object – the duration of the mouse's presence within a 5-cm border around the object – was more likely to be real and less affected by stressors.

However, mice often preferred to stay within their enclosures, resulting in short exploration periods, which made the spatial novelty test difficult to interpret and highly variable. Sufficient exploration is required to map and remember the environment and to notice subtle changes, such as the changed position of an object. Therefore, the use of the enclosure was discontinued. As the open-field experiments were no longer conducted under 'free-choice' conditions, the presence of the mouse near an object did not necessarily reflect interest or motivation, and stress levels may have been increased, making the performance of control mice in the spatial novelty task more variable (Figure 32). This is also applicable to the STSM paradigm where a mouse may have been resting near the non-female corners by chance due to its relatively safe position close to the wall, rather

[i]The wall was added later to induce an asymmetry in the maze to make the spatial novelty paradigm possible. The placement of the enclosure already induces an asymmetry, which therefore would not have required the additional wall.

than being interested in that specific corner. This additional variability may have been the reason why one control mouse failed to show a higher than chance level interest in the female corner during the 24 hr recall (Figure 30B).

Discussion of results

Do the results in this thesis show relevant changes in electrophysiological or behavioral parameters that could support the previously found cognitive deficiencies? Furthermore, do these results point to a mechanistic change of underlying neurophysiological processes of cognition upon ablation of K_v7/M-currents? Despite some reservations about the applied methods, this chapter encompasses conclusive confirmation of both and suggests additional analytical and experimental efforts to strengthen the conclusions made and to investigate this topic further.

5.1 Theta and gamma power

The contribution of K_v7/M-channels to theta frequency resonance could help explain the observed reduction of theta power in practically all CA1 layers during paradoxical sleep (Figure 18A, B) and in several layers during running (Figure 22A, B) in K_v/M-channel-deficient mice. The level of contribution from specific sources to the recorded LFP is debatable (21; 143). However, the finding that a change in dendritic RMP was reduced compared to the soma upon application of K_v/M-channel blockers (156) and that at distal dendrites K_v/M-channel-mediated resonance was not found (80) suggests that reduced theta power in CA1 str. LM is unlikely to be the direct consequence of an intrinsic CA1 K_v/M-current deficiency. Therefore, the most likely reason for the lowered theta power is a reduced strength and/or less synchronized synaptic input into the distal apical dendrites via the perforant path. Since the prion protein promoter is active in the entire brain (179), structures that target the CA1 region are also deficient in K_v/M-currents if they form tetramers with the dominant-negative $K_v7.2$ subunit. Indeed, K_v7/M-currents were found in entorhinal cortex layers II and III (122). It is therefore very well possible that those structures have an altered output towards the hippocampal CA1.

The reduction in theta and gamma power reveals a possible correlate of the impaired performance of K_v7/M-current-deficient mice in the water maze (133), as theta and gamma oscillations are thought to be associated with navigation, learning, and memory (24). In addition to epilepsy-associated memory impairment, K_v7 dysfunction-induced changes in hippocampal theta/gamma oscillations may also contribute to cognitive problems in human patients with mutations in *KCNQ2* (12). Indeed, a loss of theta and/or gamma power was found to correlate with deficiencies in learning and memory when considering several functionally distinct factors like age (4), a metabotropic glutamate receptor (78), chemotherapy (123), gap junctions (149) or a metalloproteinase (142). Additionally, both *in-vitro* and *in-vivo* experiments have shown a reduction in theta/gamma amplitude when K_v7/M-current activity is acutely reduced (11; 56; 81; 80; 139).

5.2 Coherences

Coherence analysis for basic sleep reveals sparse changes: only gamma coherences with str. Rad and the upper channels suggest a change for mutants (Figure 19). Since there is no indication that the coherence between str. LM and these upper layers is disturbed, the loss of coherence between these channels and str. Rad for mutants suggests a reduced common input from CA3 onto str.

Rad and onto the basal dendrites. On the other hand, the soma from K_v7/M-current-deficient mice may be less leaky which may result in a change in the propagation of electrical signals from str. Rad across the soma towards the basal dendrites. Since recorded currents are affected by both factors, a direct conclusion on the changes in coherences is difficult to draw.

5.3 Theta frequency and asymmetry

The data presented here reveal a significant reduction in theta frequency in the CA1 pyramidal layer during running (Figure 21), despite similar speeds overall between groups. Even though CA1 pyramidal neurons are resonant in the theta range, the rhythm is proposed to be generated in the medial septum (59; 136). Since the dominant-negative transgene is expressed under the prion protein promoter, medial septal neurons are also likely to be K_v7/M-current deficient. A lack of K_v7/M-current-mediated subthreshold theta resonance in these neurons might be responsible for reduced theta frequency.

The change in theta frequency and theta wave asymmetry was found during running. In a recent study, a correlation was found between theta frequency, or theta wave asymmetry, and speed (159). From this study, however, it is not clear whether the local CA1 circuitry, when driven at a higher theta frequency by the medial septum, is the causal factor underlying the occurrence of a more asymmetric wave, whether medial septal input itself becomes more asymmetric upon an increase in theta frequency, or whether both phenomena are generated separately. An optogenetic approach aimed at stimulating the medial septum at several theta frequencies would allow the theta asymmetry of an emerging oscillation in str. Pyr to be investigated and might reveal a causal link.

Also of interest is the fact that the lower theta frequency and changed asymmetry only occurred during running and not during paradoxical-sleep. This may be suggestive of evidence that paradoxical sleep theta oscillations are generated through different mechanisms. However, in this context it is important to note that paradoxical sleep occurs at a lower frequency (7.6 Hz) than running (9.6 Hz). It may therefore be hypothesized that a similar theta-generator is used during paradoxical sleep and running, and that the K_v7/M-current deficient mice have a frequency cap. Future research might look for a within-animal correlation between instantaneous speed and cycle lengths. This could give insight into whether K_v7/M-current deficient mice have similar theta frequencies at lower speeds where theta frequency is more similar to how it presents during paradoxical sleep, and whether their theta frequencies lags behind at higher speeds. If this is not the case, and theta frequency is lower during all speeds, including approximate paradoxical sleep frequencies, the findings would point towards different theta generating mechanisms for paradoxaical sleep and running. An additional analysis of the within-animal correlation between cycle-length and cycle-asymmetry would also be able to determine whether frequency and asymmetry are two separate phenomena or whether they are more directly related.

5.4 SW-R complexes

Ripples are generated in CA3 when desynchronous firing of pyramidal cells crosses a critical threshold that through recurring connections leads to further recruitment of pyramidal cells. This will then generate a gradual EPSC buildup which subsequently recruits interneurons to create the typical high frequency oscillation (148). As mentioned before, no literature is available on the

contribution of K_v7/M-currents to ripples. Although *in-vitro* work in these mice reveals hyperexcitability (133) and another study showed a relationship between excitability and ripple occurrence (148), the data in this thesis do not confirm this association, as ripple occurrence in mutants is comparable to controls. Also, the role K_v7/M-currents might play in spike frequency adaptation to limit ripple length is not confirmed as ripple lengths are similar between mutants and controls. Instead, the results in this thesis reveal a reduction in ripple and sharp-wave amplitudes in a K_v7/M-current-deficient mouse model, but it remains unclear whether K_v7/M-currents are directly involved in the amplitude reduction of both ripples and sharp waves, or whether the underlying reason is due to a secondary compensatory mechanism. It would be interesting to use a specific hippocampal slice preparation for the induction of spontaneous ripples in vitro (75), and to apply K_v7/M-channel blockers to see whether an acute effect on ripple parameters is induced by acute K_v7/M-current ablation. This could partly answer the question of whether K_v7/M-currents are directly involved in ripple generation. If no acute involvement can be confirmed, a compensatory effect may be the more likely factor contributing to the reduced ripple and sharp-wave amplitudes in this thesis.

5.5 Unit spiking

Firing activity from neurons isolated from K_v7/M-channel deficient mice does not show a tendency toward either higher or lower firing rates, in contrast with patch-clamp experiments previously performed using this mouse model, which revealed that hippocampal CA1 neurons are hyperexcitable (133). However, the increased firing rates of the patch-clamp experiments were based on the application of the same level of current. As can be seen in this thesis, dendritic currents were significantly reduced due to an altered dendritic input, which could normalize the hyperexcitability in neurons. This compensatory effect could possibly be explained by the presence of a homeostatic process. Indeed, homeostatic mechanisms that rectify a chronic change in neural firing are well-known (180; 181).

An unexpected finding of this thesis was that CA1 pyramidal neurons of control and mutant mice showed similar phase locking both during theta and ripple oscillations. Reduced oscillatory strength might suggest that, on the level of individual neurons, the signal- (synchronous input) to-noise (desynchronized/asynchronous input) ratio is decreased. As such, at least a tendency toward less clear phase locking to both theta and ripple oscillations is expected. However, if the asynchronous input decreases as well, the signal-to-noise ratio remains the same and phase locking remains unaltered. Therefore, future studies might dissect the total CA1 input into a synchronous and asynchronous input to verify whether the asynchronous input has decreased as well; however, it is currently unclear how this might be achieved.

5.6 Electrophysiology and behavior

It is difficult to correlate a lack of changes in unit spiking to apparent behavioral deficiencies, as seen in the Y-Maze (Chapter 3.4) and in the Morris Water Maze tasks (133). However, unit analysis was only analyzed from baseline sleep recordings and from the activity of each individual neuron. Of course, individual neurons must coordinate their activity with each other for proper cerebral function. This coordination was not investigated in this study since the recording configuration did not allow the required number of individual units to be recorded during behavioral tasks. It

is therefore possible that these interactions were altered, but not recorded. The amount of unit activity recorded during behavior was very limited due to the fact that these recordings were performed with linear silicon probes. Since all of the behavioral paradigms used in this thesis had a spatial component, future studies might perform recordings in animals during a spatial task with probes optimized for unit recordings. This would allow characterization of place cells and their properties, such as their place field size, the control of firing rates in their place field including phase precession, and their occurrence when an animal explores a novel environment.

The recorded parameters were only obtained from actively running mice. Hippocampal LFP activity during immobility and investigation of corners, either with or without females, was not analyzed. Of course, decision making itself is a complex interaction between several brain regions besides than the hippocampus (26; 91; 192), making the behavioral read-out more variable. Interestingly though, it seems that once the decision to navigate the STSM maze was made, the hippocampal oscillations generated during navigation are similar enough between mice of the same genotype for statistically significant differences to appear between groups.

The STSM paradigm does show a trend towards reduced performance of mutant mice and, in agreement with the Morris water maze results (133), suggests a general deficiency in long-term spatial memory. It is therefore expected that repetition of the STSM paradigm with a larger cohort of mice will make this cognitive deficit statistically significant. The additional reduced performance shown in the Y-maze working memory task (Figure 3.4) suggests that K_v7/M-channel deficient mice are cognitively impaired across several behavioral paradigms. It would be highly interesting to test these mice in other behavioral tests such as fear conditioning or conditional taste aversion to see whether implicit memories are similarly affected.

5.7 Homeostatic mechanisms

Three properties of a homeostatic mechanism might be involved in counteracting chronic hyperexcitability: attenuation of intrinsic excitability, changes in neurotransmitter receptor expression, and altering presynaptic neurotransmitter release probability (39). Attenuation of intrinsic excitability cannot completely explain the observed phenotype, since the *in-vitro* work on CA1 pyramidal cells from K_v7/M-current-deficient mice revealed that, despite chronic K_v7/M-current deficiency, neurons were still hyperexcitable and membrane resistances, resting membrane potentials, and a possible compensatory effect through theta-resonant HCN channels was unaffected (133). Furthermore, data from this thesis reveal normal unit spiking properties despite a decreased synaptic input, which indicates that a certain level of hyperexcitability persisted. These findings, therefore, suggest that a homeostatic mechanism is at least partially achieved at the synaptic level.

The hypothesis of increased ripple occurrence was not confirmed in this thesis. However, the recordings of unit activity were performed in CA1, and not in CA3 where ripple generation takes place. Still, if one extrapolates the CA1 unit spiking results to CA3 and assumes that CA3 neurons also fire at normal rates, the normal ripple occurrence could be explained. A normal ripple occurrence with a normal CA3 output would only be in line with smaller sharp waves in the presence of a reduced synaptic transfer, either by a reduced release of excitatory neurotransmitters at the presynapse or by a reduced surface expression of postsynaptic receptors (39). A reduction of all synaptic input would also ensure that the ratio between synchronous and asynchronous input is unchanged, which could also explain the similar unit phase locking.

An electrophysiological experiment to confirm or refute the hypothesis of a reduced synaptic

transfer in the mice in this thesis would be a standard *in-vitro* setup in which Schaffer collaterals would be stimulated and the resulting sink in CA1 str. Rad recorded. A consistently lower field EPSP (fEPSP) would then confirm this hypothesis. Further experiments would then include a histological or pharmacological analysis to see any changes in postsynaptic receptor density, such as AMPA or NMDA receptors.

Additionally, keeping mutant mice on doxycycline until adulthood and then record them before, during and after a doxycycline-free period would allow to follow the timeline of the effect of K_v7/M-current ablation on changes in electrophysiological parameters, which might happen sequentially: first an increase in neural firing rates, then a homeostatic mechanism which scales down synaptic transfer.

Mice that express the dominant-negative K_v7 transgene throughout their entire lifespans (133) may show an epileptic phenotype and abnormal cerebral morphology. Whether this is the direct consequence of hyperexcitable neurons or a secondary effect of a homeostatic mechanism that tries to compensate this hyperexcitability is unclear. Mutants show altered unit activity during this neonatal period (111). This suggests that homeostatic normalization of unit activity is incomplete, though it should be mentioned that the reported unit activity was altered in the occurence of spike doublets and triplets, an analysis not shown in this thesis. Reduction of excitability through manipulation of intracellular chloride levels with bumetanide normalized gross morphological and behavioral abnormalities, correlating with a normalization of neonatal unit activity (111). It would be interesting to see whether adult hippocampal network patterns in these bumetanide treated K_v7/M-current deficient mice mimics the results found here. If so, this would even more strongly suggest that prevention of neural hyperexcitability during this critical period by counteracting the induced hyperexcitability activity through chloride level manipulation is an effective therapeutic strategy. Such a study, comparing doxycycline with bumetanide application during the ciritical period in the mouse model used in this thesis, with WT mice and vehicle treatment as controls, might be more easily achieved in acute recordings under urethane anesthesia.

5.8 Conclusion

As hypothesized in Chapter 1.6.1 [1], typical hippocampal CA1 LFP activity patterns, such as theta/gamma oscillations and SW-R complexes, are present in K_v7/M-current deficient mice. [2] A reduction in theta and gamma power during theta-associated behaviors was identified as hypothesized, although this may be due to a secondary homeostatic mechanism rather than the direct involvement of K_v7/M-currents. [3] This thesis shows, for the first time, the effect of reduced K_v7/M-current on the SW-R complex (although this may again be due to a secondary homeostatic mechanism). [4] Sharp-wave/ripple properties were altered, but not as expected. Due to the role of K_v7/M-currents in spike frequency adaptation and the high firing rates during ripples, an increase in length and amplitude was expected, but not found.

Although the genetic model used does not precisely reflect a patient with a *KCNQ* mutation, it does contribute to the ability to distinguish developmentally related alterations of brain wiring from effects found in adults. This model also clearly puts forward the notion that evidence from transient pharmacological interventions, such as the application of XE991, either *in-vivo* or *in-vitro*, may not be directly transferred to long-term effects because compensatory mechanisms are likely to be upregulated to counteract chronic exposure. This may also be the reason why short-

term application of K_v7/M-current inhibitors can lead to cognitive improvement, whereas long-term K_v7/M-current suppression leads to cognitive deficits. The results in this thesis therefore substantially contribute to the understanding of the effect of chronic K_v7/M-current deficiency in the mammalian brain. Furthermore, since neural hyperexcitability is reported in pain (166) and after stroke (147), this mouse model may provide additional insight into homeostatic adaptation mechanisms upon induction of hyperexcitability beyond epilepsy related channelopathies.

Abbreviations

AAC	Axo-axonic cell
AIS	Axo-initial segment
AHP	Afterhyperpolarization
AKAP	A-kinase-anchoring protein
AMPA	α-amino-3-hydroxy-5-methyl-4- isoxazolepropionic acid
Ank-G	Ankyrin-G
ANOVA	Analysis of variance
AP	Action potential
BC	Basket cell
BFNC	Benign familiar neonatal convulsionsl
BS	Bistratisfied cell
CA	Cornu Ammonis
CaM	Calmodulin
cAMP	Cyclic adenosine monophosphate
ccc	Circular concentration coefficient
CNS	Central nervous system
CSD	Current source density
Cx	Cortex
DG	Dentate gyrus
EC	Entorhinal cortex
EEG	Electroencephalogram
EMF	Electromotive force
EMG	Electromyogram
EPSC	Excitatory postsynaptic current
EPSP	Excitatory postsynaptic potential
fEPSP	Field excitatory postsynaptic potential
GABA	γ-aminobutyric acid
LFP	Local field potential
LM	Lacunosum moleculare
LTP	Long term potentiation
IPSC	Inhibitory postsynaptic current
IPSP	Inhibitory postsynaptic potential
MI	Modulation index
NMDA	N-methyl-D-aspartic acid
Or	Oriens
PC	Pyramidal cell
PIP2	Phosphatidylinositol-4,5-bisphosphate
pK-C	Protein kinase C
PP	Perforant path
PSC	Postsynaptic current
PV	Parvalbumin

Pyr	Pyramidale
REM	Rapid eye movement
RMP	Resting membrane potential
SC	Schaffer collaterals
SD	Standard deviation
str.	Stratum
STSM	Single trial spatial memory
SW	Sharp wave
SW-R	Sharp wave - ripple
SWS	Slow wave sleep
TRE	Tetracycline-responsive element
tTA	Tetracycline-senstive transactivator

Bibliography

[1] Akam, T., and Kullmann, D. M. Oscillations and filtering networks support flexible routing of information. *Neuron 67*, 2 (2010), 308–20.

[2] Alexander, C., and Sadiku, M. *Fundamentals of Electric Circuits*, 3 ed. McGraw-Hill, New York, 2006.

[3] Andersen, P., Morris, R., Amaral, D., Bliss, T., and O'Keefe, J. *The Hippocampus Book*. Oxford University Press, Oxford, 2007.

[4] Barr, M. S., Radhu, N., Guglietti, C. L., Zomorrodi, R., Rajji, T. K., Ritvo, P., and Daskalakis, Z. J. Age-related differences in working memory evoked gamma oscillations. *Brain Research 1576* (2014), 43–51.

[5] Bauer, M., Oostenveld, R., Peeters, M., and Fries, P. Tactile spatial attention enhances gamma-band activity in somatosensory cortex and reduces low-frequency activity in parieto-occipital areas. *Journal of Neuroscience 26*, 2 (2006), 490–501.

[6] Bédard, C., Kröger, H., and Destexhe, A. Modeling extracellular field potentials and the frequency-filtering properties of extracellular space. *Biophysical journal 86*, 3 (2004), 1829–42.

[7] Behrens, C. J., van den Boom, L. P., de Hoz, L., Friedman, A., and Heinemann, U. Induction of sharp wave-ripple complexes in vitro and reorganization of hippocampal networks. *Nature neuroscience 8*, 11 (2005), 1560–7.

[8] Bichot, N. P., Rossi, A. F., and Desimone, R. Parallel and serial neural mechanisms for visual search in macaque area V4. *Science 308*, 5721 (2005), 529–34.

[9] Biervert, C., and Steinlein, O. K. Structural and mutational analysis of KCNQ2, the major gene locus for benign familial neonatal convulsions. *Human genetics 104*, 3 (1999), 234–40.

[10] Bliss, T. V. P., and Collingridge, G. L. Expression of NMDA receptor-dependent LTP in the hippocampus: bridging the divide. *Molecular brain 6* (2013), 5.

[11] Boehlen, A., Kunert, A., and Heinemann, U. Effects of XE991, retigabine, losigamone and ZD7288 on kainate-induced theta-like and gamma network oscillations in the rat hippocampus in vitro. *Brain research 1295* (2009), 44–58.

[12] Borgatti, R., Zucca, C., Cavallini, a., Ferrario, M., Panzeri, C., Castaldo, P., Soldovieri, M. V., Baschirotto, C., Bresolin, N., Bernardina, B. D., Taglialatela, M., and Bassi, M. T. A novel mutation in KCNQ2 associated with BFNC, drug resistant epilepsy, and mental retardation. *Neurology 63*, 1 (2004), 57–65.

[13] Boyce, R., Glasgow, S. D., Williams, S., and Adamantidis, A. Causal evidence for the role of REM sleep theta rhythm in contextual memory consolidation. *Science 352*, 6287 (2016), 812–816.

[14] Bragin, A., Hetke, J., Wilson, C. L., Anderson, D. J., Engel, J., and Buzsáki, G. Multiple site silicon-based probes for chronic recordings in freely moving rats: implantation, recording and histological verification. *Journal of Neuroscience Methods 98*, 1 (2000), 77–82.

[15] Bragin, A., Jandó, G., and Nádasdy, Z. Gamma (40-100 Hz) oscillation in the hippocampus of the behaving rat. *Journal of Neuroscience 15*, January (1995).

[16] Brandon, M. P., Bogaard, A. R., Andrews, C. M., and Hasselmo, M. E. Head direction cells in the postsubiculum do not show replay of prior waking sequences during sleep. *Hippocampus 22*, 3 (2012), 604–18.

[17] Brown, D., and Adams, P. Muscarinic suppression of a novel voltage-sensitive K+ current in a vertebrate neurone. *Nature 283* (1980), 673–676.

[18] Burgess, N. Spatial cognition and the brain. *Annals of the New York Academy of Sciences 1124* (2008), 77–97.

[19] Buzsáki, G. Theta oscillations in the hippocampus. *Neuron 33*, 3 (2002), 325–340.

[20] Buzsáki, G. Theta rhythm of navigation: link between path integration and landmark navigation, episodic and semantic memory. *Hippocampus 15*, 7 (2005), 827–40.

[21] Buzsáki, G., Anastassiou, C., and Koch, C. The origin of extracellular fields and currents–EEG, ECoG, LFP and spikes. *Nature reviews. Neuroscience 13*, 6 (2012), 407–20.

[22] Buzsáki, G., Buhl, D. L., Harris, K. D., Csicsvari, J., Czéh, B., and Morozov, A. Hippocampal network patterns of activity in the mouse. *Neuroscience 116*, 1 (2003), 201–211.

[23] Buzsáki, G., and Draguhn, A. Neuronal oscillations in cortical networks. *Science 304*, 5679 (2004), 1926–1929.

[24] Buzsáki, G., and Moser, E. I. Memory, navigation and theta rhythm in the hippocampal-entorhinal system. *Nature Neuroscience 16*, 2 (2013), 130–138.

[25] Catterall, W. A. Ion channel voltage sensors: structure, function, and pathophysiology. *Neuron 67*, 6 (2010), 915–28.

[26] Chen, J. L., Andermann, M. L., Keck, T., Xu, N.-l., and Ziv, Y. Imaging Neuronal Populations in Behaving Rodents : Paradigms for Studying Neural Circuits Underlying Behavior in the Mammalian Cortex. *Journal of Neuroscience 33*, 45 (2013), 17631–17640.

[27] Cherny, V. V., Markin, V. S., and DeCoursey, T. E. The voltage-activated hydrogen ion conductance in rat alveolar epithelial cells is determined by the pH gradient. *The Journal of general physiology 105*, 6 (1995), 861–96.

[28] Chrobak, J., and Buzsáki, G. High-frequency oscillations in the output networks of the hippocampal–entorhinal axis of the freely behaving rat. *The Journal of Neuroscience 76*, 9 (1996), 3056–3066.

[29] Chung, H. J., Jan, Y. N., and Jan, L. Y. Polarized axonal surface expression of neuronal KCNQ channels is mediated by multiple signals in the KCNQ2 and KCNQ3 C-terminal domains. *Proceedings of the National Academy of Sciences of the United States of America 103*, 23 (2006), 8870–5.

[30] Colgin, L. L., Denninger, T., Fyhn, M., Hafting, T., Bonnevie, T., Jensen, O., Moser, M.-B., and Moser, E. I. Frequency of gamma oscillations routes flow of information in the hippocampus. *Nature 462*, 7271 (2009), 353–7.

[31] Colgin, L. L., and Moser, E. I. Gamma oscillations in the hippocampus. *Physiology (Bethesda, Md.) 25*, 5 (2010), 319–29.

[32] Conley, E. C., and Brammar, W. J. Voltage-gated channels. In *The Ion channel FactsBook*, vol. IV. Academic Press, San Diego, 1999.

[33] Cook, L., Steinfels, G., Rohrbach, K., and DeNoble, V. Cognition enhancement by the acetylcholine releaser dup 996. *Drug Development Research 19* (1990), 301–314.

[34] Cooper, E. C., Harrington, E., Jan, Y. N., and Jan, L. Y. M channel KCNQ2 subunits are localized to key sites for control of neuronal network oscillations and synchronization in mouse brain. *Journal of Neuroscience 21*, 24 (2001), 9529–40.

[35] Cooper, E. C., and Jan, L. Y. M-channels: neurological diseases, neuromodulation, and drug development. *Archives of neurology 60*, 4 (2003), 496–500.

[36] Csicsvari, J., Jamieson, B., Wise, K. D., and Buzsáki, G. Mechanisms of gamma oscillations in the hippocampus of the behaving rat. *Neuron 37*, 2 (2003), 311–22.

[37] Cutsuridis, V., and Taxidis, J. Deciphering the role of CA1 inhibitory circuits in sharp wave-ripple complexes. *Frontiers in systems neuroscience 7*, May (2013), 13.

[38] Dailey, J., Cheong, J., and Ko, K. Anticonvulsant properties of D-20443 in genetically epilepsy-prone rats: prediction of clinical response. *Neuroscience . . . 195* (1995), 77–80.

[39] Davis, G. W. Homeostatic Signaling and the Stabilization of Neural Function. *Neuron 80*, 3 (2013), 1–22.

[40] Devaux, J. J., Abidi, A., Roubertie, A., Molinari, F., Becq, H., Lacoste, C., Villard, L., Milh, M., and Anikstejn, L. BRIEF COMMUNICATION A Kv7 . 2 mutation associated with early onset epileptic encephalopathy with suppression-burst enhances Kv7 / M channel activity r o. *Epilepsia 57*, 5 (2016), 87–93.

[41] Devaux, J. J., Kleopa, K. A., Cooper, E. C., and Scherer, S. S. KCNQ2 is a nodal K+ channel. *Journal of Neuroscience 24*, 5 (2004), 1236–44.

[42] Diba, K., and Buzsáki, G. Forward and reverse hippocampal place-cell sequences during ripples. *Nature neuroscience 10*, 10 (2007), 1241–2.

[43] Dingledine, R., Borges, K., Bowie, D., and Traynelis, S. F. The glutamate receptor ion channels. *Pharmacological reviews 51*, 1 (1999), 7–61.

[44] Dragoi, G., Carpi, D., Recce, M., Csicsvari, J., and Buzsáki, G. Interactions between hippocampus and medial septum during sharp waves and theta oscillation in the behaving rat. *Journal of Neuroscience 19*, 14 (1999), 6191–9.

[45] Dragoi, G., and Tonegawa, S. Preplay of future place cell sequences by hippocampal cellular assemblies. *Nature 469*, 7330 (2011), 397–401.

[46] Dunwiddie, T., and Lynch, G. Long-term potentiation and depression of synaptic responses in the rat hippocampus: localization and frequency dependency. *The Journal of physiology* (1978), 353–367.

[47] Eggermont, J. J., Smith, G. M., and Smith, M. Synchrony between single-unit activity and local field potentials in relation to periodicity coding in primary auditory cortex. *Journal of Neurophysiology* (2013), 227–245.

[48] Ego-Stengel, V., and Wilson, M. A. Disruption of ripple-associated hippocampal activity during rest impairs spatial learning in the rat. *Neuroscience Research 20*, 1 (2011), 1–10.

[49] Elul, R. The genesis of the eeg. *Int. Rev. Neurobiology 15* (1972), 227–272.

[50] Feldman, D. E. The spike timing dependence of plasticity. *Neuron 75*, 4 (2013), 556–571.

[51] Fellini, L., and Morellini, F. Mice Create What-Where-When Hippocampus-Dependent Memories of Unique Experiences. *Journal of Neuroscience 33*, 3 (2013), 1038–1043.

[52] Fidzinski, P., Korotkova, T., Heidenreich, M., Maier, N., Schuetze, S., Kobler, O., Zuschratter, W., Schmitz, D., Ponomarenko, A., and Jentsch, T. J. KCNQ5 K+ channels control hippocampal synaptic inhibition and fast network oscillations. *Nature Communications 6* (2015), 1–13.

[53] Fisahn, a., Pike, F. G., Buhl, E. H., and Paulsen, O. Cholinergic induction of network oscillations at 40 Hz in the hippocampus in vitro. *Nature 394*, 6689 (1998), 186–9.

[54] Fischer, R. S., van Emde Boas, W., Blume, W., Elger, C., Genton, P., Lee, P., and Engel Jr, J. Epileptic seizures and epilepsy: definitions proposed by the International League Against Epilepsy (ILAE) and the International Bureau for Epilepsy (IBE). *Epilepsia 46*, 10 (2005), 1698–9; author reply 1701–2.

[55] Fishbein, W., and Gutwein, B. M. Paradoxical sleep and memory storage processes. *Behavioral biology 19*, 4 (1977), 425–64.

[56] Fontán-Lozano, A., Suárez-Pereira, I., Delgado-García, J. M., and Carrión, A. M. The M-current inhibitor XE991 decreases the stimulation threshold for long-term synaptic plasticity in healthy mice and in models of cognitive disease. *Hippocampus 21*, 1 (2011), 22–32.

[57] Freeman, J., and Nicholson, C. Experimental optimization of current source-density technique for anuran cerebellum. *Journal of Neurophysiology* (1975).

[58] Fuchs, E. C., Zivkovic, A. R., Cunningham, M. O., Middleton, S. J., Lebeau, F. E. N., Bannerman, D. M., Rozov, A., Whittington, M. A., Traub, R. D., Rawlins, J. N. P., and Monyer, H. Recruitment of parvalbumin-positive interneurons determines hippocampal function and associated behavior. *Neuron 53*, 4 (2007), 591–604.

[59] Fuhrmann, F., Justus, D., Sosulina, L., Kaneko, H., Beutel, T., Friedrichs, D., Schoch, S., Schwarz, M., Fuhrmann, M., and Remy, S. Locomotion, Theta Oscillations, and the Speed-Correlated Firing of Hippocampal Neurons Are Controlled by a Medial Septal Glutamatergic Circuit. *Neuron 86*, 5 (2015), 1253–1264.

[60] Gadsby, D. C. Ion channels versus ion pumps: the principal difference, in principle. *Nature reviews. Molecular cell biology 10*, 5 (2009), 344–52.

[61] Gamper, N., and Shapiro, M. S. Calmodulin mediates ca^{2+}-dependent modulation of m-type k-channels. *Journal of General Physiology 122*, July (2003), 17–31.

[62] Gilman, a. G. G proteins: transducers of receptor-generated signals. *Annual review of biochemistry 56* (1987), 615–49.

[63] Girardeau, G., Benchenane, K., Wiener, S. I., Buzsáki, G., and Zugaro, M. B. Selective suppression of hippocampal ripples impairs spatial memory. *Nature neuroscience 12*, 10 (2009), 1222–3.

[64] Goldman, D. E. Potential, impedance and rectification in membranes. *Journal of General Physiology 27* (1943), 37–60.

[65] Gossen, M., and Bujard, H. Tight control of gene expression in mammalian cells by tetracycline-responsive promoters. *Proceedings of the National Academy of Sciences of the United States of America 89*, 12 (1992), 5547–51.

[66] Gray, C. M., Maldonado, P. E., Wilson, M., and McNaughton, B. Tetrodes markedly improve the reliability and yield of multiple single-unit isolation from multi-unit recordings in cat striate cortex. *Journal of Neuroscience methods 63*, 1-2 (1995), 43–54.

[67] Gregoriou, G. G., Gotts, S. J., Zhou, H., and Desimone, R. High-frequency, long-range coupling between prefrontal and visual cortex during attention. *Science 324*, 5931 (2009), 1207–10.

[68] Gu, N., Vervaeke, K., Hu, H., and Storm, J. F. Kv7/KCNQ/M and HCN/h, but not KCa2/SK channels, contribute to the somatic medium after-hyperpolarization and excitability control in CA1 hippocampal pyramidal cells. *The Journal of physiology 566*, Pt 3 (2005), 689–715.

[69] Hämäläinen, M., Hari, R., and Ilmoniemi, R. Magnetoencephalography—theory, instrumentation, and applications to noninvasive studies of the working human brain. *Reviews of modern physics* (1993).

[70] Harris, K. D., Henze, D. A., Csicsvari, J., Hirase, H., and Buzsáki, G. Accuracy of tetrode spike separation as determined by simultaneous intracellular and extracellular measurements. *Journal of neurophysiology 84*, 1 (2000), 401–14.

[71] Harris, K. D., Kadir, S., and Goodman, D. Klustakwik, 2000-2013.

[72] Hasselmo, M. Temporally structured replay of neural activity in a model of entorhinal cortex, hippocampus and postsubiculum. *European Journal of Neuroscience 28*, 7 (2008), 1301–1315.

[73] Hazan, L., Zugaro, M., and Buzsáki, G. Klusters, neuroscope, ndmanager: A free software suite for neurophysiological data processing and visualization. *Journal of Neuroscience Methods 155* (2006), 207–216.

[74] Hennevin, E., Hars, B., Maho, C., and Bloch, V. Processing of learned information in paradoxical sleep: relevance for memory. *Behavioural Brain Research 69*, 1-2 (1995), 125–135.

[75] Hernandez, C. C., Falkenburger, B., and Shapiro, M. S. Affinity for phosphatidylinositol 4,5-bisphosphate determines muscarinic agonist sensitivity of Kv7 K+ channels. *The Journal of general physiology 134*, 5 (2009), 437–48.

[76] Hille, B. *Ion channels of excitable membranes*, 3 ed. Sinauer Associates, Boston, 2001.

[77] Hodgkin, A. L., and Huxley, A. F. A quantitative description of membrane current and its application to conduction and excitation in nerve. *Bulletin of Mathematical Biology 52*, 1-2 (1990), 25–71.

[78] Hölscher, C., Schmid, S., Pilz, P. K. D., Sansig, G., van der Putten, H., and Plappert, C. F. Lack of the metabotropic glutamate receptor subtype 7 selectively modulates Theta rhythm and working memory. *Learning & memory 12* (2005), 450–455.

[79] Holsheimer, J. Electrical conductivity of the hippocampal CA1 layers and application to current-source-density analysis. *Experimental Brain Research 67* (1987), 402–410.

[80] Hu, H., Vervaeke, K., Graham, L. J., and Storm, J. F. Complementary theta resonance filtering by two spatially segregated mechanisms in CA1 hippocampal pyramidal neurons. *Journal of Neuroscience 29*, 46 (2009), 14472–83.

[81] Hu, H., Vervaeke, K., and Storm, J. F. Two forms of electrical resonance at theta frequencies, generated by M-current, h-current and persistent Na+ current in rat hippocampal pyramidal cells. *The Journal of Physiology 545*, 3 (2002), 783–805.

[82] Hutcheon, B., and Yarom, Y. Resonance, oscillation and the intrinsic frequency preferences of neurons. *Trends in Neurosciences 23*, 5 (2000), 216–222.

[83] Jefferys, J. G. Nonsynaptic modulation of neuronal activity in the brain: electric currents and extracellular ions. *Physiological reviews 75*, 4 (1995), 689–723.

[84] Jeneson, A., and Squire, L. R. Working memory, long-term memory, and medial temporal lobe function. *Learning & memory 19*, 1 (2012), 15–25.

[85] Jentsch, T. J. Neuronal KCNQ potassium channels: physiology and role in disease. *Nature reviews. Neuroscience 1*, 1 (2000), 21–30.

[86] Jespersen, T., Grunnet, M., and Olesen, S. r.-P. The KCNQ1 potassium channel: from gene to physiological function. *Physiology (Bethesda, Md.) 20*, 63 (2005), 408–16.

[87] Johnston, D., and Wu, S. *Foundations of Cellular Neurophysiology*. The MIT Press, Cambridge, 1997.

[88] Kajikawa, Y., and Schroeder, C. E. How local is the local field potential? *Neuron 72*, 5 (2011), 847–58.

[89] Kamondi, A., Acsády, L., Wang, X., and Buzsáki, G. Theta oscillations in somata and dendrites of hippocampal pyramidal cells in vivo: Activity dependent phase precession of action potentials. *Hippocampus 261*, March (1998), 244–261.

[90] Kaneko, S., Iwasa, H., and Okada, M. Genetic identifiers of epilepsy. *Epilepsia 43 Suppl 9*, 8 (2002), 16–20.

[91] Kennedy, A., Asahina, K., Hoopfer, E., Inagaki, H., Jung, Y., Lee, H., Remedios, R., and Anderson, D. J. Internal States and Behavioral Decision-Making : Toward an Integration of Emotion and Cognition. *Cold Spring Harbor Symposia on Quantitative Biology LXXIX* (2014), 199–210.

[92] Klausberger, T., and Somogyi, P. Neuronal diversity and temporal dynamics: the unity of hippocampal circuit operations. *Science 321*, 5885 (2008), 53–7.

[93] Klee, M., and Rall, W. Computed potentials of cortically arranged populations of neurons. *Journal of neurophysiology 40*, 3 (1977), 647–66.

[94] Kocsis, B., Bragin, a., and Buzsáki, G. Interdependence of multiple theta generators in the hippocampus: a partial coherence analysis. *Journal of Neuroscience 19*, 14 (1999), 6200–12.

[95] Kohler, H., Haider, C., and Woelki, S. Selectivity and dynamic behavior of glass electrodes. *Advances in Colloid and Interface Science 114 115* (2005), 281–290.

[96] Kopell, N., Ermentrout, G. B., Whittington, M. a., and Traub, R. D. Gamma rhythms and beta rhythms have different synchronization properties. *Proceedings of the National Academy of Sciences of the United States of America 97*, 4 (2000), 1867–72.

[97] Korotkova, T., Fuchs, E. C., Ponomarenko, A., von Engelhardt, J., and Monyer, H. NMDA receptor ablation on parvalbumin-positive interneurons impairs hippocampal synchrony, spatial representations, and working memory. *Neuron 68*, 3 (2010), 557–69.

[98] Krnjević, K., and Schwartz, S. The action of gamma-aminobutyric acid on cortical neurones. *Experimental brain research. Experimentelle Hirnforschung. Expérimentation cérébrale 3*, 4 (1967), 320–36.

[99] Kudrimoti, H. S., Barnes, C. a., and McNaughton, B. L. Reactivation of hippocampal cell assemblies: effects of behavioral state, experience, and EEG dynamics. *Journal of Neuroscience 19*, 10 (1999), 4090–101.

[100] Lerche, C., Scherer, C. R., Seebohm, G., Derst, C., Wei, a. D., Busch, a. E., and Steinmeyer, K. Molecular cloning and functional expression of KCNQ5, a potassium channel subunit that may contribute to neuronal M-current diversity. *The Journal of biological chemistry 275*, 29 (2000), 22395–400.

[101] Leung, L. S. Fast (beta) rhythms in the hippocampus: a review. *Hippocampus 2*, 2 (1992), 93–8.

[102] Leung, L. W., Lopes da Silva, F. H., and Wadman, W. J. Spectral characteristics of the hippocampal EEG in the freely moving rat. *Electroencephalography and clinical neurophysiology 54*, 2 (1982), 203–19.

[103] Li, Y., Gamper, N., Hilgemann, D. W., and Shapiro, M. S. Regulation of Kv7 (KCNQ) K+ channel open probability by phosphatidylinositol 4,5-bisphosphate. *Journal of Neuroscience 25*, 43 (2005), 9825–35.

[104] Li, Y., Gamper, N., and Shapiro, M. S. Single-channel analysis of KCNQ K+ channels reveals the mechanism of augmentation by a cysteine-modifying reagent. *Journal of Neuroscience 24*, 22 (2004), 5079–90.

[105] Lindén, H., Pettersen, K. H., and Einevoll, G. T. Intrinsic dendritic filtering gives low-pass power spectra of local field potentials. *Journal of computational neuroscience 29*, 3 (2010), 423–44.

[106] Lisman, J. E., and Jensen, O. The θ-γ neural code. *Neuron 77*, 6 (2013), 1002–16.

[107] Louie, K., and Wilson, M. a. Temporally structured replay of awake hippocampal ensemble activity during rapid eye movement sleep. *Neuron 29*, 1 (2001), 145–56.

[108] Madison, B. Y. D. V., and Nicoll, R. A. Physiol. (1984), 354,. *The Journal of Physiology* (1984), 319–331.

[109] Malenka, R. C., and Bear, M. F. LTP and LTD: an embarrassment of riches. *Neuron 44*, 1 (2004), 5–21.

[110] Mann, E. O., Radcliffe, C. a., and Paulsen, O. Hippocampal gamma-frequency oscillations: from interneurones to pyramidal cells, and back. *The Journal of physiology 562* (2005), 55–63.

[111] Marguet, S. L., Le-schulte, V. T. Q., Merseburg, A., Neu, A., Eichler, R., Jakovcevski, I., Ivanov, A., Hanganu-opatz, I. L., Bernard, C., Morellini, F., and Isbrandt, D. Articles Treatment during a vulnerable developmental period rescues a genetic epilepsy. *Nature Medicine 21*, 12 (2015), 1436–1444.

[112] Maviel, T., Durkin, T. P., Menzaghi, F., and Bontempi, B. Sites of neocortical reorganization critical for remote spatial memory. *Science 305*, 5680 (2004), 96–9.

[113] Mayer, M. L. Glutamate receptor ion channels. *Current opinion in neurobiology 15*, 3 (2005), 282–8.

[114] McNaughton, B. L., O'Keefe, J., and Barnes, C. A. The stereotrode: a new technique for simultaneous isolation of several single units in the central nervous system from multiple unit records. *The Journal of Neuroscience Methods*, 8 (1983), 391–7.

[115] McQuiston, a. R. Acetylcholine release and inhibitory interneuron activity in hippocampal CA1. *Frontiers in Synaptic Neuroscience 6*, September (2014), 1–7.

[116] Miceli, F., Soldovieri, M. V., Martire, M., and Taglialatela, M. Molecular pharmacology and therapeutic potential of neuronal Kv7-modulating drugs. *Current opinion in pharmacology 8*, 1 (2008), 65–74.

[117] Milkereit, D. *Charakterisierung und pharmakologische Behandlung der M-Strom-defizienten Maus (Mus musculus, Linnaeus 1758) KCNQ2^{Nmf134} als Modell neonataler Epilepsien*. PhD thesis, Universität Hamburg, 2013.

[118] Montgomery, S. M., and Buzsáki, G. Gamma oscillations dynamically couple hippocampal CA3 and CA1 regions during memory task performance. *Proceedings of the National Academy of Sciences of the United States of America 104*, 36 (2007), 14495–500.

[119] Morris, R., Garrud, P., Rawlins, J., and O'Keefe, J. Place navigation impaired in rats with hippocampal lesions. *Nature* (1982).

[120] Myers, K. M., and Davis, M. Behavioral and neural analysis of extinction. *Neuron 36* (2002), 567–584.

[121] Nagle, J. F., and Tristram-Nagle, S. Lipid bilayer structure. *Current Opinion in Structural Biology 10*, 4 (2000), 474–480.

[122] Nigro, M. J., Mateos-aparicio, P., and Storm, J. F. Expression and Functional Roles of Kv7 / KCNQ / M-Channels in Rat Medial Entorhinal Cortex Layer II Stellate Cells. *Journal of Neuroscience 34*, 20 (2014), 6807–6812.

[123] Nokia, M. S., Anderson, M. L., and Shors, T. J. Chemotherapy disrupts learning, neurogenesis and theta activity in the adult brain. *Eur J Neurosci 29*, 11 (2012), 997–1003.

[124] O'Keefe, J. Place units in the hippocampus of the freely moving rat. *Experimental neurology 109*, 1 (1976), 78–109.

[125] O'Keefe, J., and Dostrovsky, J. The hippocampus as a spatial map. Preliminary evidence from unit activity in the freely-moving rat. *Brain research 34* (1971), 171–175.

[126] O'Keefe, J., and Recce, M. L. Phase relationship between hippocampal place units and the EEG theta rhythm. *Hippocampus 3*, 3 (1993), 317–30.

[127] Oliva, A., Fernández-Ruiz, A., Buzsáki, G., and Berényi, A. Role of Hippocampal CA2 Region in Triggering Article Role of Hippocampal CA2 Region in Triggering Sharp-Wave Ripples. *Neuron 91*, 6 (2016), 1342–1355.

[128] Orhan, G., Bock, M., Schepers, D., Ilina, E. I., Reichel, S. N., L??ffler, H., Jezutkovic, N., Weckhuysen, S., Mandelstam, S., Suls, A., Danker, T., Guenther, E., Scheffer, I. E., De Jonghe, P., Lerche, H., and Maljevic, S. Dominant-negative effects of KCNQ2 mutations are associated with epileptic encephalopathy. *Annals of Neurology 75*, 3 (2014), 382–394.

[129] Pan, Z., Kao, T., Horvath, Z., Lemos, J., Sul, J.-y., Cranstoun, S. D., Bennett, V., Scherer, S. S., and Cooper, E. C. A Common Ankyrin-G-Based Mechanism Retains KCNQ and Na V Channels at Electrically Active Domains of the Axon. *Journal of Neuroscience 26*, 10 (2006), 2599–2613.

[130] Paoletti, P., and Neyton, J. NMDA receptor subunits: function and pharmacology. *Current opinion in pharmacology 7*, 1 (2007), 39–47.

[131] Pastalkova, E., Itskov, V., Amarasingham, A., and Buzsaki, G. Internally Generated Cell Assembly Sequences in the Rat Hippocampus. *Science 321*, 5894 (2008), 1322–1327.

[132] Pavlides, C., and Winson, J. Influences of hippocampal place cell firing in the awake state on the activity of these cells during subsequent sleep episodes. *Journal of Neuroscience 9*, 8 (1989), 2907–18.

[133] Peters, H. C., Hu, H., Pongs, O., Storm, J. F., and Isbrandt, D. Conditional transgenic suppression of M channels in mouse brain reveals functions in neuronal excitability, resonance and behavior. *Nature Neuroscience 8*, 1 (2005), 51–60.

[134] Petrantonakis, P. C., and Poirazi, P. A compressed sensing perspective of hippocampal function. *Frontiers in Systems Neuroscience 8*, August (2014), 1–13.

[135] Petroff, O. A. C. Book Review: GABA and Glutamate in the Human Brain. *The Neuroscientist 8*, 6 (2002), 562–573.

[136] Petsche, H., Stumpf, C., and Gogolak, G. The significance of the rabbit's septum as a relay station between the midbrain and the hippocampus I. The control of hippocampus arousal activity by the septum cells. *Electroencephalography and clinical Neurophysiology* (1962), 202–211.

[137] Pettersen, K. H., Devor, A., Ulbert, I., Dale, A. M., and Einevoll, G. T. Current-source density estimation based on inversion of electrostatic forward solution: effects of finite extent of neuronal activity and conductivity discontinuities. *Journal of Neuroscience methods 154*, 1-2 (2006), 116–33.

[138] Pfeiffer, B. E., and Foster, D. J. Hippocampal place-cell sequences depict future paths to remembered goals. *Nature 497*, 7447 (2013), 74–9.

[139] Piccinin, S., Randall, A. D., and Brown, J. T. KCNQ/Kv7 channel regulation of hippocampal gamma-frequency firing in the absence of synaptic transmission. *Journal of neurophysiology* (2006), 3105–3112.

[140] Poe, G. R., Nitz, D. a., McNaughton, B. L., and Barnes, C. a. Experience-dependent phase-reversal of hippocampal neuron firing during REM sleep. *Brain research 855*, 1 (2000), 176–80.

[141] Poe, G. R., Walsh, C. M., and Bjorness, T. E. *Cognitive neuroscience of sleep.*, vol. 185. Elsevier B.V., 2010.

[142] Prox, J., Bernreuther, C., Altmeppen, H., Grendel, J., Glatzel, M., D'Hooge, R., Stroobants, S., Ahmed, T., Balschun, D., Willem, M., Lammich, S., Isbrandt, D., Schweizer, M., Horré, K., De Strooper, B., and Saftig, P. Postnatal disruption of the disintegrin/metalloproteinase ADAM10 in brain causes epileptic seizures, learning deficits, altered spine morphology, and defective synaptic functions. *Journal of Neuroscience 33*, 32 (2013), 12915–28, 12928a.

[143] Reimann, M., Anastassiou, C., Perin, R., Hill, S. L., Markram, H., and Koch, C. A biophysically detailed model of neocortical local field potentials predicts the critical role of active membrane currents. *Neuron 79*, 2 (2013), 375–390.

[144] Ronen, G., Rosales, T., Connolly, M., Anderson, V., and Leppert, M. Seizure characteristics in chromosome 20 benign familial neonatal convulsions. *Neurology 43*, 7 (1993), 1355.

[145] Royer, S., Zemelman, B. V., Losonczy, A., Kim, J., Chance, F., Magee, J. C., and Buzsáki, G. Control of timing, rate and bursts of hippocampal place cells by dendritic and somatic inhibition. *Nature neuroscience 15*, 5 (2012), 769–75.

[146] Rudyl, B., and Seeburg, P. Molecular and functional diversity of ion channels and receptors. In *Annals of the New York Academy of Sciences*, vol. 868. New York Academy of Sciences, New York, 1999.

[147] Salar, S., Lapilover, E., Müller, J., Hollnagel, J.-o., Lippmann, K., Friedman, A., and Heinemann, U. Neurobiology of Disease Synaptic plasticity in area CA1 of rat hippocampal slices following intraventricular application of albumin. *Neurobiology of Disease 91* (2016), 155–165.

[148] Schlingloff, D., Káli, S., Freund, T. F., Hájos, N., and Gulyás, A. I. Mechanisms of sharp wave initiation and ripple generation. *Journal of Neuroscience 34*, 34 (2014), 11385–98.

[149] Schoenfeld, T. J., Kloth, a. D., Hsueh, B., Runkle, M. B., Kane, G. a., Wang, S. S.-H., and Gould, E. Gap Junctions in the Ventral Hippocampal-Medial Prefrontal Pathway Are Involved in Anxiety Regulation. *Journal of Neuroscience 34*, 47 (2014), 15679–15688.

[150] Schroeder, B. C., Hechenberger, M., Weinreich, F., Kubisch, C., and Jentsch, T. J. KCNQ5, a novel potassium channel broadly expressed in brain, mediates M-type currents. *The Journal of biological chemistry 275*, 31 (2000), 24089–95.

[151] Schroeder, B. C., Kubisch, C., Stein, V., and Jentsch, T. J. Moderate loss of function of cyclic-AMP-modulated KCNQ2/KCNQ3 K+ channels causes epilepsy. *Nature 396*, 6712 (1998), 687–90.

[152] Schwake, M. Surface Expression and Single Channel Properties of KCNQ2/KCNQ3, M-type K+ Channels Involved in Epilepsy. *Journal of Biological Chemistry 275*, 18 (2000), 13343–13348.

[153] Selyanko, a. a., Hadley, J. K., and Brown, D. a. Properties of single M-type KCNQ2/KCNQ3 potassium channels expressed in mammalian cells. *The Journal of physiology 534*, 1 (2001), 15–24.

[154] Senior, T. J., Huxter, J. R., Allen, K., O'Neill, J., and Csicsvari, J. Gamma oscillatory firing reveals distinct populations of pyramidal cells in the CA1 region of the hippocampus. *Journal of Neuroscience 28*, 9 (2008), 2274–86.

[155] Shah, M. M., Huang, Z., and Martinello, K. HCN and KV7 (M-) channels as targets for epilepsy treatment. *Neuropharmacology 69* (2013), 75–81.

[156] Shah, M. M., Migliore, M., Valencia, I., Cooper, E. C., and Brown, D. A. Functional significance of axonal Kv7 channels in hippocampal pyramidal neurons. *Proceedings of the National Academy of Sciences 105*, 22 (2008), 7869–7874.

[157] Shah, M. M., Mistry, M., Marsh, S. J., Brown, D. a., and Delmas, P. Molecular correlates of the M-current in cultured rat hippocampal neurons. *The Journal of Physiology 544*, 1 (2002), 29–37.

[158] Shapiro, M. S., Roche, J. P., Kaftan, E. J., Cruzblanca, H., Mackie, K., and Hille, B. Reconstitution of muscarinic modulation of the KCNQ2/KCNQ3 K(+) channels that underlie the neuronal M current. *Journal of Neuroscience 20*, 5 (2000), 1710–21.

[159] Sheremet, A., Burke, S. N., and Maurer, A. P. Movement Enhances the Nonlinearity of Hippocampal Theta. *Journal of Neuroscience 36*, 15 (2016), 4218–4230.

[160] Shigemoto, R., Kinoshita, a., Wada, E., Nomura, S., Ohishi, H., Takada, M., Flor, P. J., Neki, a., Abe, T., Nakanishi, S., and Mizuno, N. Differential presynaptic localization of metabotropic glutamate receptor subtypes in the rat hippocampus. *Journal of Neuroscience 17*, 19 (1997), 7503–22.

[161] Singh, N. A., Otto, J. F., Dahle, E. J., Pappas, C., Leslie, J. D., Vilaythong, A., Noebels, J. L., White, H. S., Wilcox, K. S., and Leppert, M. F. Mouse models of human KCNQ2 and KCNQ3 mutations for benign familial neonatal convulsions show seizures and neuronal plasticity without synaptic reorganization. *The Journal of physiology 586*, 14 (2008), 3405–23.

[162] Singh, R., Scheffer, I. E., Crossland, K., and Berkovic, S. F. Generalized epilepsy with febrile seizures plus: a common childhood-onset genetic epilepsy syndrome. *Annals of neurology 45*, 1 (1999), 75–81.

[163] Sivilotti, L., and Nistri, a. GABA receptor mechanisms in the central nervous system. *Progress in neurobiology 36*, 1 (1991), 35–92.

[164] Skaggs, W. E., McNaughton, B. L., Wilson, M. a., and Barnes, C. a. Theta phase precession in hippocampal neuronal populations and the compression of temporal sequences. *Hippocampus 6*, 2 (1996), 149–72.

[165] Smythe, J. W., Colom, L. V., and Bland, B. H. The extrinsic modulation of hippocampal theta depends on the coactivation of cholinergic and GABA-ergic medial septal inputs. *Neuroscience and biobehavioral reviews 16* (1992), 289–308.

[166] Snowball, A., and Schorge, S. Changing channels in pain and epilepsy : Exploiting ion channel gene therapy for disorders of neuronal hyperexcitability. *FEBS Letters 589*, 14 (2015), 1620–1634.

[167] Sohal, V. S., Zhang, F., Yizhar, O., and Deisseroth, K. Parvalbumin neurons and gamma rhythms enhance cortical circuit performance. *Nature 459*, 7247 (2009), 698–702.

[168] Soltesz, I., and Deschênes, M. Low- and high-frequency membrane potential oscillations during theta activity in CA1 and CA3 pyramidal neurons of the rat hippocampus under ketamine-xylazine anesthesia. *Journal of neurophysiology 70*, 1 (1993), 97–116.

[169] Song, M. K., Cui, Y. Y., Zhang, W. W., Zhu, L., Lu, Y., and Chen, H. Z. The facilitating effect of systemic administration of Kv7/M channel blocker XE991 on LTP induction in the hippocampal CA1 area independent of muscarinic activation. *Neuroscience Letters 461*, 1 (2009), 25–29.

[170] Squire, L. R., and Bayley, P. J. The neuroscience of remote memory. *Current opinion in neurobiology 17*, 2 (2007), 185–96.

[171] Storm, J. An after-hyperpolarization of medium duration in rat hippocampal pyramidal cells. *The Journal of physiology*, 1989 (1989), 171–190.

[172] Storm, J. F. Potassium currents in hippocampal pyramidal cells. In *Progress in Brain Research*, J. Storm-Mathisen, I. Zimmer, and O. Ottersen, Eds., vol. 83. Elsevier Science Publishers B.V. (Biomedical Division), 1990, pp. 161–187.

[173] Strogatz, S. H. *Nonlinear Dynamics and Chaos*. Westview Press, Cambridge, 1994.

[174] Stumpf, C. The fast component in the electrical activity of rabbit's hippocampus. *Electroencephalography and clinical neurophysiology*, 18 (1965), 477–486.

[175] Tort, A. B. L., Komorowski, R. W., Manns, J. R., Kopell, N. J., and Eichenbaum, H. Theta-gamma coupling increases during the learning of item-context associations. *Proceedings of the National Academy of Sciences of the United States of America 106*, 49 (2009), 2–7.

[176] Tort, A. B. L., Scheffer-Teixeira, R., Souza, B. C., Draguhn, A., and Brankačk, J. Theta-associated high-frequency oscillations (110-160Hz) in the hippocampus and neocortex. *Progress in neurobiology 100* (2013), 1–14.

[177] Traub, R. D., Bibbig, A., LeBeau, F. E. N., Buhl, E. H., and Whittington, M. a. Cellular mechanisms of neuronal population oscillations in the hippocampus in vitro. *Annual review of neuroscience 27* (2004), 247–78.

[178] Traub, R. D., and Miles, R. *Neuronal Networks of the Hippocampus*. Cambridge University Press, Cambridge, 1991.

[179] Tremblay, P., Meiner, Z., Galou, M., and Heinrich, C. Doxycycline control of prion protein transgene expression modulates prion disease in mice. *Proc. Natl. Acad. Sci. U. S. A.* (1998).

[180] Turrigiano, G. Too many cooks? Intrinsic and synaptic homeostatic mechanisms in cortical circuit refinement. *Annual review of neuroscience 34* (2011), 89–103.

[181] Turrigiano, G. Homeostatic synaptic plasticity: Local and global mechanisms for stabilizing neuronal function. *Perspectives in Biology 4* (2012), 1–17.

[182] Tzingounis, A. V., and Nicoll, R. A. Contribution of KCNQ2 and KCNQ3 to the medium and slow afterhyperpolarization currents. *Proc. Natl. Acad. Sci. U. S. A. 105*, 50 (2008), 19974–19979.

[183] Vanderwolf, C. H., and Heron, W. Electroencephalographic Waves With Voluntary Movement. *Archives of neurology 11* (1964), 379–384.

[184] Wang, Y., Romani, S., Lustig, B., Leonardo, A., and Pastalkova, E. Theta sequences are essential for internally generated hippocampal firing fields. *Nature Neuroscience 18*, 2 (2014), 282–288.

[185] Watanabe, H., Nagata, E., Kosakai, a., Nakamura, M., Yokoyama, M., Tanaka, K., and Sasai, H. Disruption of the epilepsy KCNQ2 gene results in neural hyperexcitability. *Journal of neurochemistry 75*, 1 (2000), 28–33.

[186] Weckhuysen, S., Mandelstam, S., Suls, A., Audenaert, D., Deconinck, T., Claes, L. R. F., Deprez, L., Smets, K., Hristova, D., Yordanova, I., Jordanova, A., Ceulemans, B., Jansen, A., Hasaerts, D., Roelens, F., Lagae, L., Yendle, S., Stanley, T., Heron, S. E., Mulley, J. C., Berkovic, S. F., Scheffer, I. E., and De Jonghe, P. KCNQ2 encephalopathy: Emerging phenotype of a neonatal epileptic encephalopathy. *Annals of Neurology 71* (2012), 15–25.

[187] Whittington, M. a., Traub, R. D., Kopell, N., Ermentrout, B., and Buhl, E. H. Inhibition-based rhythms: Experimental and mathematical observations on network dynamics. *International Journal of Psychophysiology 38* (2000), 315–336.

[188] Wilson, D. A. *Learning to Smell: Olfactory Perception from Neurobiology to Behavior*. Johns Hopkins University Press, Baltimore, 2006.

[189] Witter, M. P. Intrinsic and extrinsic wiring of CA3: indications for connectional heterogeneity. *Learning & memory 14*, 11 (2007), 705–13.

[190] World Health Organization. *Epilepsy fact sheet*. http://www.who.int, 2012.

[191] Xiong, Q., Sun, H., Zhang, Y., Nan, F., and Li, M. Combinatorial augmentation of voltage-gated KCNQ potassium channels by chemical openers. *Proceedings of the National Academy of Sciences of the United States of America 105*, 8 (2008), 3128–33.

[192] Yapici, N., Zimmer, M., and Domingos, A. I. Cellular and molecular basis of decision-making. *EMBO reports 15*, 10 (2014), 1023–1035.

[193] Ylinen, a., Bragin, a., Nádasdy, Z., Jandó, G., Szabó, I., Sik, a., and Buzsáki, G. Sharp wave-associated high-frequency oscillation (200 Hz) in the intact hippocampus: network and intracellular mechanisms. *Journal of Neuroscience 15*, 1 (1995), 30–46.

[194] Zhang, J., and Shapiro, M. S. Activity-dependent Transcriptional Regulation of M-type (Kv7) K+ Channels by AKAP79/150-mediated NFAT Actions. *Neuron 76*, 6 (2012), 1133–1146.